LABEL-FREE TRACKING OF PHOTOCATALYSIS ON A SINGLE NANOPARTICLE

BY

DINUMOL DEVASIA

DISSERTATION

Submitted in partial fulfillment of the requirements
for the degree of Doctor of Philosophy in Chemistry
in the Graduate College of the
University of Illinois Urbana-Champaign, 2021

Urbana, Illinois

Doctoral Committee:

Professor Prashant K. Jain, Chair
Associate Professor Joaquin Rodriguez-Lopez
Assistant Professor Lisa Olshansky
Assistant Professor Renske M. van der Veen

ABSTRACT

Nanocatalysis is a rapidly growing field where nanoparticles are exploited to catalyze industrially relevant chemical reactions. The successful design of these heterogeneous catalysts is hindered by our limited understanding of the chemical dynamics occurring in the working environment of a catalyst. An example is the limited mechanistic insights available on the photocatalytic reduction of CO_2 to hydrocarbons and other value-added chemicals. Monitoring catalysts in action—in situ investigation—can elucidate potential reaction intermediates and pathways, especially under the action of light. Additionally, by probing catalysis at the level of individual active nanoparticles one-at-a-time, interparticle heterogeneity in catalytic activity, information otherwise masked in ensemble measurements can be extracted and utilized for designing better catalysts.

To close the knowledge gap in CO_2 reduction (CO_2RR) studies, we have developed a sensitive and versatile in-situ surface enhanced Raman scattering (SERS)-based chemical imaging technique that has single-nanoparticle-level spatial resolution and a 100-ms time-resolution and can probe aqueous phase reactions. Using this technique, we studied plasmon-excitation assisted CO_2RR on individual Ag nanoparticle (NP) catalysts in CO_2-saturated water. This in-situ investigation of Ag NP catalysts at the single-nanoparticle level captured a rich array of C_1 and C_{2+} surface species formed in the CO_2RR. The catalog of species abundant with multi-carbon compounds, such as butanol, discovered in this study, hints the favorability of kinetically challenging C–C coupling on a plasmonically excited Ag surface.

Another advancement in this work was the use of isotope labeling in the single-molecule-level sensitive nanoscale probing of a NP surface. This, in turn allowed the confirmation that detected

surface species are the intermediates and products of the catalytic reaction—CO_2RR—rather than spurious contaminants.

Additionally, by cataloging the surface species profile on individual NPs of a population, we found that catalytic behavior fluctuates from NP to NP. Conventionally, the interparticle heterogeneity in catalytic activity is attributed to factors such as structural inhomogeneities or differences in the local environment. However, in our study, the fluctuations of the species were observed both across the population and in time. We infer that the fluctuations in large part represent noise resulting from the inherent stochasticity of chemical events probed on the level of individual NPs. Ultimately, this stochasticity is manifested as a NP-to-NP variation of the species profile. We were also able to exploit the NP-to-NP variation to determine pathways responsible for the formation of multicarbon species on the surface of Ag. This work exemplifies the power of nanoscale probing for revealing the otherwise hidden molecular-level behavior of a complex catalytic system. The surface chemical knowledge made accessible by our approach here will guide the future modeling and engineering of active and selective catalysts.

DEDICATION

To my beloved family.
Thank you for your endless love, sacrifices, prayers,
inspiration, and support.

ACKNOWLEDGEMENTS

First and foremost, I would like to thank the Almighty God who granted me this opportunity and helped me in the successful completion of this dissertation.

I would like to express the deepest appreciation to my advisor, Prof. Prashant K Jain, for the continuous support, patience, guidance, and motivation throughout my Ph. D. study and research. He guided me with his knowledge and feedback during the research and the writing of my dissertation.

I would like to thank my prelim and dissertation committee members Prof. Joaquin Rodriguez-Lopez, Prof. Renske M. van der Veen, Prof. Lisa Olshansky, and Prof. Gregory Girolami for all the support, helpful comments, and suggestions.

I would like to thank the sources that funded my research. This dissertation is based on work supported by the National Science Foundation under grant no. NSF CHE-1455011. Funding for part of the efforts was provided by the Energy & Biosciences Institute (EBI) through the EBI-Shell program. My early work performed with Gayatri Kumari was supported by an Arnold and Mabel Beckman Young Investigator Award made to Prof. Jain. I am also thankful for support from UIUC through the TechnipFMC Fellowship.

I express my sincere gratitude to Jain lab members. First, I would like to acknowledge Dr. Andrew J. Wilson for his mentorship, laser and microscope training, helpful suggestions, and constant support throughout my research. I would like to thank Dr. Gayatri Kumari who helped me to start my project. I thank Dr. Varun Mohan and Dr. Jaeyoung Heo for performing the electron microscopy characterization of the silver nanoparticles used in my experiments. The electron microscopy characterization was conducted at the Frederick Seitz Materials Research Laboratory at UIUC. I thank undergraduate researcher Maya Chattoraj who recently worked with me to carry forward the computation of Raman spectra of molecules using density functional theory. I thank Dr. Jianxiao Gong for being a good friend and mentor. I would like to thank all the other group members, especially Dr. Xueqiang Zhang, Dr. Kihyun Cho, and Dr. Daniel Dumett Torres for their help.

I would like to thank all my friends for all the fun, help, and constant support during my stay here.

And finally, many thanks to an understanding family who believed in me. I would like to acknowledge with gratitude, the love and support of my parents-Devasia and Shiney, my sister-Ditty and my brother-Diju. This dissertation would not have been possible without them.

TABLE OF CONTENTS

CHAPTER 1

IN SITU STUDIES OF CATALYSIS AT THE SINGLE-NANOPARTICLE AND SINGLE-MOLECULE LEVELS

1.1. THE NEED FOR THE STUDY OF CATALYSTS AND CATALYTIC PROCESSES

Catalysis is a core area of science that has a major impact in our daily lives because it lies at the heart of the chemical manufacturing sector. Catalysis is used at some stage in about 90% of chemical processes,[1–3] to enhance energy efficiency and/or to reduce energy usage. Hence catalysts are critically important, without which we would not have requisite access to energy, food, water, and medicines—the fundamental needs of society.

In the science world, a "catalyst" is a substance that initiates a reaction or alters its rate without undergoing a chemical or physical change by itself. The use of catalysts can save energy required for chemical processes and can provide us viable options for the use of renewable energy sources. Owing to their central importance, there is a great interest among researchers in understanding the structure and activity of catalysts. To improve existing catalysts and design new catalysts of high activity and selectivity, we need to understand how they operate. How does a catalyst drive chemical transformations of structurally diverse molecules maintaining its active/functional state? What dictates the activity of a catalyst? When does a catalyst become inactive? How to design a catalyst that can selectively activate an energetically less favored pathway? To answer these questions, and to design a champion catalyst that can thrive under the most demanding chemical reactions and maintain high activity and selectivity for a desired reaction, an understanding of this process at the molecular level is necessary. However, due to the inherent complexity, the study of catalysts presents a multitude of intellectual and technological challenges.

A heterogeneous catalyst—the one in a phase different from reactants and products—is often favored in industry due to the ease of separation and purification of products from unreacted reagents. A wide variety of petroleum products, fertilizers, pharmaceuticals, and precursors for polymers are manufactured using solid catalysts.[4–7] In industrially relevant heterogeneous catalytic reactions, reactive gases are passed over a metal or metal oxide surface. Synthesis of ammonia, sulfuric acid, and nitric acid and reforming of naphtha are some examples of industrial processes where the aforementioned strategy is used.[5,8]

A heterogeneous catalytic process involves a variety of complexities. First, solid catalysts are mostly used in the form of a fine powder (consisting of grains or pellets of size ranging from 10 μm to 10 mm) or as nanoparticles (NPs). Decades ago, it was established that the performance of these catalytic particulates is influenced significantly by their size, shape, and composition. Practically, a typical catalyst incorporates particles of varying dimensions, shapes, and compositions. As a result, there are considerable variations in activity and selectivity across the catalyst material. Often, particulate catalysts are supported on a high surface area material or porous support such as a metal oxide surface (Fig. 1.1).[9] Additionally, the electronic interaction with the support could influence the properties of the catalyst. If the support surface is non-uniform, the influence of the support would result in additional variations in the catalytic properties. Furthermore, support surfaces may not be inert and may themselves participate in the catalytic chemistry. Understanding these complexities and heterogeneities in catalytic behavior requires a high-spatial resolution study of the structure and functioning of heterogeneous catalysts.

Traditionally heterogeneous catalysts are studied by a range of techniques. The products and byproducts formed in the catalytic reaction are characterized using gas chromatography methods; the catalyst material is structurally characterized employing a range of techniques such as electron microscopy, X-ray fluorescence spectrometry, X-ray photoelectron spectroscopy, X-ray diffraction, Infrared/Raman spectroscopy. These measurements are sometimes performed pre-and post-reaction to account for any changes, such as oxidation, reduction, changes in surface oxidation state or morphology, induced by the reaction. In these conventional measurements, catalysts are characterized at an ensemble level: an average property of all the catalyst nanoparticles is measured. Using this approach, we lose important information about how individual catalyst NPs differ in their structural properties and consequently in their catalytic activity and product selectivity. To capture this information, which would greatly enhance structure–activity understanding of solid-state catalysis, individual NPs need to be characterized in terms of their catalytic properties. The ultimate aspiration is to study catalytic chemistry on individual NPs with single-molecule resolution in real time under operating conditions. Such measurements will enable atomic-level understanding of the structure, activity, and dynamics of the catalyst occurring under reaction conditions and revolutionize the future design of these complex materials.

1.2. TRACKING OF CATALYSIS AT THE SINGLE-MOLECULE-LEVEL

One of the most important form of industrial catalysts is NPs. Regardless of the impressive development achieved in synthesizing monodisperse homogeneous NPs, there is still significant structural heterogeneity in NP-based catalyst samples. Even otherwise, at the individual NP-level, there can be spatial variations and temporal changes in activity arising from the interaction of local sites with reactive species. To account for this intra-nanoparticle-level and dynamic heterogeneity, single-molecule-level tracking of individual NPs is necessary.

One of the most prominent methods that has emerged in the last decade for probing catalysis on single NPs is fluorescence microscopy.[10–14] This technique, based on the phenomenon of fluorescence emission of molecules, has single-molecule level sensitivity making it widely popular. Fluorescence is a process in which a molecule emits light after (typically within 10^{-8} s) it absorbs light and gets photoexcited. It involves a spin-allowed, singlet–singlet electronic transition and in most cases, the emitted radiation has a wavelength longer (and hence lower photon energy) than the absorbed radiation.

Single molecules were first observed optically at room temperature back in 1976.[15] Shera et. al reported for the first time the detection of fluorescent light from a single rhodamine-6G molecule.[16] Single fluorescent molecules were detected for the first time in solids at cryogenic temperatures[17,18] which later led to the development of Nobel-Prize-winning super-resolved fluorescence microscopy. Around the same time, room temperature imaging of single fluorophores was achieved with near-field scanning optical microscopy.[19] Following these advancements, researchers started widely using the fluorescence approach to study single-enzyme-molecule catalytic dynamics and kinetics.[20–24] Till date, single-molecule fluorescence microscopy remains the most popular method for probing biomolecular processes at the single-molecule level. Typically, biomacromolecules of interest are labeled with a fluorophore and then tracked with an optical microscope.

In recent years, several research groups adopted this strategy to study catalysis on individual NPs.[11,25] In a typical study, the NP catalyzes the conversion of a non-fluorescent reactant molecule to a strongly fluorescent product molecule on the surface of a NP. The light emitted from an individual fluorescent product molecule is then detected using a detector such as charge-coupled device (CCD) camera. Hofkens and coworkers first utilized the fluorescence approach to map the spatial distribution of catalytic activity on micron-sized layered double hydroxide crystals in solution.[26] Photocatalysis on TiO_2 surfaces,[27] catalysis on single Au NP,[25] and solid state reactions in nanocrystals[28,29] are other examples where fluorescence was used as the probe to track chemical transformations.

As shown in Fig. 1.2a, b, in a typical experiment setup, a fluorogenic reaction is catalyzed by the NP where the non-fluorescent reactant and fluorescent product are temporarily adsorbed to the NP surface. To suppress background fluorescence, a TIRF technique is generally used (Fig. 1.2a, b). A microfluidic reactor is prepared with a transparent support and cover glass. Here, an evanescent wave is used to selectively excite a thin 100-nm-scale layer of the sample close to the coverslip (where the catalytic NPs are deposited, and surface reactions take place) instead of non-selectively exciting the entirety of the reaction medium (Fig. 1.2a); this strategy suppresses background fluorescence that would otherwise arise from species in the bulk reaction medium. The fluorescent emission from an individual NP is collected. The time trajectory of the acquired emission (Fig. 1.2c) shows transitions between two states: a fluorescent (on) state, which represents a single product molecule adsorbed on the NP surface and a non-fluorescent (off) state, which represents the lack of any product molecules adsorbed onto the NP surface. Thus, the off → on transition represents the formation of a single product molecule, i.e., a single turnover event. The on → off transition represents the desorption of the product molecule. The time period between a product formation event and desorption of the product is the fluorescent time period (τ_{on}); the time period between a product desorption event and the next product formation event is the non-fluorescent time period (τ_{off}). By analyzing these two time-constants of molecular events and the heterogeneity they exhibit, Chen and co-workers obtained insights into the microscopic kinetics of catalytic reactions on the NPs and dynamic surface restructuring events.[25]

The possibility of studying catalytic reactions on a wide range of catalysts in real-time, with high-throughput and single-turnover resolution makes single-molecule fluorescence microscopy a powerful and versatile technique. The temporal resolution is in the millisecond range. However, the requirement of a fluorescent label limits the wide applicability of the technique: not all catalytic reactions involve fluorescent products and thus, the approach described applies to the study of fluorogenic reactions alone. To extend this approach to non-fluorogenic reactions, indirect detection/deduction or correlation methods need to be employed. Alternatively, a fluorogenic version of a reaction needs to be designed to enable the study of a reaction of our interest. That is why a fluorescent label-free technique is essential for the in-situ study of a wide range of catalytic processes at the single-molecule level.

1.3. LABEL-FREE PROBING OF CHEMISTRY ON THE NANOSCALE AND SINGLE-MOLECULE LEVELS

To realize label-free probing of chemical transformations, one can apply a universal molecular phenomenon as the chemical probe, e.g., vibrational signatures of reactants, intermediates, and products. To serve this purpose, Raman spectroscopy based on the inelastic scattering of light by molecular vibrations is a great choice of technique. It provides Raman spectra, which are vibrational fingerprints of molecules (and even molecular fragments). Although Raman scattering is a weak phenomenon, the Raman signals of molecules can be enhanced in the presence of a photoexcited nanostructured surface of Au, Ag, or Cu. This effect is called surface-enhanced Raman scattering (SERS).[30–32] Au, Ag, and Cu nanostructures exhibit plasmon resonances, i.e., collective resonant excitations of free electrons at visible frequencies. The excitation of these plasmon resonances by visible light results in an intense electric field felt on the surface of the nanostructure and a resulting electromagnetic enhancement of Raman scattering from molecules at or near the surface of the nanostructure.[33] In addition, adsorbed molecules also undergo chemical enhancement of their Raman scattering.[34–36] These underlying mechanisms render SERS high sensitivity and surface specificity. Consequently, SERS has the potential to probe with single-molecule resolution[37] chemical events (adsorption, molecular transformations, and charge transfer) occurring on a catalyst surface.[38–45]

In the literature, there are examples of single-molecule-level SERS detection.[37,46–48] These studies are often performed using model systems such as crystal violet[46,49] or R6G[47,50,51], which are dye molecules with high Raman cross-sections due to resonant enhancement in the visible region. SERS has also been used to monitor reactions such as the photoinduced conversion of p-nitrothiophenol (pNTP) to p, p'-dimercaptoazobenzene (DMAB).[44,52] Analogous to SERS, Raman signals can be enhanced by the electromagnetic fields supported by sharp metallic tips. This technique is called tip-enhanced Raman spectroscopy (TERS) that can have a spatial resolution (< 10 nm) superior to that of SERS when fine tips are used.[53] In a TERS setup (Fig. 1.3a), the Ag-coated atomic force microscopy (AFM) tip acts as the Raman scattering enhancer. On the other hand, in SERS (Fig. 1.3b), metallic NPs serve as the SERS substrate, in some cases, also as the catalyst studied. The amplified Raman scattering from all the reactants and products are collected by the microscope objective, which is then directed to a spectrometer–detector system. However, the technique can be applied to other surfaces as well; there have been demonstrations of SERS probing of nanometer-thin films overcoated on an underlying SERS substrate.[54–56]

While SERS has been demonstrated for the study of model reactions, e.g., pNTP conversion, it has the potential to be applied more generally to the study of important catalytic transformations, especially ones where the reaction events involved are not known a priori and do not involve resonant SERS probes. Aside from single-molecule-level probing, which can be mechanistically revealing; SERS can also be used to track the temporal profile of a reaction, e.g., formation of products and simultaneous depletion of reactants in real time on a single catalyst NP,[44] thus yielding single-NP-level kinetics. SERS also has the potential to provide us information about the surface chemistry of the catalyst itself because the surface presents its own vibrational signatures, which are sensitive to the chemical state such as oxidation or hydroxylation. The major limitation of the SERS is the requirement of a component that can produce the SERS effect: a plasmonic material or a tip. Interpretation of SERS spectra in complex environments and performing quantitative analysis are other major challenges in the use of SERS probing. With further studies and design of modified approaches, these limitations and challenges need to be overcome.

My dissertation work described in the proceeding chapters focused on establishing SERS as a powerful tool for molecular-level probing of important catalytic conversions where the mechanism and scheme of reaction events are not known beforehand. Carrying forward from a prior proof-of-concept study from the Jain lab,[45] my PhD work developed the use of single-NP SERS in liquid media, improved the reliability of spectroscopic analysis and interpretation, and applied the approach to visible-light mediated reduction of CO_2 on metal NPs in liquid water.

1.4. FIGURES

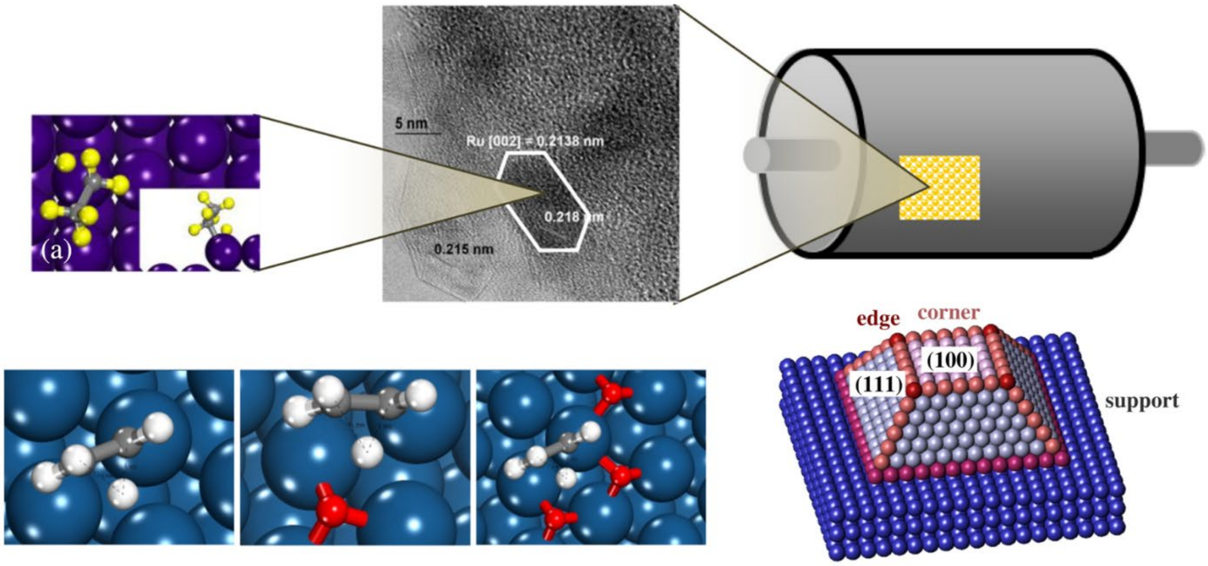

Figure 1.1. A heterogeneous catalytic system at various scales: industrial-scale catalytic bed (10 m scale), catalytically active NP (10 nm scale), and the molecular scale on which the catalytic reactions take place. Not all NPs in the catalytic bed are identical. In addition to their differences in terms of size, shape, and composition, the constitution of the surface facets and the fraction and spatial distribution of highly active edge and corner atoms could vary from one NP to another. These structural features are the key determinants of catalytic activity. Reprinted from ref. 9, Copyright (2011), with permission from Elsevier.

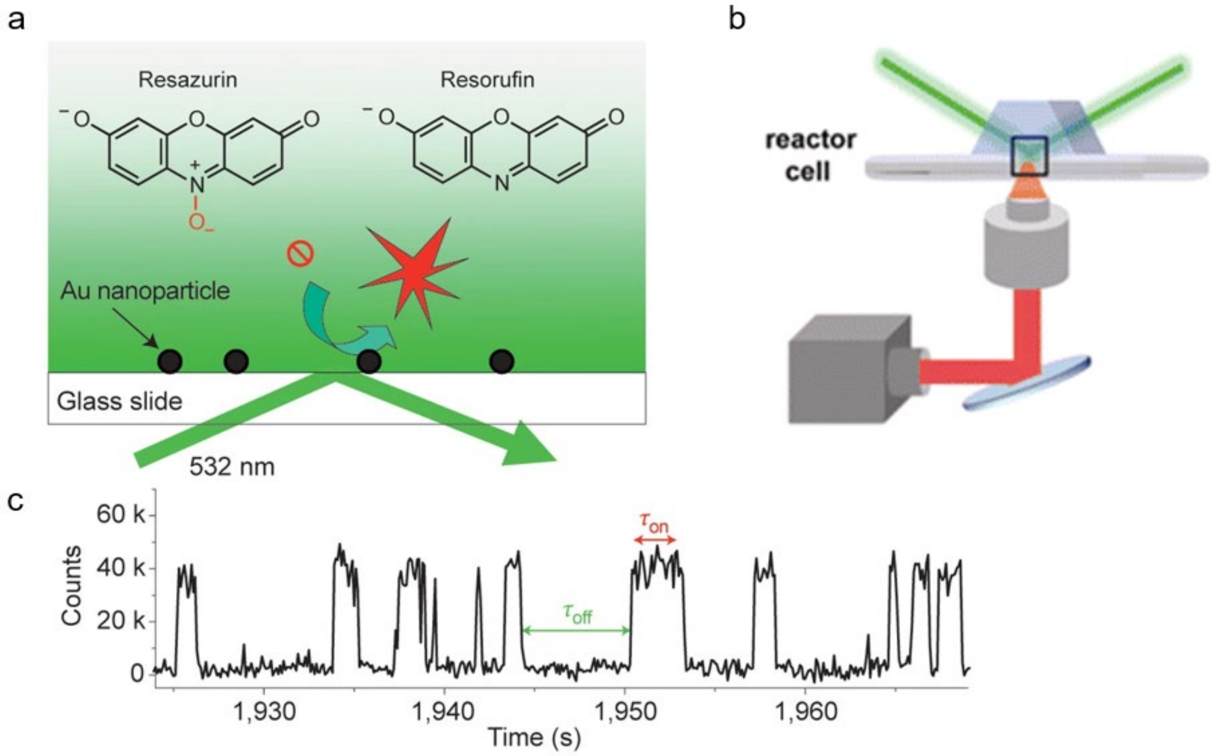

Figure 1.2. Single-molecule-level mapping of fluorogenic reactions on NP-based catalysts. a) A fluorogenic reaction where a non-fluorescent reactant molecule (resazurin) is converted to strongly fluorescent product (resorufin) molecule on the surface of a catalytic Au NP b) A total internal reflection fluorescence (TIRF) setup for single-molecule-resolution fluorescence microscopy. An evanescent wave is used for the selective excitation of a thin region close to the glass–reaction medium interface. The resulting fluorescent emission is then collected using an objective lens and detected with a charge-coupled device (CCD) camera. c) Example of a time-trajectory of the fluorescent emission acquired from a NP showing single-molecule events of formation of fluorescent P (off → on level) and disappearance (on → off level). Figs. a and c, reprinted by permission from Springer Nature: ref. 25, Copyright (2008). Fig. b, reprinted with permission from ref. 181. Copyright (2013) American Chemical Society.

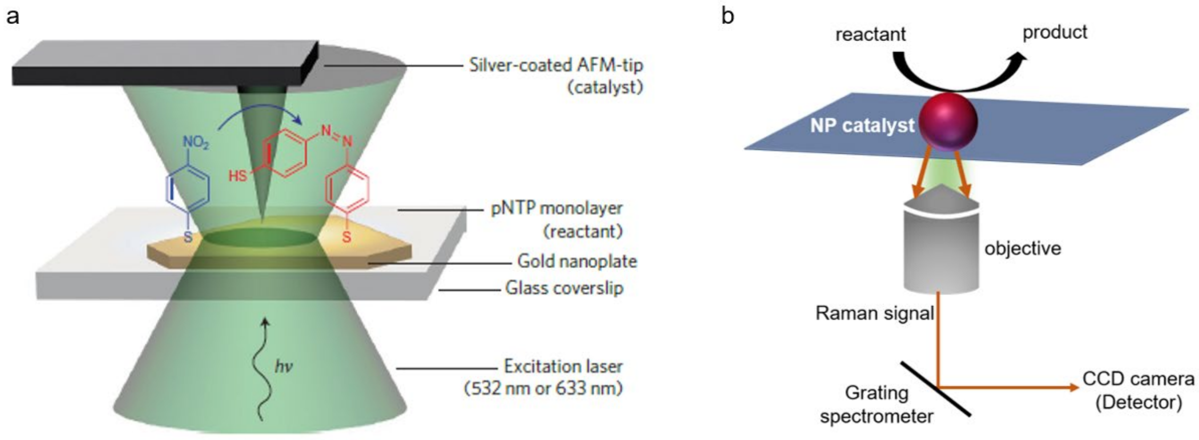

Figure 1.3. Experimental set-up for a) tip-enhanced Raman spectroscopy (TERS) and b) surface-enhanced Raman scattering (SERS). Fig. a, reprinted by permission from Springer Nature: ref. 54, Copyright (2012).

CHAPTER 2

A RICH CATALOG OF C–C BONDED SPECIES FORMED IN CO_2 REDUCTION ON A PLASMONIC PHOTOCATALYST

This chapter is reproduced, in full, with permission from a published article: *Devasia, D., Wilson, A. J., Heo, J., Mohan, V. & Jain, P. K. A rich catalog of C–C bonded species formed in* CO_2 *reduction on a plasmonic photocatalyst. Nat. Commun. 12, 2612 (2021*). I designed experiments, performed sample preparation, SERS experiments, DFT calculations, analysis, and co-wrote the manuscript. Dr. Andrew J. Wilson aided experimental design, developed data processing algorithm, and helped with analysis. Dr. Jaeyoung Heo performed TEM characterization and Dr. Varun Mohan performed SEM characterization. Prof. Prashant K. Jain conceived project, designed experiments, helped with analysis and interpretation, and co-wrote the manuscript.

2.1. INTRODUCTION

Traditionally, heterogeneous catalysts are tested, screened, and optimized on the basis of the products of the catalytic reaction that are formed in the bulk phase. Yet, it is the adsorbates, intermediates, and species formed on the surface of the catalyst that are the fundamental signifiers of how a catalyst functions. Quantum-chemical modeling of a catalyst relies on information of surface species, comprehensive knowledge of which under operando conditions is often poor. As a result, despite the success of empirical catalyst discovery, mechanistic understanding has remained limited. This is especially the case for catalytic chemistry such as the CO_2 reduction reaction (CO_2RR), where multiple steps and alternate pathways are involved. Chemical interrogation of the surface in-situ under catalytic turnover conditions is important for advancing molecular-level understanding and enabling knowledge-driven modeling of catalysts.[57]

Here, we characterize in comprehensive detail the surface species formed on a CO_2RR photocatalyst under operating conditions. In addition to the use of realistic aqueous conditions for this reaction, our methodology combines nanoscale spatial resolution[25,58–63] and sub-second temporal resolution, which allows us to capture ephemeral intermediates that are otherwise hidden in measurements averaged over larger ensembles.[28,29,64–68] The vast array of species captured in spectra is identified using an automated procedure that queries a database of carbonaceous compounds we developed for this study. A fuller picture of the chemical activity on the photocatalyst surface is thus obtained. Another important feature of our study is the development of isotopological validation of the nanoscale surface interrogation, which ensures that detected species are indeed the intermediates and products of the catalytic reaction rather than artefacts and contaminants that commonly plague surface interrogations in realistic reaction media.

We apply our approach to a plasmonic nanoparticle (NP)-based photocatalyst for the CO_2 reduction reaction (CO_2RR). The solar light driven-conversion of CO_2 and water into energy-dense, value-added multi-carbon molecules is of considerable interest as a technology for renewable energy generation and chemical manufacturing.[69] In particular, the fixation of CO_2 into liquid hydrocarbons and alcohols is desirable due to the high energy density and easy transportability of these products.[70,71] Consequently, there is an ongoing quest for a synthetic photocatalyst that facilitates the reduction of CO_2[72–74] and the coupling of the reduced intermediates into multi-carbon molecules.[75–77] Such C–C coupling, in particular, is kinetically unfavorable in most cases.

2.2. EXPERIMENTAL APPROACH

Plasmonic NPs of Au, Ag, and Cu have been found to photocatalyze CO_2RR due to the action of energetic electron–hole pairs formed by the decay of localized surface plasmon resonances (LSPRs)[78–82] excited in the NPs.[45,83–90] Further, Ag NPs serve as resonant optical antennas that concentrate electromagnetic fields at their surfaces[91] and lead to intense surface-enhanced Raman scattering (SERS) from molecules present at the surface of the NP.[92] SERS is a powerful tool for selectively probing the chemistry occurring at the surface of a plasmonic NP.[37,46,93–99] Previous work from our group and others has pushed the limits of SERS and used it for in-situ high-spatial resolution probing of chemical reactions without requiring the use of fluorogenic probes and reactions.[30,45,48,100–104] For the current study, we expanded single-NP-level SERS to a liquid water reaction medium and monitored plasmon-excitation-driven CO_2RR events on Ag NPs under these conditions. We found an unexpectedly wide range of C_1–C_4 species, including hydrocarbons, alcohols and oxygenates, to be formed on the NP surface under light excitation. The observed prevalence of C–C coupling on the Ag surface is striking and calls for further exploration and optimization of light-driven CO_2RR on Ag NPs. This work is also an experimental advance in chemical imaging in a label-free, high spatiotemporal resolution, and reliable manner. Our approach can be extended to the study of other light-driven reactions on surfaces in fluid media.

2.3. RESULTS

Single-NP-level SERS probing in an aqueous medium. The CO_2RR photocatalyst and SERS platform consisted of Ag NPs synthesized by the Lee–Meisel method.[105] The as-synthesized colloid contains NPs of a variety of sizes and shapes and surface-coated with citrate ligands (Figs. 2.5 and 2.6). The colloidal NPs were drop casted onto a clean coverslip (Fig. 2.7). We ensured that the area density was low enough for discrete scatterers to be spatially resolvable in diffraction-limited optical microscopy using a 60× objective (Figs. 2.1a, 2.8 and 2.9). The discrete scatterers are typically single Ag NPs, dimers, or trimers (Figs. 2.8–2.10) as determined by scanning electron microscopy (SEM) and transmission electron microscopy (TEM). The NP-coated substrate was then subjected to ultraviolet (UV) radiation to photo-oxidize and clean organic ligands and contaminants off the NP surface (Fig. 2.12a). This cleaning procedure ensures that SERS spectroscopy probes only CO_2 photoreduction activity and is not complicated by the photochemical reactions of citrate or other carbonaceous contaminants on the Ag NP surface.[102] UV light treatment has the potential to oxidize the Ag; extensive oxidation of the Ag NP preclude catalysis and SERS. Therefore, substrate-bound NPs subjected to photo-oxidative cleaning were examined by TEM, which shows that the NPs are comprised of metallic Ag and do not have a Ag oxide shell on the surface (Fig. 2.10). The morphology of the NPs does not appear to have been modified by UV light illumination. However, a Ag sub-oxide is indicated to be present by high-sensitivity surface characterization by SERS (Fig. 2.12b). Following photo-oxidative cleaning (Figs. 2.1b, 2.12 and 2.13), the NP-coated coverslip was integrated into a home-built microfluidic cell (Fig. 2.7). For SERS spectroscopy, the microfluidic cell was filled with deionized (DI) water saturated with CO_2 and mounted on an inverted microscope (Fig. 2.1a). Despite the presence of the liquid layer covering the Ag NPs, we were able to selectively probe chemical activity at the surface of the Ag NPs. The sharp decay of the electric field enhancement of Raman scattering over a distance on the order of 1–10 nm from the NP surface[106,107] ensures that the measured SERS signals emanate specifically from surface species; there is little to no contribution of SERS from the tens-of-μm-thick liquid layer.

Similar to our previous study,[45,103] we identified by dark-field scattering imaging individual diffraction-limited Ag NP scatterers that were spatially resolvable from other NP scatterers (Fig. 2.1). One such scatterer was then subjected to a beam of a continuous-wave 514.5 nm laser focused using a 60× objective. Note that a typical scatterer chosen for SERS may not be a single nanosphere; in fact, it is more likely an anisotropic NP, a NP dimer, or a NP trimer (Figs. 2.8–2.11). Such structures dominate dark-field scattering, display overlap of LSPR bands with the 514.5 nm laser excitation (Fig. 2.11),[45] and also exhibit large SERS signals due to the electric field hotspots supported at their inter-NP junctions[45,51] or sharp tips. Excitation of LSPRs by the 514.5 nm laser initiated photochemistry of CO_2 on the Ag NP surface. The 514.5 nm laser was also the Raman excitation source. SERS spectra arising from species formed on the Ag NP surface in the course of CO_2 photochemistry were acquired continuously under LSPR excitation with an acquisition time of 200 ms per frame. An interrogated scatterer does not migrate during the course of the acquisition, as we confirm at the end of each experiment. Using this method, 96 individual Ag NP scatterers were interrogated. More details can be found in the Methods section.

Spectral tracking of plasmon-excitation-driven CO_2RR events. The continuously acquired SERS spectra capture snapshots of discrete photochemical events occurring on the Ag NP surface under continuous LSPR excitation. This is best depicted by time-series of SERS spectra plotted as a spectrogram (Figs. 2.1c, 2.1d, 2.14a and 2.14b). SERS spectra acquired from individual plasmon-excited Ag NPs in CO_2-saturated water show dynamics in the fingerprint region, i.e., the 500–1800 cm^{-1} range where vibrational signatures of hydrocarbons, alcohols, acids, and esters are known to appear. In addition to fluctuations in the intensities of vibrational bands (Fig. 2.14c), specific vibrational modes appear and disappear signifying the formation of transient adsorbates and intermediates in photodriven CO_2RR at the NP surface. SERS spectra of individual plasmon-excited Ag NPs in water that is not intentionally saturated with CO_2 showed no vibrational bands in the fingerprint region (Figs. 2.1b, 2.1d, and 2.13). The result of this control experiment rules out the possibility of contaminants in water or adventitious adsorbates and ligands on the Ag NP surface causing the dynamic SERS activity observed in CO_2-saturated water.

Uncovering the array of surface species formed. From 96 individual Ag NP scatterers under photodriven CO_2RR conditions, we collected 98,000 SERS spectra, providing us with a comprehensive profile of the surface adsorbates and intermediates formed in the reaction. An examination of the spectra indicated that the range of species captured in the spectra is vast and includes many that are not known from bulk catalytic studies to be produced by Ag-catalyzed CO_2RR. To allow identification of these species without a priori bias, we used a database-query approach. From an extensive search of the CO_2RR literature,[108–121] we created a database (Table 2.1 and vibrational assignments in Tables 2.2–2.24) consisting of organic molecules that putatively can be generated by reactions starting from CO_2. The list includes both species formed by direct transformations of CO_2 and those formed indirectly by reactions between species formed directly from CO_2. This database can be further extended by us or others by inclusion of other probable products. Raman vibrational modes of all species in the database were calculated by density functional theory (DFT). An automated peak-matching algorithm was employed to assign each acquired spectrum to a species from this reference database (see Section 2.5.3). In a subset of cases, an acquired spectrum could not be assigned solely to one species; such a spectrum likely captured more than one species simultaneously present on the Ag surface during the 200 ms acquisition time.

It is known that electrochemical CO_2RR on Ag predominantly yields CO.[122–125] So, we scanned the large collection of spectra for the presence of CO, the stretching vibrational mode of which is expected to appear in the 1800–2200 cm^{-1} region, with the exact location dependent on its adsorption motif. But a small fraction of spectra (~0.1 %) obtained from the 96 individual NP scatterers corresponded to the detection of CO. Our analysis showed an abundance of other organic compounds, including multi-carbon ones. Thus, the surface species distribution uncovered here is richer than the typical bulk product distribution observed for electrochemical CO_2RR on Ag.[122–124] The detected species were grouped on the basis of the number of C atoms constituting them. The distribution was dominated by C_2–C_4 compounds, indicative of the prevalence of C–C coupling events on the NP surface under plasmon-excitation conditions. Representative examples of in-situ SERS spectra that captured various C_1–C_4 species are shown in Figs. 2.2 and 2.15–2.23.

The CO_2RR requires a counter oxidation reaction. Under the conditions of our in-situ SERS experiments, possible counter reactions are the oxidation of water to oxygen (O_2) or hydrogen peroxide (H_2O_2), Ag oxidation,[45] and Ag hydroxylation. We detected in SERS spectra instances of detection of O_2 (Fig. 2.23c) and H_2O_2 (Fig. 2.23b), which are indicative of water oxidation.

Isotopological validation of CO_2RR origin of surface species. Surfaces in realistic fluid media can often be contaminated with hydrocarbons and other organic compounds from the environment. Ligands leftover from NP synthesis can be another spurious source of species detected on the Ag NP surface. It was therefore important to ensure that the observed surface species were not artefactual and that the precursor of the detected species was indeed CO_2. We used isotope labeling[126,127] for this verification. We conducted SERS probing of plasmon-excitation-driven CO_2RR on individual Ag NP scatterers in an aqueous medium saturated with ^{13}C-labeled CO_2. Species generated from $^{13}CO_2$ are expected to have vibrational spectra with their mass-sensitive modes shifted in frequency with respect to the ^{12}C isotopologs. For each species, the expected isotopological frequency shift, $\nu(^{13}C) - \nu(^{12}C)$, was calculated by DFT for every vibrational mode in the Raman spectrum. We determined from experimental SERS spectra, isotopological shifts for all detected species (see Section 2.5.6) and compared them with the corresponding DFT-predicted values, as shown in Tables 2.25–2.45. For the surface species detected, the isotopological shifts observed in experiments have the same sign and magnitude, within one standard deviation (SD), as the corresponding DFT-predicted values for most of the vibrational peaks.

For clear visualization of the isotopological validation, measured SERS spectra of ^{12}C and ^{13}C isotopologs of each species are plotted in the form of spectral barcodes. An experimental barcode consists of vertical lines, which denote the averaged peak wavenumber for each SERS band in the spectrum. The method for barcode construction is detailed in Fig. 2.24. A reference barcode was also constructed from the DFT-computed Raman spectrum for each species. For all the major surface species (Figs. 2.3 and 2.25-2.29), the pattern of isotopological shifts is in close agreement between the experimental and reference (DFT-computed) barcodes. Thus, we validate our assignments of spectra to molecular species and also corroborate that CO_2 is the precursor of the detected surface species.

2.4. DISCUSSION

With the in-situ nanoscale SERS probing method fully validated, we discuss the major findings about chemical species formed in the plasmon-excitation-driven CO_2RR on Ag. Of the 42000 spectra collected from 40 individual Ag NP scatterers in $^{12}CO_2$-saturated water, 74 % of the spectra showed no SERS peaks (Figs. 2.4a, b). About 15 % of the spectra showed activity (Figs. 2.4a, b) and were assignable to a species in the reference database (Fig. 2.4d). The remaining 11% were non- assignable (Figs. 2.4a, b) as per our mode-match algorithm; it is possible that some of these spectra captured a species not present in the database or they captured species that have fewer than 3 modes in the fingerprint region.

A similar distribution was seen for the 56000 spectra acquired from 56 individual Ag NP scatterers in $^{13}CO_2$-saturated water (Fig. 2.30). The distribution of surface species by detection counts in the active, assigned spectra is shown in Fig. 2.4d. It must be noted that the relative counts of species are not a quantitative representation of their relative abundance because the likelihood of detection of a species is influenced by factors such as its Raman cross-section, chemical enhancement factor, orientation and location with respect to the electromagnetic field hotspot, and surface residence time. Furthermore, the identification of a species may be positively biased by the number of Raman vibrational modes in its SERS spectrum. Because of the conditions imposed by our algorithm, longer hydrocarbons and alcohols, which have a larger number of modes, may be more likely to be identified than smaller molecules like methane, which have fewer modes.

In-situ nanoscale SERS (Fig. 2.4d) shows the surface of the photocatalyst to be abundant in multi-carbon hydrocarbons and alcohols, which are kinetically challenging to produce in CO_2RR. In electrocatalytic CO_2RR on Ag,[128,129] H_2—formed by competing HER—and CO[130,131] are the most common bulk products; there are some reports of the observation of formate,[123,131] methane,[132,133] ethylene,[134] methanol, and ethanol,[124] albeit in smaller yields. In our study, in addition to these previously reported products, we detected on the surface C_2 compounds such as ethylene glycol, glyoxal, glycolaldehyde, and oxalic acid; C_3 compounds such as propane, propanol, and acetone; and the C_4 compound, butanol. There are no previous reports of the formation of C_3 or C_4 products in Ag catalyzed-CO_2RR. These higher hydrocarbons and alcohols have been reported on other metal catalysts and under special conditions such as high-pressure electrochemistry.[116,135–159] Another species of note detected in our study is oxalic acid (Fig. 2.16c), which is known to be formed in photosynthesis. The dominance of multi-carbon species in the distribution (Figs. 2.4c, 2.4d, and 2.30) leads us to infer that C–C coupling is favorable on the plasmon-excited NP surface.

The formation of the wide variety of C_{2+} chemical species on a Ag NP surface in the presence of visible light excitation and water, without an applied potential, is striking. The atypical profile of multiplex species found here may be an outcome of one or more unique features of our methodology. First, the higher surface sensitivity of SERS combined with the 200 ms temporal resolution and nanoscale sampling volume employed here is quite unlike the bulk-level characterization methods used previously. Secondly, the catalytic activation method utilized in this study is considerably different from the typical conditions in photocatalytic or electrocatalytic CO_2RR. Under the focused plasmonic excitation with an intensity of ~10^8 W.m^{-2} we use, the average time between absorbed photons is ~700 fs (Table 2.46), which is shorter than the 1-ps-scale time constant[160] of electron–hole recombination. These conditions can favor multiphoton excitation and re-excitation of electron–hole pairs (Fig. 2.31), resulting in the generation of highly energetic carriers (Fig. 2.31) akin to those generated by UV light. Such effects may be responsible for the richer photochemistry observed here. While a product profile that is abundant in high-value hydrocarbons and alcohols is desirable, it must be acknowledged that what is measured in these experiments are trace amounts of species generated on the surface that do not necessarily survive or culminate into the bulk product profile. However, there is a possibility that by appropriate engineering of the Ag NP catalyst and the reaction conditions, it may be possible to scale-up the formation of these promising multi-carbon species and recover them as products in the bulk phase.

These findings highlight the potential of in-situ nanoscale SERS probing for providing insights into elementary reaction steps and species prevalent on a photocatalyst surface under operando conditions. This insight, which is typically inaccessible by conventional bulk-level interrogation of heterogeneous catalysts, is made possible by the high spatiotemporal resolution, surface-sensitivity, and reliability of our approach. Noble metals that are effective SERS substrates are naturally suited for highly sensitive interrogation by SERS; however, the method has potential to be extended[161] to other classes of catalysts and photocatalysts. A finding of general importance made here is that the profile of surface species formed under catalytic conditions can differ dramatically from the expected profile of products the catalyst is known to yield. This knowledge will guide more accurate computational modeling, advance mechanistic understanding of the catalytic process, and revolutionize the way catalysts are designed, especially for multi-step, multi-pathway reactions such as CO_2RR.

2.5. METHODS

2.5.1. Sample preparation for surface-enhanced Raman scattering (SERS) experiments

Synthesis of Ag nanoparticles (NPs). Ag NPs for the SERS studies were synthesized by the Lee–Meisel method.[105] Briefly, 45 mg of $AgNO_3$ was added to 250 mL of boiling deionized (DI) water. A solution of trisodium citrate was prepared by dissolving 50 mg of the compound in 5 mL of DI water under stirring. After 5 min of stirring, the entire 5 mL of the citrate solution was added to the $AgNO_3$ solution under stirring. Boiling of the mixture was continued for 1 h. After the addition of the citrate solution, the mixture started changing its color from bright yellow to greenish yellow. This Ag colloid was then allowed to cool to room temperature and stored in fridge. The measured extinction spectrum of the as-synthesized Ag NP colloid is shown in Fig. 2.5.

Preparation of microfluidic reaction cells. SERS-based tracking of plasmon-excitation-driven CO_2 reduction reaction (CO_2RR) events was performed using a microfluidic reaction cell. To construct a microfluidic cell (Fig. 2.7), holes of 1 mm diameter were drilled in a glass coverslip (24×60 mm^2, VWR SuperSlips, no. 1). The coverslip was cleaned by sonication in deionized (DI) water for 10 min and then dried in air. Then, 10 µl of as-synthesized Ag NPs, diluted by the addition of 1 mL of DI water, was drop casted onto the coverslip, which was then heated on a hot plate for drying. This procedure has been optimized to obtain well-isolated Ag NP scatterers suitable for our single-NP-level SERS studies. After multiple rinses with DI water and drying under N_2, this NP-coated coverslip was exposed to ultraviolet (UV) light from a Hg lamp for ca. 10 min to remove any organic contaminants and ligands by UV photo-oxidation. This cleaning procedure ensures that Ag NPs are free of ligands, which would otherwise complicate SERS spectra, and have accessible active surfaces for catalysis. Representative examples of a SERS spectrum from an "unclean" NP scatterer (with surface-adsorbed citrate ligands) and a "clean" NP scatterer (with no surface-adsorbed citrate ligands or other contaminants) are shown in Fig. 2.12a. The length of the UV light treatment was optimized by multiple trials so that the NPs exhibit ligand-free SERS spectra while ensuring that the Ag NP surfaces do not get photo-oxidized, which would mar their catalytic activity. After UV light exposure, the NP-coated coverslip was rinsed with DI water and dried in air. Then the coverslip was placed onto another clean coverslip (24×60 mm^2, VWR SuperSlips, no. 1 with no drilled holes) spaced by double-sided tape, which has a thickness of 10s of μm, and glued using an epoxy glue to form the microfluidic cell.

2.5.2. SERS experiments

Assessment of cleanliness of Ag NPs. For reliable SERS study of plasmon-excitation-driven CO_2RR on Ag NPs, the NPs must have clean surfaces. Although we employed UV photo-oxidation to clean the NP surfaces, it was important to assess the resulting cleanliness. For such an assessment, a separate set of studies was performed where SERS spectra were acquired from individual Ag NP scatterers in CO_2 -untreated DI water. The microfluidic reaction cell was filled with DI water by using a syringe to inject DI water through the drilled holes. The cell was then mounted on the stage of a Olympus IX51 inverted microscope. Spatially isolated scatterers were identified by dark-field scattering imaging. Once an individual scatterer was identified, it was subjected to a 9–10 mW beam of a continuous-wave (CW) 514.5 nm laser focused using a 60× Olympus UPlanApo water immersion objective. At the same time as the laser excitation was turned on, started the continuous acquisition of SERS spectra from the scatterer. SERS spectra were collected using the same objective and filtered by a ca. 530 nm long-pass emission filter before being dispersed by a Princeton Instruments Acton SP2300 spectrometer equipped with a 300 g.mm^{-1} grating. The dispersed light was then detected in a spectrally resolved manner by a Princeton Instruments Pylon 100B liquid nitrogen-cooled charged coupled device (CCD). Using the software Winspec, a 500-frame-long movie of SERS spectra (scattered intensity vs. wavelength) was collected with an acquisition time of 200 ms per frame. In Winspec, the wavelength of the scattered light, in nm units, was converted into a Raman shift in wavenumber (cm^{-1}) units. In this manner, 105 individual Ag NP scatterers were interrogated. These spectral movies from all scatterers interrogated were analyzed to determine the presence of surface ligands and/or contaminants on the NP scatterers. The statistics from this analysis are shown later. To serve as examples, for a few cases, the time-series of continuously acquired SERS spectra from an individual scatterer is plotted as a spectrogram (Figs. 2.1b and 2.13), which is a color-coded map of the intensity plotted as a function of Raman shift and time on the x and y axes respectively. Prior to plotting, the SERS spectrum at each time-point was normalized to a [0, 1] scale.

Statistics showing the cleanliness of Ag NPs after UV light illumination

Cleanliness of individual scatterers

- Total number of individual scatterers investigated = 105
- Number of scatterers with at least one unclean spectral frame = 12
- Number of scatterers with no unclean spectral frames = 93.

- Percentage of such fully clean scatterers = 89 %

Cleanliness of spectral frames

- Total number of spectral frames investigated = 105 scatterers x 500 frames = 52,500 frames
- Number of unclean frames = 738
- Percentage of clean frames = 98.6 %

Degree of cleanliness of scatterers with at least one unclean frame

- Total number of frames acquired from scatterers with at least one unclean frame = 12 scatterers × 500 = 6,000 frames
- Number of unclean frames = 738
- Percentage of clean frames acquired from scatterers with at least one unclean frame = 88 %

SERS studies of CO_2RR activity of Ag NPs. For in-situ SERS studies of plasmon-excitation-driven CO_2RR on Ag NPs, the following procedure was employed. The microfluidic cell bearing the cleaned NPs immobilized on a glass coverslip was filled with DI water, which had been saturated with CO_2 or $^{13}CO_2$ by bubbling CO_2 (99.999 % purity) or $^{13}CO_2$ (<3 atom % ^{18}O, 99.0 atom % ^{13}C) gas, respectively, through it for 20 min at a flow rate of 15–20 cc min^{-1}. The reaction medium prepared in this manner has a bulk pH of ~4.4.

The liquid-filled cell was mounted onto the stage of an Olympus IX51 inverted microscope. First, a spatially isolated Ag NP scatterer was identified by dark-field scattering imaging. A 9–10 mW beam of a 514.5 nm laser line was focused onto the identified scatterer using a 60× Olympus UPlanApo water immersion objective. At the same time as the laser excitation was turned on, started the continuous acquisition of SERS spectra from the scatterer. Spectra were collected using the same objective and filtered by a ca. 530 nm long-pass emission filter before being dispersed by a Princeton Instruments Acton SP2300 spectrometer equipped with a 300 g.mm^{-1} grating. The dispersed light was then detected in a spectrally resolved manner by a Princeton Instruments Pylon 100B liquid nitrogen-cooled charged coupled device (CCD). Using the software Winspec, 1000-frame-long movies of SERS spectra (scattered intensity vs. wavelength) were collected with an acquisition time of 200 ms per frame. In Winspec, the wavelength of the scattered light, in nm units, was converted into a Raman shift in wavenumber (cm^{-1}) units. In a typical SERS experiment performed in CO_2 or $^{13}CO_2$-saturated water, acquired spectra showed considerable dynamics in the fingerprint region (500–1800 cm^{-1}): as a function of time, vibrational bands in the spectra fluctuated in intensity and certain vibrational bands appeared and disappeared. This dynamics is indicative of the formation of transient species and intermediates, i.e., photodriven CO_2RR activity, on the NP surface.

2.5.3. Data analysis

Density functional theory (DFT)-computed Raman spectra. Raman spectra of all the species in the database were calculated by DFT implemented on the software, Gaussian 09.[162] The molecular structure of the species was constructed in Gaussian and then its geometry was optimized by DFT using the B3LYP functional and the 6311G++ (d, p) basis set. The Raman spectrum (harmonic frequencies) of the optimized structure was calculated using the same functional and basis set. All the calculations were performed for structures that correspond to gas phase species at a temperature of 298.150 K and a pressure of 1 atm. Calculations were performed for the normal (^{12}C) and the heavy (^{13}C) isotopologs of each species. DFT-computed frequencies of Raman vibration modes are listed in Tables 2.2–2.24 species-by-species. Mode frequencies for the ^{12}C isotopolog are listed in the leftmost column and those for the ^{13}C isotopolog are listed in the rightmost column of each table. These tabulated frequencies were used for the assignment of experimental SERS spectra to species.

SERS peak analysis. To determine peaks in acquired SERS spectra associated with vibrational modes, we subjected the spectra to derivative analysis in MATLAB. Each raw spectrum (intensity as a function of the Raman shift) was first smoothed in the software MATLAB using a Savitzky–Golay filter with a window size of 5 and the order of the polynomial set to 1. Then the first derivative of the intensity was calculated. The derivative spectrum was also smoothed using a Savitzky–Golay filter with window size of 5 and an order of the polynomial of 1. The wavenumber locations of peaks in the acquired spectrum were determined by identifying all zero-crossing points in the smoothed derivative spectrum that match two criteria. First, the zero-crossing point ought to lie on a negative-slope region of the derivative spectrum. Second, this negative-slope region ought to begin at an intensity that is above a threshold set to 3× the standard deviation of the scattering intensity of the smoothed derivative spectrum calculated between 4000–7000 cm^{-1}, where no vibrational modes are observed and only noise contributes to the spectrum.

Spectral assignment. Once the wavenumber locations of all peaks in a SERS spectrum were determined, these wavenumbers were compared with the DFT-calculated Raman frequencies of vibrational modes of all species in our database. A peak is considered to correspond to a vibrational mode if the wavenumber location of the peak lies within a tolerance range of ±10 cm^{-1} around the DFT-computed Raman frequency of the mode. A spectrum is assigned to a species if 3 or more peaks in the SERS spectrum correspond to the Raman vibrational modes of that species. This method was followed to analyze and assign over 98,000 spectra acquired from the 96 single-NP-level scatterers interrogated across multiple experiments. Note that relative intensities of vibrational peaks in a DFT-computed Raman spectrum do not model the relative intensities of vibrational peaks in a corresponding SERS spectrum; hence, only the peak locations are used for assigning a measured spectrum to a species.

The reference database consists of simple C_1–C_4 hydrocarbons, alcohols, and oxygenates. Naturally these species are similar in terms of the functional groups and bonding motifs they contain. So, there is potential for spectral overlap between vibrational features of different species, especially given the considerable size of the database. It was necessary to ensure that such spectral overlap does not affect the reliability of our spectral assignments. The algorithm we used considers the appearance of a peak in the experimental SERS spectrum within a ±10 cm^{-1} range around the DFT-computed frequency of a Raman mode to be a mode-match. For a spectrum to be assigned to a particular species, a minimum of three such matches between the experimental SERS spectrum and the DFT-computed Raman spectrum is required. Note that we did not require a match between all modes of a species, because not all DFT-computed Raman vibration modes necessarily appear in an experimental spectrum corresponding to a species. The three-mode-match threshold we use reduces the effect of potential overlap between modes of different species and increases the likelihood of a unique assignment of a spectrum. In a subset of the cases, a spectrum gets assigned to more than one species, in which case all these species are deemed to be detected. Manual assignment of a set of 500 experimental SERS spectra showed that automated spectral assignment based on the aforementioned criteria is reliable. It must be noted that the three-mode-match assignment method is inappropriate for finding spectra which capture CO because CO has only one vibrational mode. Therefore, for identifying spectra containing the CO mode, we ran a separate analysis for the full set of spectra obtained with $^{12}CO_2$-saturated water using the method described above but with a single mode-match criterion and an increased tolerance of ±100 cm^{-1}.

2.5.4. Potential energy distribution (PED) analysis

The interpretation of DFT-computed Raman spectra and the assignment of vibrational frequencies to various local bond vibrations were performed by a PED analysis. This analysis was performed using the vibrational energy distribution analysis (VEDA) program.[163, 164] A normal vibrational mode of a polyatomic molecule is typically a superposition of multiple local stretching, bending, and torsion motions of smaller fragments of the molecule. PED analysis helps us quantitatively assess the contributions of these local motions to a normal mode of vibration. In this analysis, the co-ordinate of a normal mode of vibration is represented as a superposition of various local mode co-ordinates. The VEDA program uses output files from Gaussian and proposes an introductory set of possible local mode co-ordinates comprising a normal mode of vibration. The combination of local mode co-ordinates is then optimized by the program. VEDA outputs the % contribution of a local mode co-ordinate to the potential energy function of a normal mode. In the following tables (Tables 2.2–2.24), alongside each vibrational frequency, the dominant local mode/s and their % PED contribution to the frequency are listed in the second column. Positive values indicate symmetric modes and negative values indicate antisymmetric modes of vibration. The following symbols are used to indicate various vibrational modes: ν-stretching; δ-bending; ρ-rocking; τ-twisting; ω-wagging; ϕ-torsion.

2.5.5. SERS spectra of surface species detected

In Fig. 2.2, examples of measured SERS spectra corresponding to methanol, acetic acid, acetone, and butanol are provided. Representative examples of measured SERS spectra for the other species detected in plasmon-excitation-driven CO_2RR are shown below in Figs. 2.15–2.23. These examples were found from 42,000 in-situ SERS spectra collected from 40 individual Ag NP scatterers in $^{12}CO_2$-saturated water under plasmonic excitation.

2.5.6. Isotopological shifts and spectral barcodes

By use of ^{13}C-labeling, we attempted to confirm whether C_1–C_4 surface species detected in SERS spectra are indeed formed by CO_2RR. Species generated from $^{13}CO_2$ are expected to have vibrational spectra with their mass-sensitive modes shifted in frequency with respect to the ^{12}C isotopologs. For each species detected in experimental SERS spectra, we determined these isotopological shifts from SERS spectra measured in $^{12}CO_2$-saturated water and $^{13}CO_2$-saturated water. We compared these measured shifts with those estimated from DFT-computed Raman spectra.

Isotopological shifts. From experiments conducted in $^{12}CO_2$–saturated water, all SERS spectra corresponding to a particular species were grouped together. From each experimental SERS spectrum, the peak wavenumbers (cm^{-1}) of the key vibrational modes were determined (Fig. 2.24). Note that the key vibrational modes were identified on the basis of DFT-computed Raman frequencies. Then, for each mode, we determined the average and standard deviation (SD) of the peak wavenumber, $\nu(^{12}C)$, across the entire set of experimental spectra corresponding to this species. The same procedure was followed for the set of SERS spectra corresponding to this species acquired in $^{13}CO_2$–saturated water. The latter yielded for each mode, the average and SD of the peak wavenumber, $\nu(^{13}C)$, for the heavier isotopolog. We then determined the experimental isotopological shift, $\nu(^{13}C) - \nu(^{12}C)$, and the SD in this shift for all key modes for each species. The SD in the measured isotopological shift of a mode was calculated as $\sqrt{\sigma_{12C}^2 + \sigma_{13C}^2}$, where σ_{12C} and σ_{13C} are the standard deviations in the peak wavenumbers of the mode as determined from experimental SERS spectra of the ^{12}C and ^{13}C isotopologs, respectively. These experimentally measured isotopological shifts were then compared with corresponding DFT-computed isotopological shifts for each species, as shown in Tables 2.25–2.45.

Note that the averaging procedure described above only utilized wavenumber locations of vibrational peaks in spectra; peak intensities were disregarded because they do not provide any information on the isotopological shift.

Construction of spectral barcodes. For visualization of the isotopological shifts, measured SERS spectra of ^{12}C and ^{13}C isotopologs of each species are plotted in the form of spectral barcodes (Figs. 2.3 and 2.25–2.29). To construct a spectral barcode for a species, we plotted along the x-axis unit-height vertical lines corresponding to the average peak wavenumber locations of the key vibrational modes for that species. These average peak wavenumber locations were determined from experimental SERS spectra, as described in the previous paragraph. The spectral barcodes for the ^{12}C and ^{13}C isotopologs of each species were overlaid for visualization of the experimentally measured isotopological shift. The number of experimental SERS spectra that were used to construct a barcode is listed in each case. Reference barcodes were also constructed from the DFT-computed Raman spectra of the ^{12}C and ^{13}C isotopologs of the species and overlaid for visualization of the DFT-computed isotopological shift. Fig. 2.24 depicts the procedure for the construction of spectral barcodes with the aid of the example of propane.

2.5.7. Analysis of photon flux

Under the continuous-wave (CW) laser excitation conditions employed in our SERS experiments, we estimated the average time between individual photon absorption events by a Ag NP scatterer to be 690 fs (Table 2.46). We assumed the scatterer to be a dimer of 60-nm diameter spherical Ag NPs, which has an estimated absorption cross-section, σ, of 5.12 x 10^{-15} m^2 at 514.5 nm.[45]

2.5.8. Calculation of temperature rise resulting from photothermal heating

Under CW laser excitation, a Ag NP scatterer will undergo photothermal heating. As a result of this heating, the NP surface is expected to be at steady-state temperature that is higher than the bulk temperature of the ambient medium by an amount ΔT. We estimated ΔT under our experimental conditions: CW excitation with a 514.5 nm laser with a power of 10 mW and a beam diameter of 10.8 μm. The focused laser spot excites only a discrete scatterer at a time, since scatterers on the substrate are well separated from one another (Figs. 2.8 and 2.9). Therefore, we use an expression obtained from the steady-state heat-balance analysis of a single absorbing entity:[45, 165]

$$\Delta T = \frac{\sigma I}{4\pi r \kappa} \qquad (1)$$

In this equation, I is the laser intensity estimated to be 1.09 x 10^8 W.m^{-2} (Table 2.46). σ is the absorption cross-section of the absorbing entity, which we assume to be a dimer of 60-nm diameter Ag NPs[45] for a reasonable representation of a typical scatterer interrogated in our studies (Figs. 2.8–2.11). σ for a dimer of 60-nm diameter Ag NPs has an estimated value of 5.12 x 10^{-15} m^2 at the excitation wavelength of 514.5 nm.[45] r is the radius of the absorber, which is effectively 37.8 nm based on the total volume of the dimer. κ is the thermal conductivity of the surrounding medium, which has a value of 0.6 W.m^{-1}.K^{-1} for water, which overlies the NP dimer, and a value of 1.2 W m^{-1} K^{-1} for the borosilicate glass coverslip that underlies the NP dimer. For the worst-case scenario of photothermal heating, we use the lower value of κ. Substituting these values into equation 1, ΔT is determined to be 2 K. In other words, the steady-state local temperature at the surface of the NP scatterer is 2 K higher than the bulk temperature (296 K) of the aqueous medium. Alternatively, we make an estimate using an effective thermal conductivity, κ_{eff}, that is a simple average of the κ values of glass and water. In such a case, κ_{eff} is 0.9 W. m^{-1}. K^{-1} and the estimated temperature rise is 1.3 K. Such a small photoinduced temperature rise (2K or smaller) cannot be assigned responsibility for the observed CO_2RR activity.[166]

2.6. FIGURES

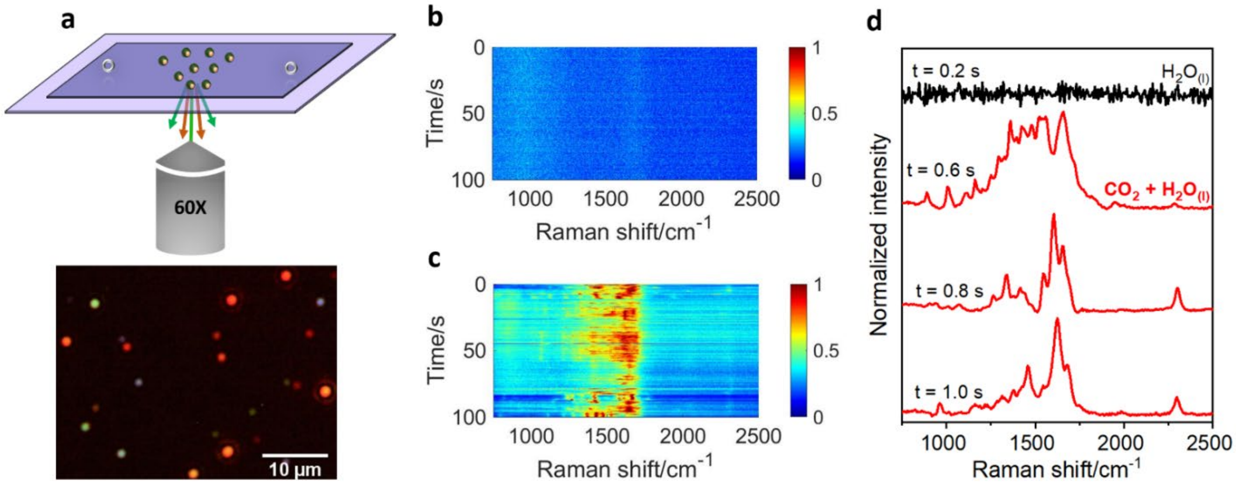

Figure 2.1. In-situ SERS probing of plasmon-excitation-driven CO_2RR in an aqueous medium. a) Top panel shows a schematic of the single-NP-level SERS spectroscopy setup used for probing CO_2 photochemistry on a Ag NP in water, i.e., $H_2O_{(l)}$. The Ag NP was immobilized inside a microfluidic cell placed on an inverted optical microscope and subject to continuous-wave focused laser excitation. Raman scattering was continuously collected using a 60× objective. The bottom panel shows a representative dark-field scattering image of the substrate coated with spatially resolvable Ag NP emitters. Representative spectrograms showing a time series of in-situ SERS spectra acquired from an individual Ag NP scatterer in b) CO_2-untreated $H_2O_{(l)}$ and c) CO_2-saturated $H_2O_{(l)}$. The SERS intensity is coded by the color, as indicated by the legend. d) Spectral slice, corresponding to t = 0.2 s, from the plot in b shows the lack of any vibrational modes. Spectral slices, corresponding to t = 0.6 s, 0.8 s, and 1.0 s from the plot in c show the spectral dynamics taking place in the presence of CO_2-saturated $H_2O_{(l)}$ under LSPR excitation. The spectra were normalized to a [0, 1] range prior to plotting in the form of spectrograms in b and c. The spectra were baseline-subtracted and normalized to a [0, 1] range prior to plotting in a vertically-stacked manner in d. The baseline was determined by polynomial fitting.

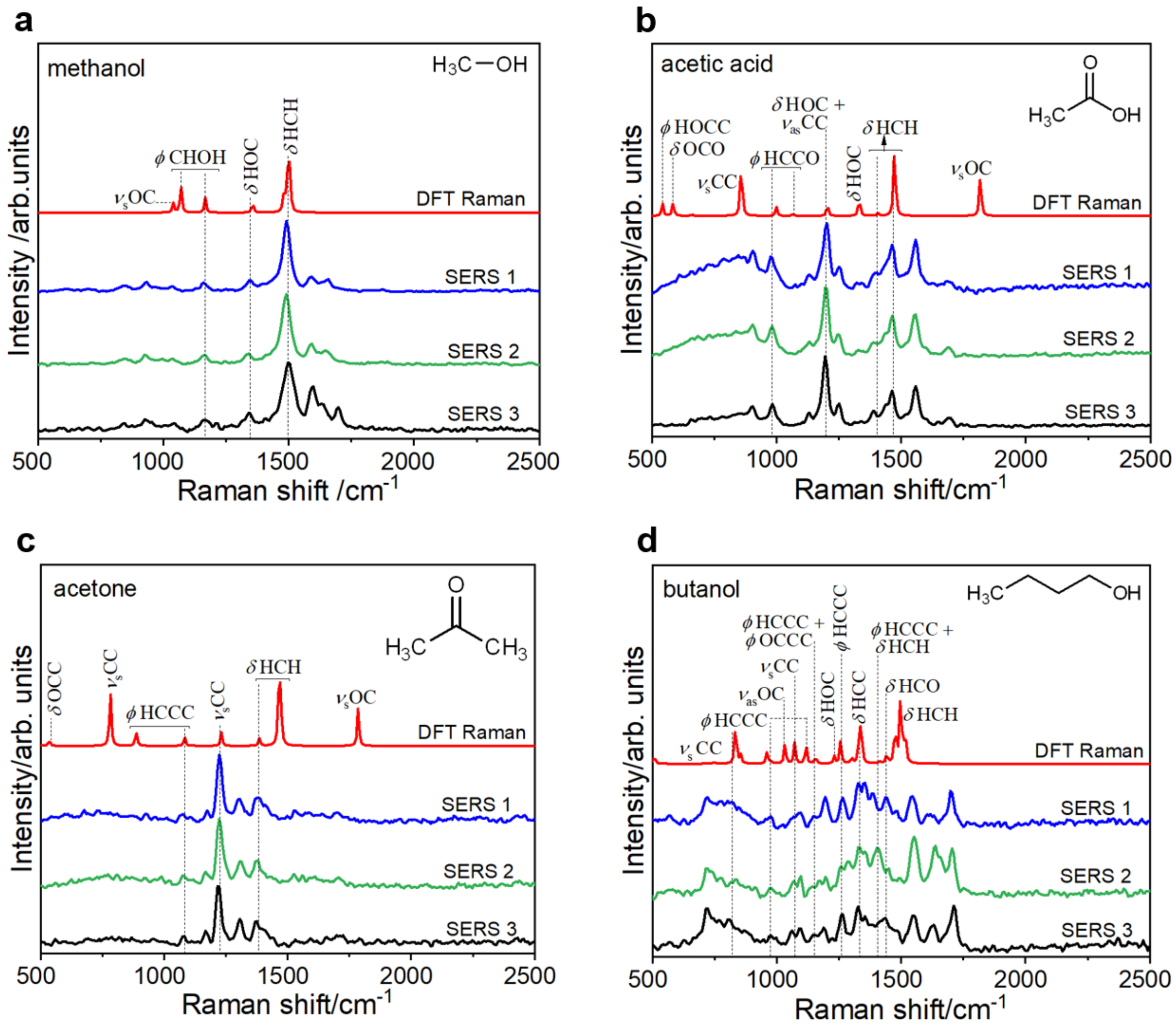

Figure 2.2. Species detected on Ag NPs in the course of plasmon-excitation-driven CO_2RR in water. Three representative examples of measured SERS spectra (blue, green, and black traces) that correspond to the detection of a) methanol, b) acetic acid, c) acetone, and d) butanol. In each case the DFT-calculated Raman vibrational spectrum, which served as the basis of the assignment of the measured SERS spectra, is also shown by the red trace. The major vibrational modes are labeled using the following symbols: ϕ-torsion; ν_s-symmetric stretching; ν_{as}-asymmetric stretching; δ-bending. Spectra are shown vertically stacked for clarity. SERS spectra were baseline-subtracted, subjected to smoothing by the Savitzky–Golay with a window of 5 points and a polynomial of order 3, and normalized to a [0, 1] scale prior to plotting in a vertically-stacked manner. The baseline was determined by polynomial fitting. DFT-computed Raman spectra were normalized to a [0, 1] scale, and the y-axis quantity was magnified (by a scale factor of 4 in panels a and b and a factor of 10 in panels c and d) prior to plotting.

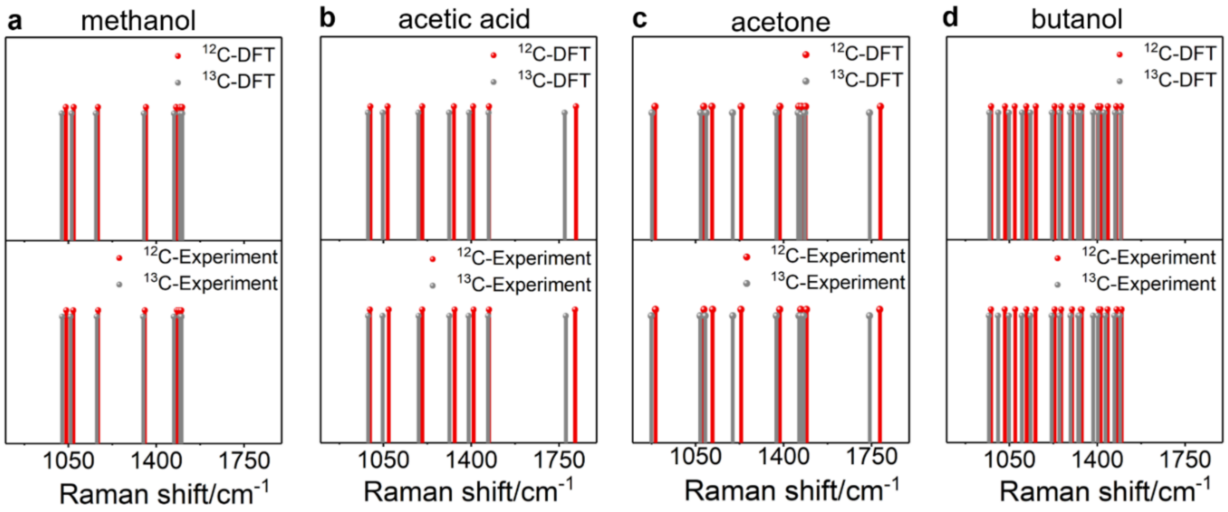

Figure 2.3. Isotopological validation of CO2RR origin of surface species. Spectral barcodes for the DFT-computed Raman spectra (top row) and experimental SERS spectra (bottom row) for ^{12}C (red lines) and ^{13}C (gray lines) isotopologs of a) methanol, b) acetic acid, c) acetone and d) butanol. Each vertical line in a barcode indicates the peak wavenumber of a vibrational mode. The number of SERS spectra that led to the experimental barcodes are a) 119 and 43, b) 106 and 59, c) 243 and 177, and d) 1062 and 836 for the ^{12}C and ^{13}C isotopologs, respectively.

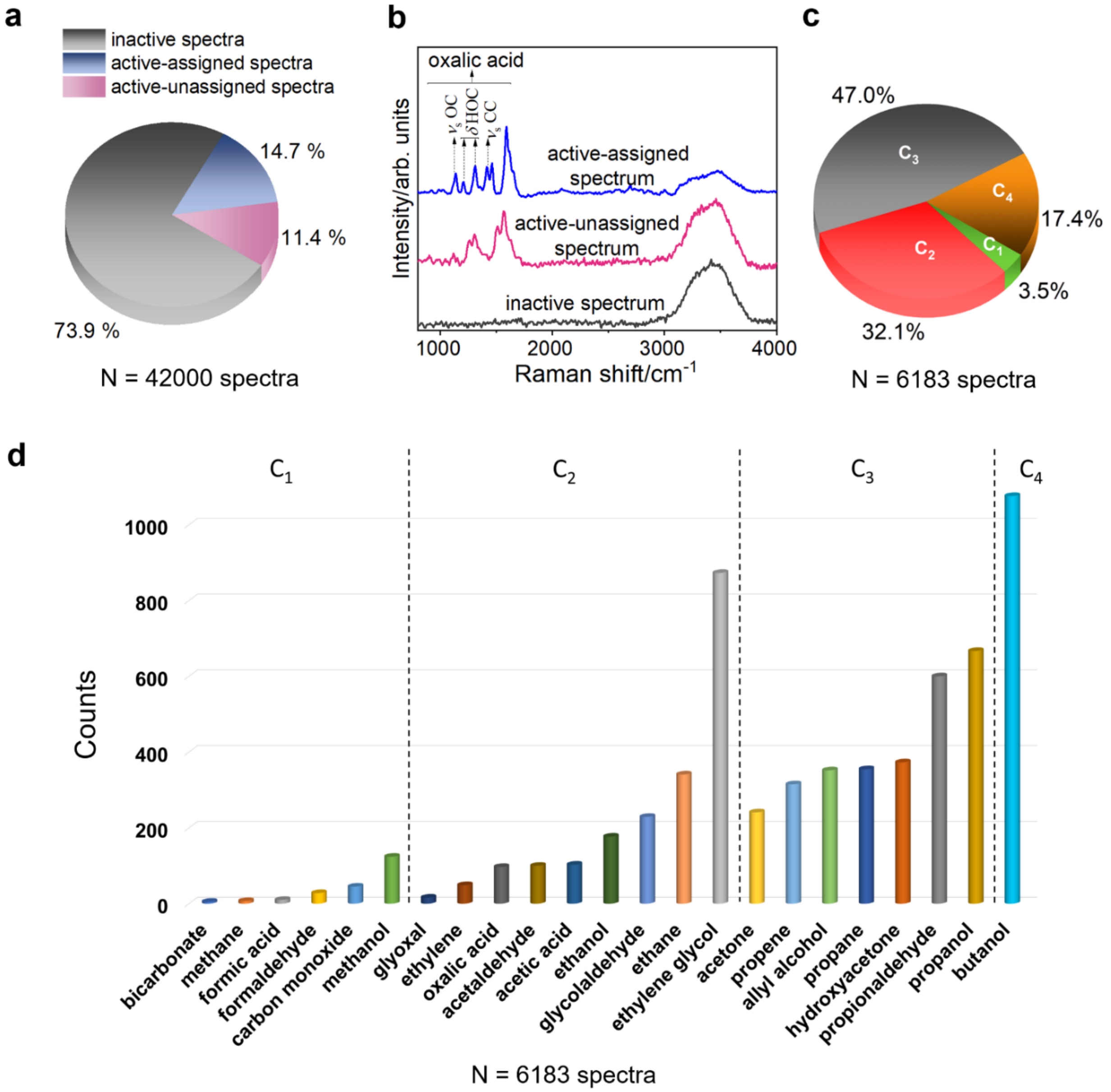

Figure 2.4. Profile of surface species observed in CO_2RR by in-situ nanoscale SERS. a) Pie-chart showing the % distribution of inactive SERS spectra, active spectra that were assigned to a species in the database, and active spectra that were unassignable. This distribution was obtained by an analysis of 42,000 in-situ SERS spectra collected from 40 individual Ag NP scatterers in $^{12}CO_2$-saturated $H_2O_{(l)}$ under plasmonic excitation. b) Representative examples of SERS spectra in each of these three classes, plotted in a vertically-stacked manner. The broad band at ca. 3400 cm^{-1} in all three spectra is due to Raman scattering from $H_2O_{(l)}$ in the medium. The active, assigned SERS spectrum shown as an example captured oxalic acid, the major vibrational modes of which are labeled by the following symbols: ν_s-symmetric stretching; δ-bending. SERS spectra were baseline-subtracted, subjected to smoothing by a Savitzky–Golay filter with a window of 5 points

Figure 2.4. (cont.) and a polynomial of order 3, and normalized to a [0, 1] scale prior to plotting in a vertically stacked manner. The baseline was determined by polynomial fitting. c) Pie-chart showing the percentages of active, assigned spectra that captured a C_1, C_2, C_3, and C_4 species. d) Bar plot showing for each surface species the number of detection events across the set of active, assigned spectra. Each species is shown by a bar of a different color. The species are grouped into C_1, C_2, C_3, and C_4 categories; within each category, they are listed in the order of their prevalence. N in panels a, c, and d represents the total number of spectra that led to the plot.

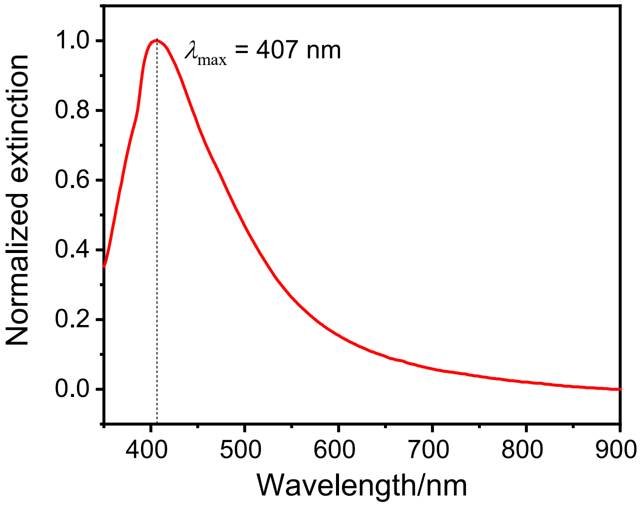

Figure 2.5. Extinction spectrum (normalized to the maximum extinction) of the Ag NP colloid synthesized by the Lee–Meisel method.[105] The spectrum shows the localized surface plasmon resonance (LSPR) band with a wavelength maximum, λ_{max}, at 407 nm (marked by the dotted vertical line).

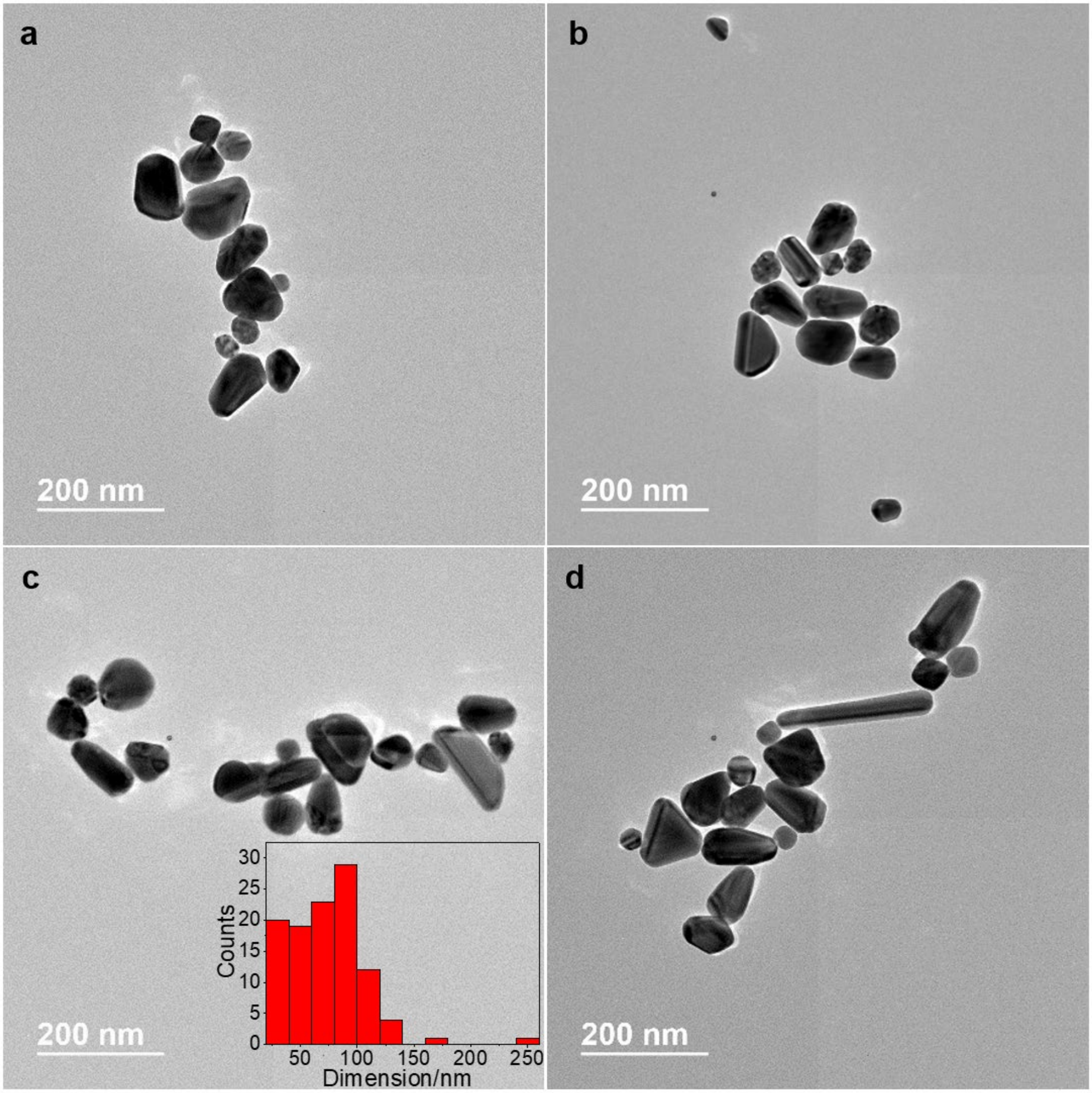

Figure 2.6. Transmission electron microscopy (TEM) characterization of colloidal Ag NPs synthesized by the Lee–Meisel method. A 500 µL volume of the as-synthesized colloid was mixed with 3 mL of DI water. The diluted colloid was drop-casted onto a carbon-coated Formvar film on a 200 mesh Cu TEM grid (Ted Pella) and dried by heating on a hot plate for < 5 min. Images were acquired on a JEOL 2100 Cryo TEM instrument using a 200 kV electron beam. (a–d) Selected TEM images show that the colloid contains NPs of a variety of sizes and shapes. From an analysis of 109 NPs over several images, the longest NP dimension is found to range from 26–244 nm with an average of 74 nm and a standard deviation of 33 nm. The histogram of longest NP dimension is shown in the inset in c.

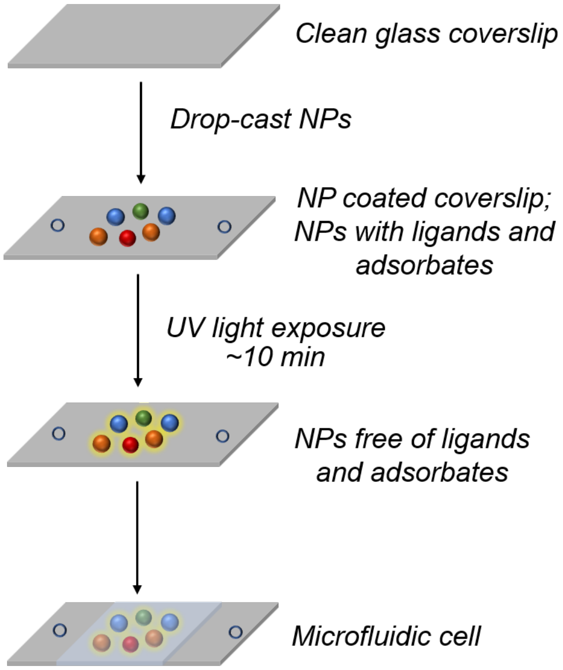

Figure 2.7. Schematic description of the construction of microfluidic reaction cells for SERS experiments.

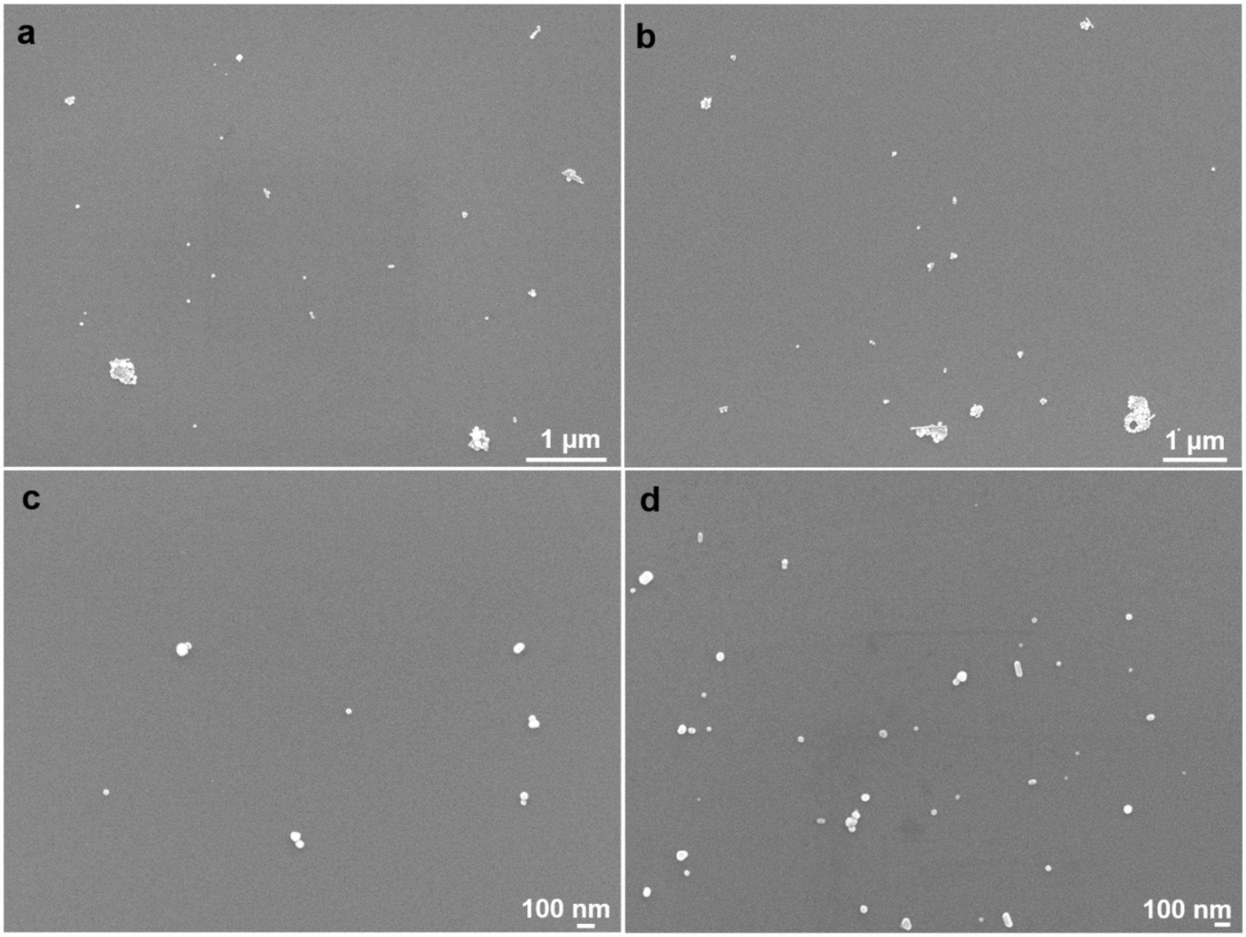

Figure 2.8. Scanning electron microscopy (SEM) characterization of Ag NPs deposited on a substrate using conditions similar to the preparation of samples for the in-situ SERS studies. A 10 μL volume of the as-synthesized Ag NP colloid was mixed with 1 mL of DI water. The diluted colloid was drop-casted onto a Si substrate and dried by heating on a hot plate for < 5 min. Imaging was performed using a JEOL 7000F field emission SEM instrument operated in secondary-electron mode. An accelerating voltage of 15 kV was used for imaging. (a–d) Selected images show the area distribution of discrete deposits formed by the sample preparation method used for our SERS studies. The area-density of NPs deposited is low enough such that discrete deposits well-isolated from one another are formed. The discrete deposits appear primarily to be single NPs, dimers, or trimers from the higher-magnification images in c and d. Some larger NP aggregates are found as well in the lower-magnification images in a and b.

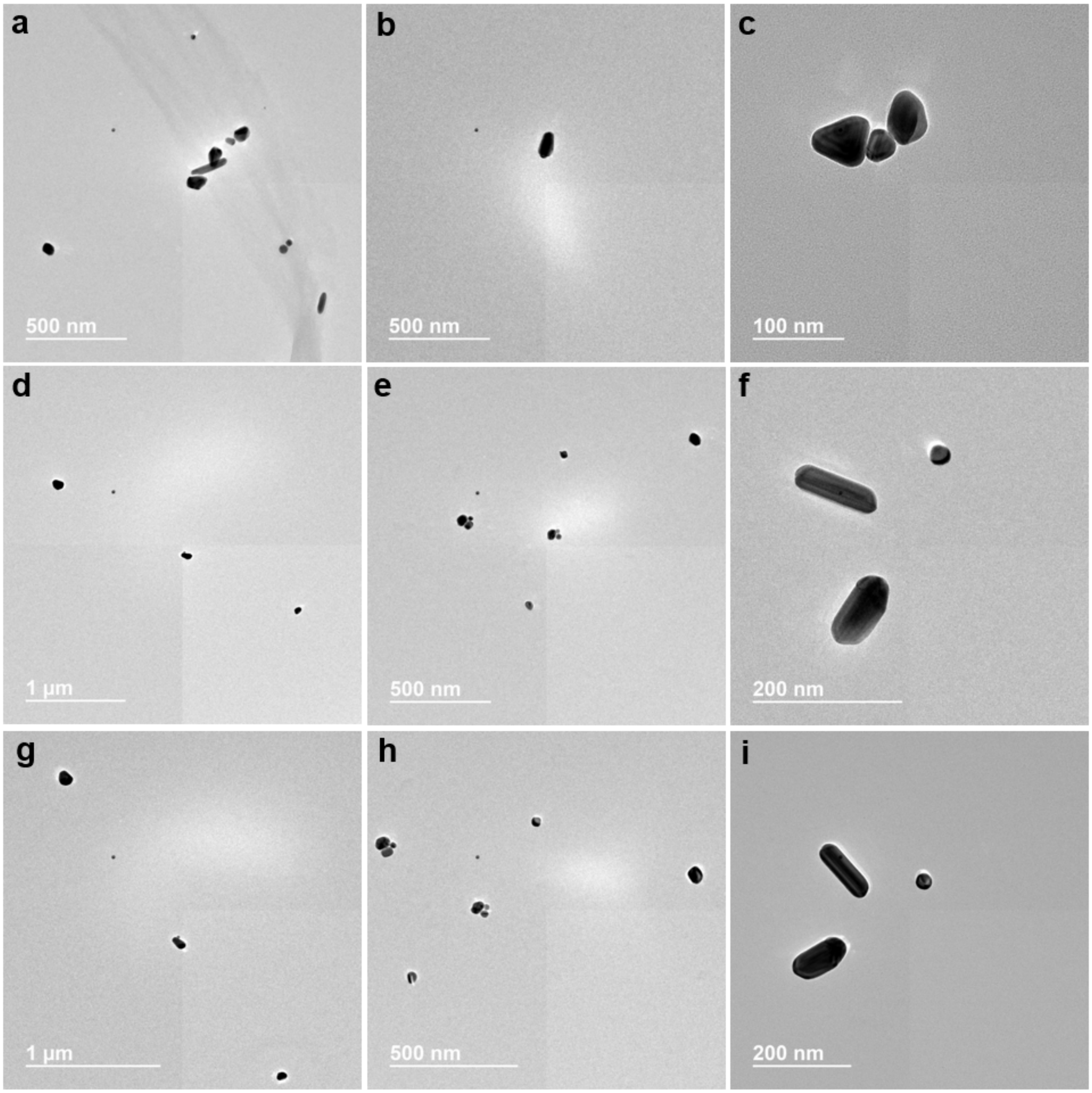

Figure 2.9. TEM characterization of Ag NPs deposited on a substrate using conditions similar to the preparation of samples for the SERS studies. A 10 µL volume of the Ag NP colloid was mixed with 1 mL of DI water. The diluted colloid was drop-casted onto a carbon-coated Formvar film on a 200 mesh, Cu TEM grid (Ted Pella) and dried by heating on a hot plate for < 5 min. Images at multiple magnifications were acquired on a JEOL 2100 Cryo TEM instrument using a 200 kV electron beam. (a–i) Selected TEM images show the area distribution of discrete deposits formed by the sample preparation method used for our SERS studies. Similar to the findings from SEM shown in Figure S4, these TEM images show discrete deposits well-isolated from one another and consisting primarily of single NPs, dimers, or trimers. Some larger aggregates are also present in other regions. The same regions seen in the images in d–f were imaged after subjecting the TEM grid-bearing sample to ~10 min of UV light illumination. The respective images in g–i show that UV light illumination does not induce changes in the area-density or location of deposited NPs.

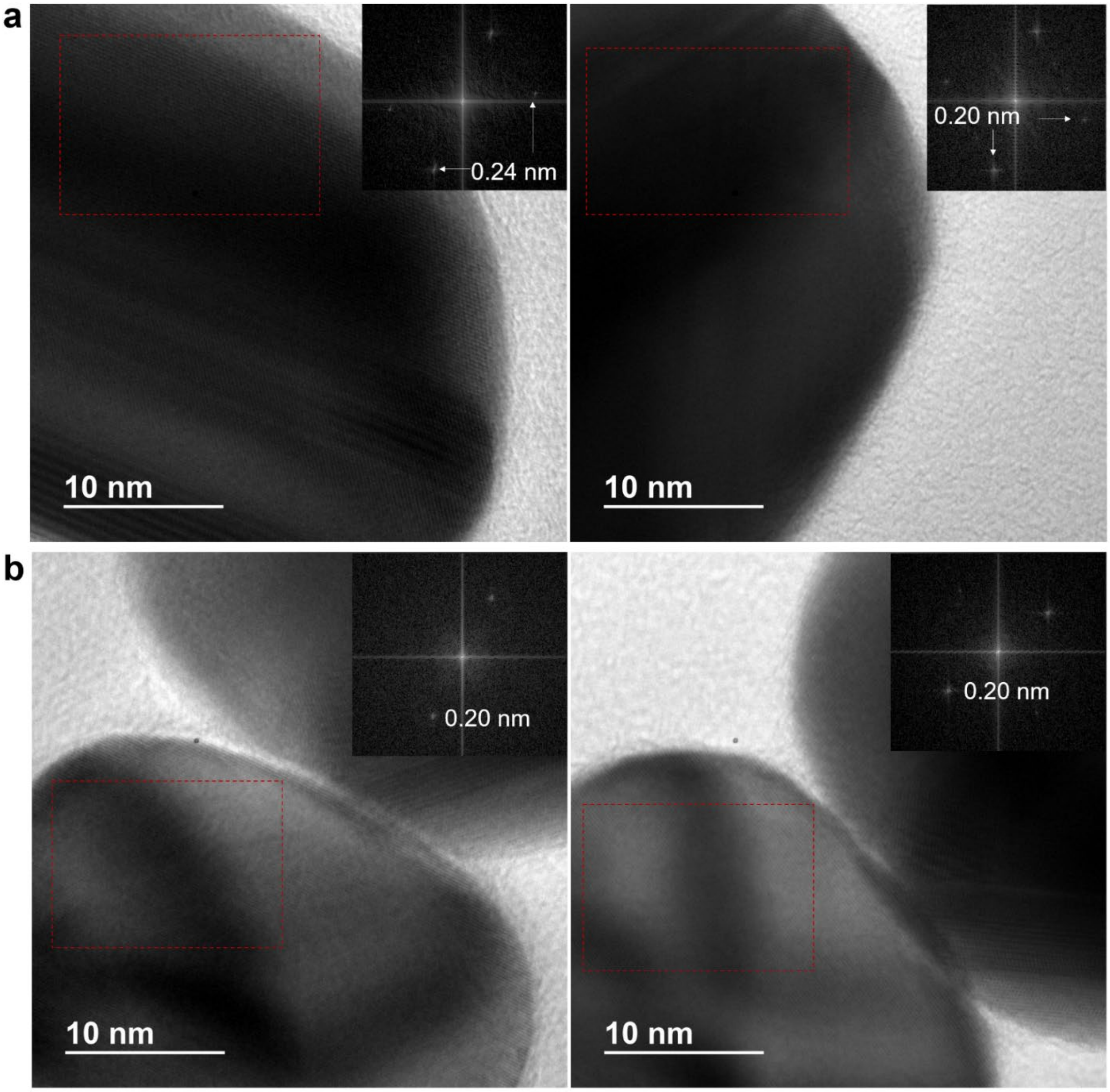

Figure 2.10. (cont.)

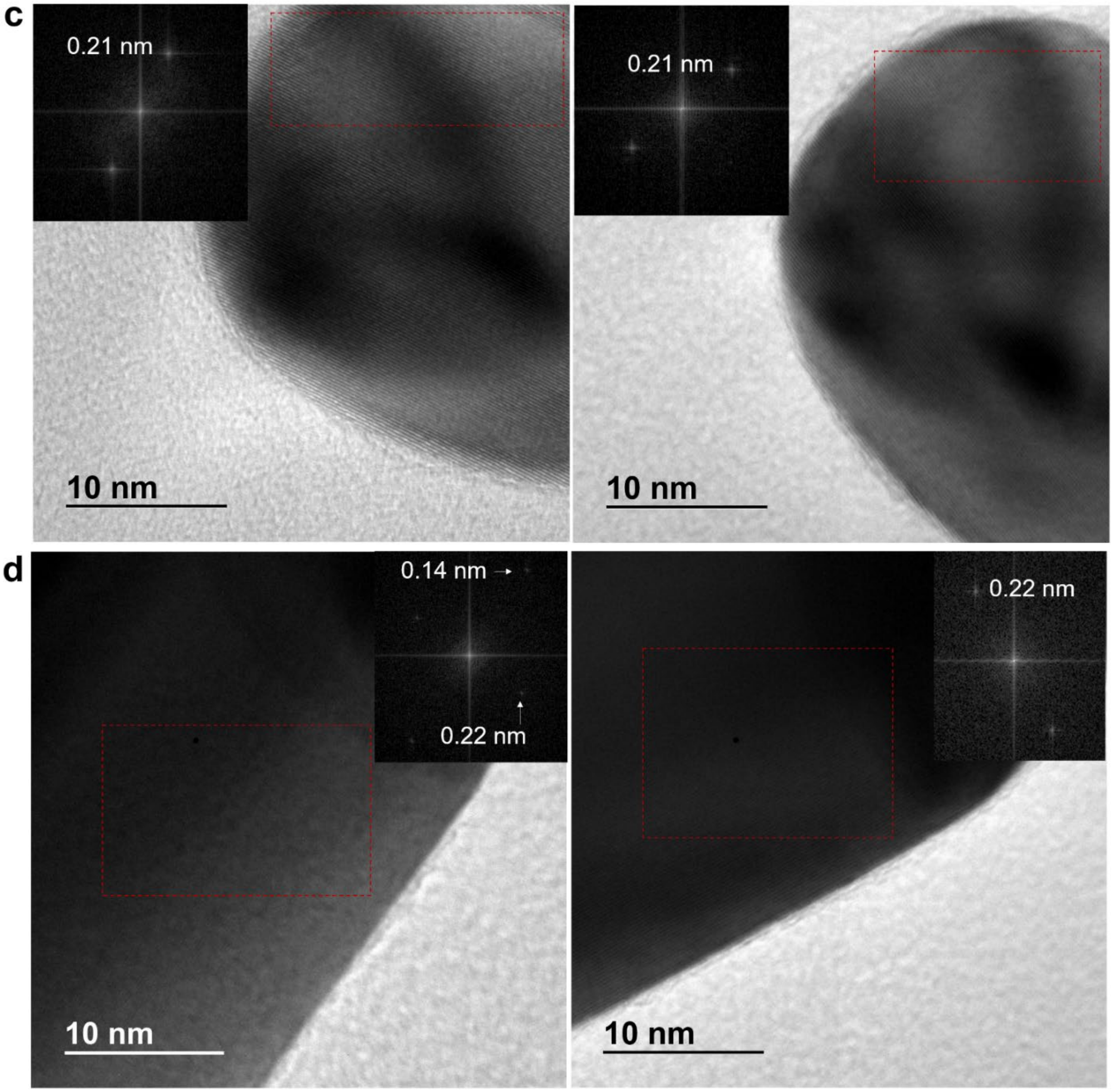

Figure 2.10. High-magnification TEM images of representative NPs before (left column) and after (right column) ~10 min of UV light illumination. In each image, a Fast-Fourier transform (FFT) of a selected area (red box) of the real-space image is shown as the inset. Reciprocal lattice spots at a d-spacing of 0.14 nm (inset of d) correspond to (220) lattice planes of Ag. Reciprocal lattice spots at d-spacings of 0.22 nm (inset of d) and 0.24 nm (inset figure a) correspond to the (111) lattice planes of Ag and those at 0.20 nm (insets in a & b) and 0.21 nm (inset figure c) correspond to the (200) lattice planes of Ag. No oxide shell is found on the Ag NPs subjected to UV light illumination. The morphology of the NPs does not appear to have been modified by UV light illumination. The high-magnification images shown here are from the same study as the one presented in Fig. 2.9. Note the display of each FFT image has been adjusted in ImageJ by setting the brightness/contrast minimum to 100.

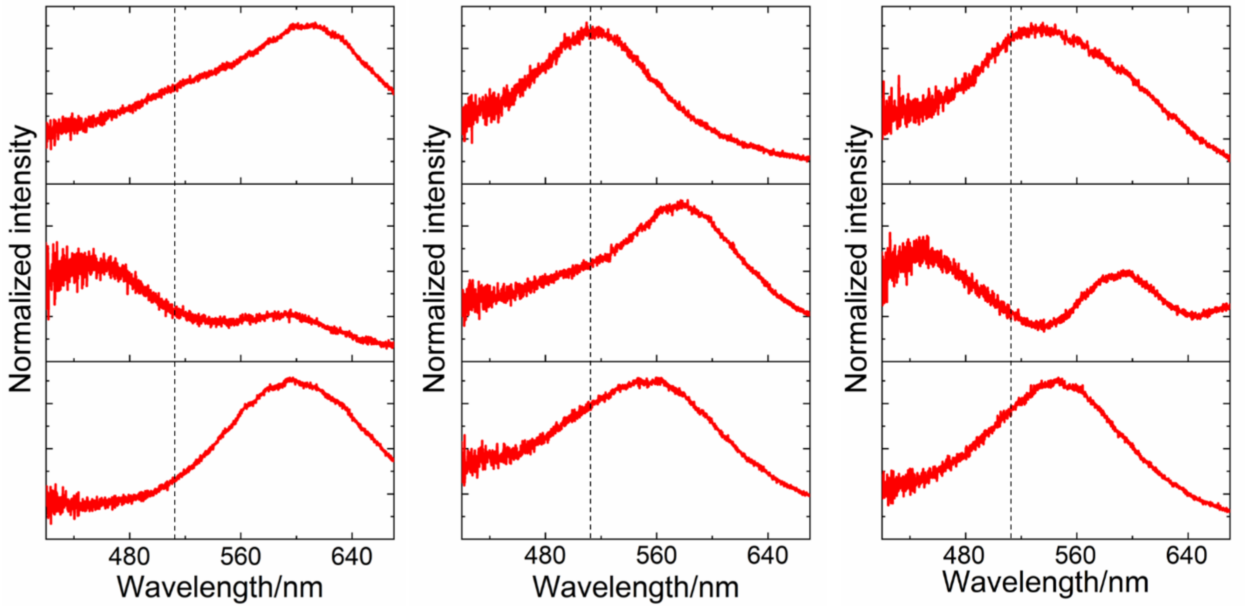

Figure 2.11. Representative dark-field scattering spectra of discrete Ag NP scatterers on a sample prepared using conditions similar to the preparation of samples for the in-situ SERS studies. The scattering spectra of these NP scatterers show broad LSPR peaks centered at wavelengths in the 450–600 nm range. Thus, representative scatterers interrogated in our study possess LSPR bands overlapping with the 514.5 nm laser excitation (vertical dotted line). The scattering spectra also indicate that the scatterers are not single spherical NPs, which would exhibit a simple dipolar LSPR band centered around 400 nm. Instead, a typical scatterer interrogated in our study is an anisotropic NP, a NP dimer, or a few-NP aggregate, as further supported by SEM (Fig. 2.8) and TEM (Fig. 2.9.) characterization of substrate-bound Ag NPs prepared using conditions similar to those used for preparation of samples for SERS studies. The spectra of discrete scatterers were measured using a dark-field microscopy setup under white-light illumination focused using a dark-field (Olympus U-DCW) condenser. The scattered light was collected by a 100× dark-field, oil-immersion objective, dispersed by a spectrograph equipped with a 300 g/mm grating, and spectrally analyzed using a Pylon 100B charged-coupled device (CCD) camera. Acquired spectra were subjected to a subtraction of the dark counts and divided by the dark-count-subtracted spectrum of the white-light source to obtain a scattering spectrum. The scattering spectra were normalized to a [0, 1] range prior to plotting.

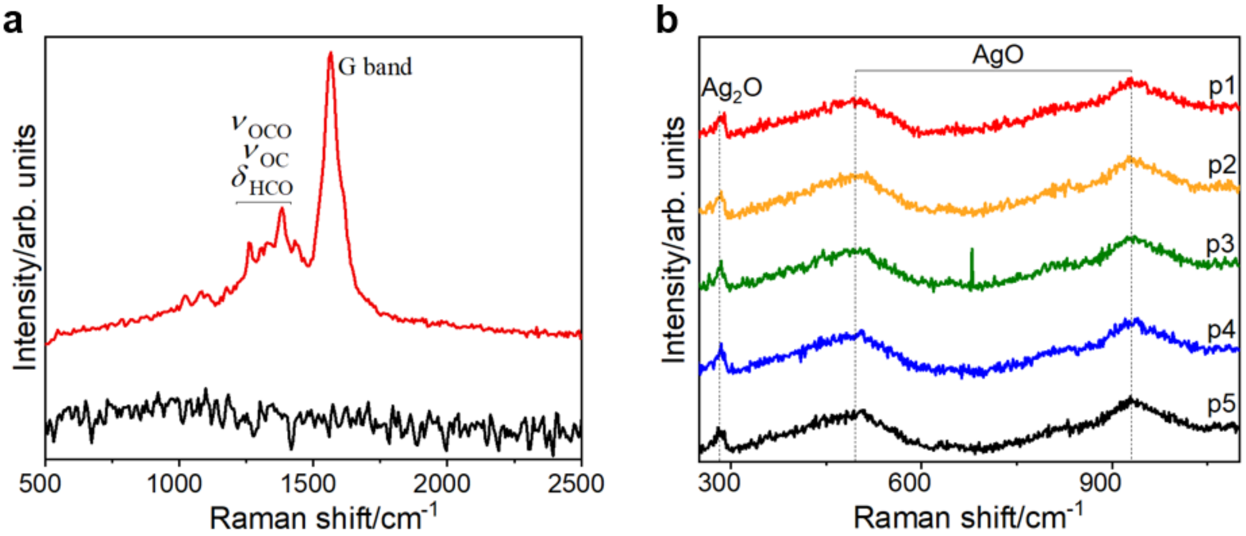

Figure 2.12. a) A representative SERS spectrum of an Ag NP scatterer before (red trace) and after 10 min of UV light illumination (black trace). The spectrum before illumination shows SERS bands corresponding to citrate ligands (as shown by the labeled modes where ν refers to stretching and δ to bending) and adsorbed carbonaceous species (as shown by the labeled G band) on the NP; no bands are observed in the spectrum acquired after 10 min of illumination. The spectra were collected under 9 mW of 514.5 nm excitation with an acquisition time of 1 s (red trace) and 200 ms (black trace). Spectra were normalized to a [0,1] scale and the black trace was smoothed using a Savitzsky–Golay method filter with a window of 5 points and a polynomial of order 3 prior to plotting in a vertically-stacked manner. b) SERS spectra in the low-wavenumber range (250-1100 cm^{-1}) acquired from five discrete scatterers (labeled p1 to p5) on a Ag NP-coated glass coverslip that was subjected to 10 min of UV light illumination. The spectra were collected under 20 mW of 514.5 nm excitation with an acquisition time of 1 min. The vibrational peak (vertical dotted line) at 284 cm^{-1} can be attributed to the presence of AgO.[167] Broad vibrational peaks (vertical dotted lines) centered at 497 cm^{-1} and 930 cm^{-1} can be assigned to Ag_2O.[167, 168] SERS spectra were baseline-subtracted prior to plotting in a vertically-stacked manner. The baseline was determined by polynomial fitting.

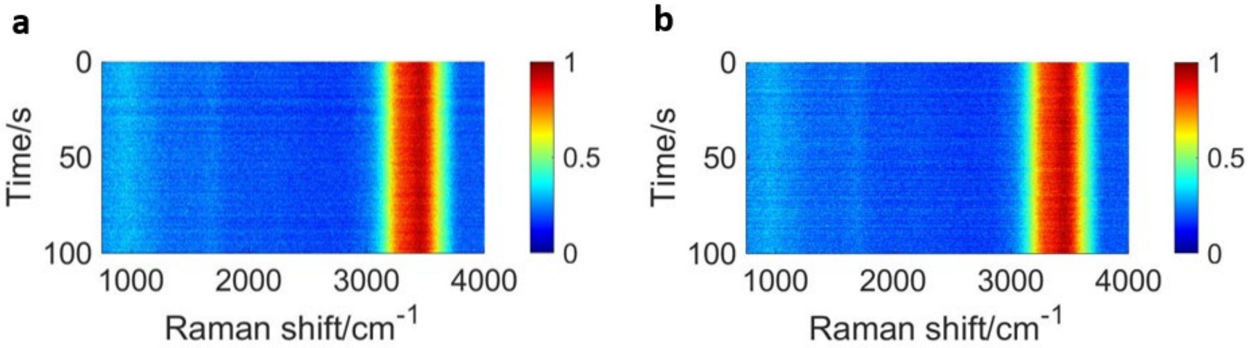

Figure 2.13. Two examples (a and b) of spectrograms showing the time series of in-situ SERS spectra (normalized to a [0, 1] scale at each time-point) acquired from an individual Ag NP scatterer in CO_2-untreated $H_2O_{(l)}$ under plasmonic excitation. The SERS intensity is coded by the color, as indicated by the legend. Except for the broad band at ca. 3400 cm^{-1}, which is due to Raman scattering from $H_2O_{(l)}$ in the medium, there are no SERS bands in the spectra. This shows the cleanliness of the NPs.

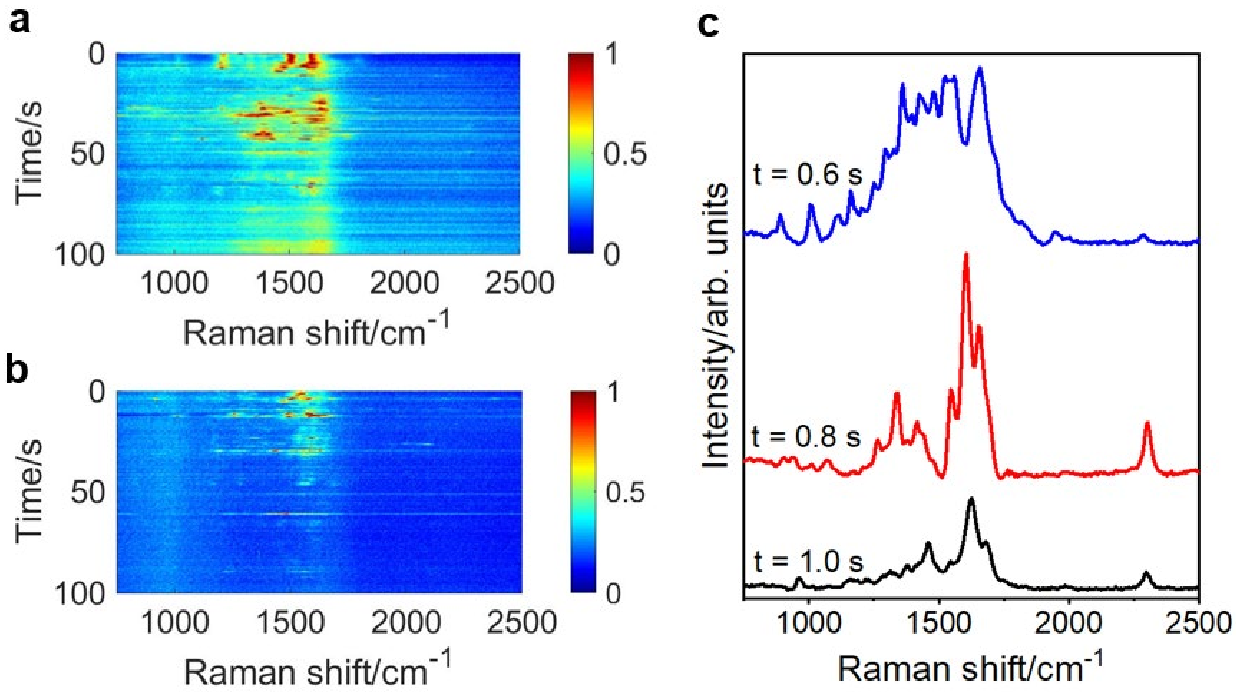

Figure 2.14. Two representative examples (a and b) of spectrograms showing the time series of in-situ SERS spectra (normalized to a [0, 1] scale at each time-point) acquired from an individual Ag NP scatterer in CO_2-saturated water under plasmonic excitation. The SERS intensity is coded by the color, as indicated by the legend. c) SERS spectra presented in Fig. 2.1d are plotted here without normalization to demonstrate the intensity variations from one time-frame to another. The spectra were baseline-subtracted prior to plotting in a vertically-stacked manner. The baseline was determined by polynomial fitting.

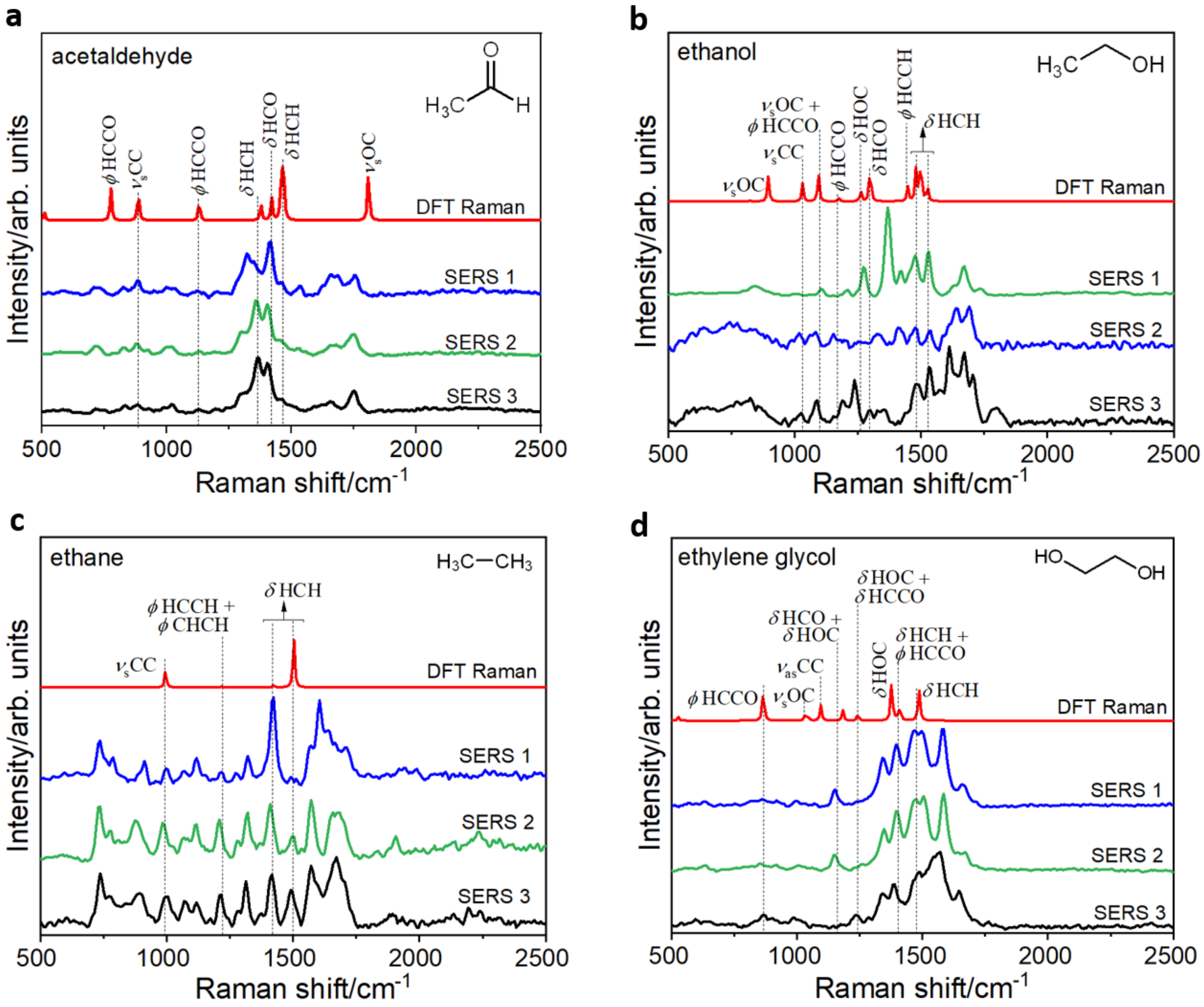

Figure 2.15. Three representative examples of measured SERS spectra (blue, green, and black traces) that correspond to the detection of a) acetaldehyde, b) ethanol, c) ethane, and d) ethylene glycol. In each case, the DFT-computed Raman vibrational spectrum, which served as the basis of the assignment of the measured SERS spectra, is also shown by the red trace. The major vibrational modes are labeled using the following symbols: ϕ-torsion; ν_s-symmetric stretching; ν_{as}-asymmetric stretching; δ-bending. Spectra are shown vertically stacked for clarity. SERS spectra were baseline-subtracted, subjected to smoothing by the Savitzky–Golay method with a window of 5 points and a polynomial of order 3, and normalized to a [0, 1] scale prior to plotting. The baseline was determined by polynomial fitting. DFT-computed Raman spectra were normalized to a [0, 1] scale, and the y-axis quantity was magnified (by a scale factor of 10 in panel a, a factor of 5 in panels b and d and a factor of 3 in panel c) prior to plotting.

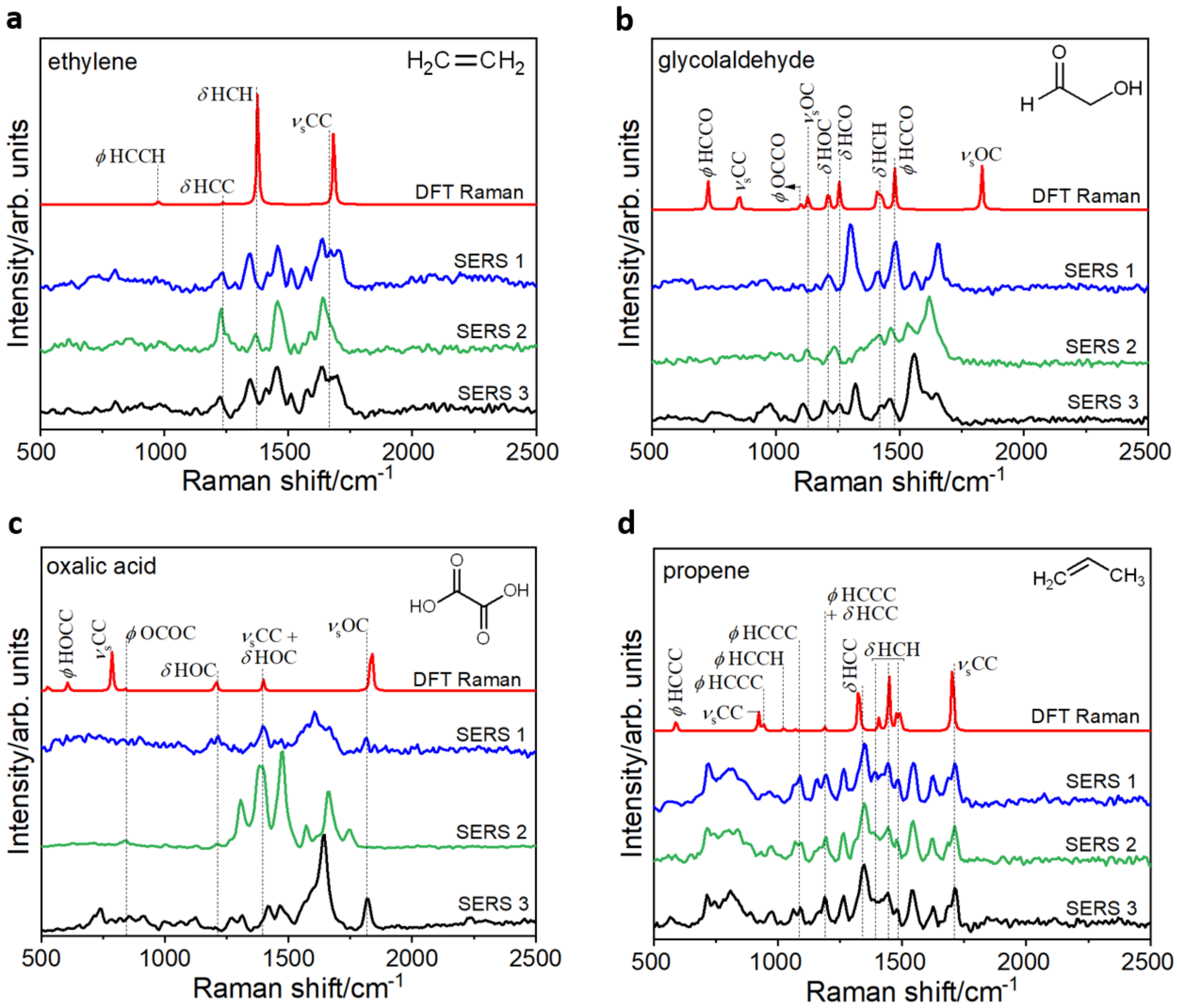

Figure 2.16. Three representative examples of measured SERS spectra (blue, green, and black traces) that correspond to the detection of a) ethylene, b) glycolaldehyde, c) oxalic acid, and d) propene. In each case, the DFT-computed Raman vibrational spectrum, which served as the basis of the assignment of the measured SERS spectra, is also shown by the red trace. The major vibrational modes are labeled using the following symbols: ϕ-torsion; ν_s-symmetric stretching; ν_{as}-asymmetric stretching; δ-bending. Spectra are shown vertically stacked for clarity. SERS spectra were baseline-subtracted, subjected to smoothing by the Savitzky–Golay method with a window of 5 points and a polynomial of order 3, and normalized to a [0, 1] scale prior to plotting. The baseline was determined by polynomial fitting. DFT-computed Raman spectra were normalized to a [0, 1] scale, and the y-axis quantity was magnified (by a scale factor of 5 in panels a and b, a factor of 2 in panel c and a factor of 3 in panel d) prior to plotting.

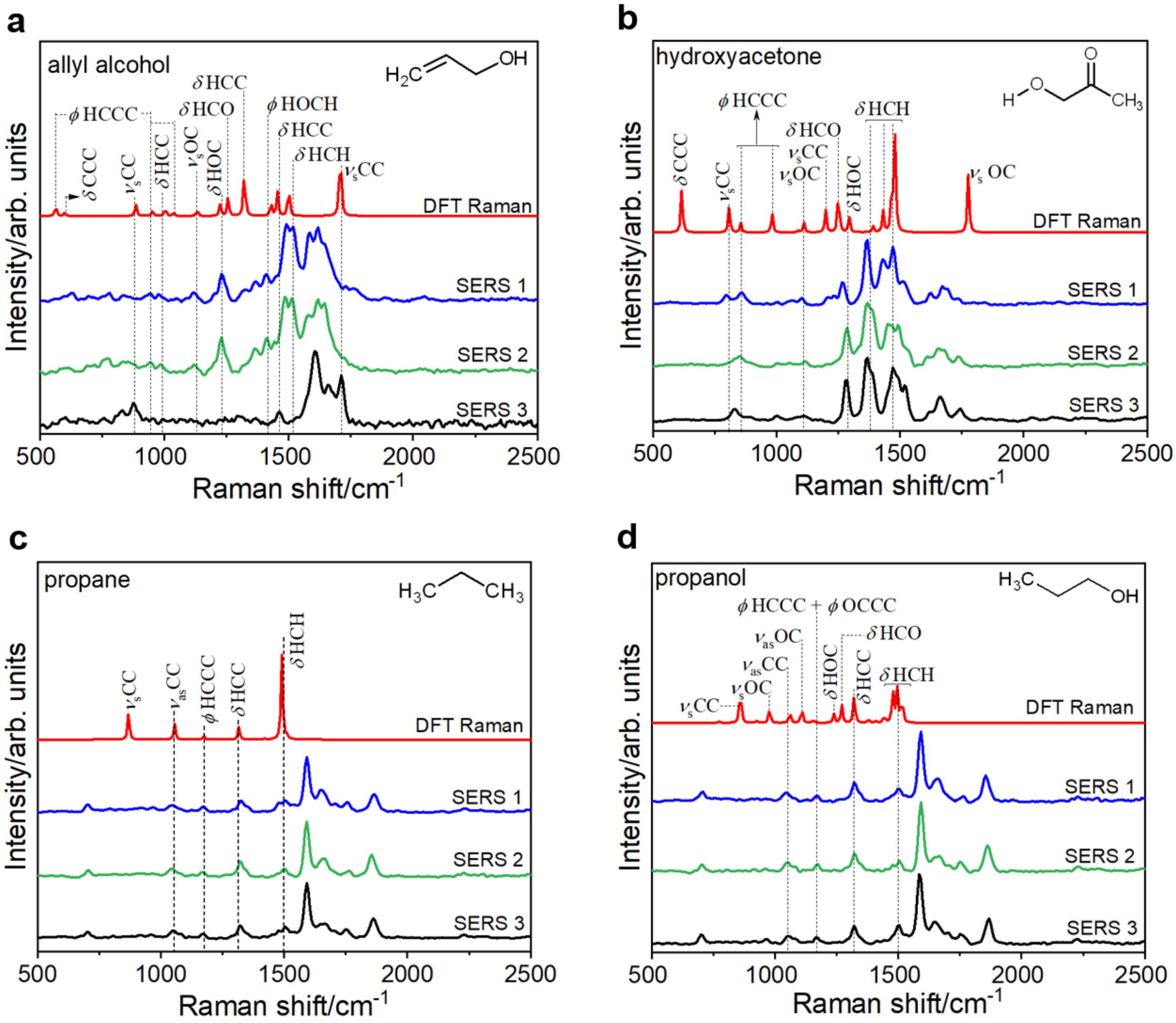

Figure 2.17. Three representative examples of measured SERS spectra (blue, green, and black traces) that correspond to the detection of a) allyl alcohol, b) hydroxyacetone, c) propane, and d) propanol. In each case, the DFT-computed Raman vibrational spectrum, which served as the basis of the assignment of the measured SERS spectra, is also shown by the red trace. The major vibrational modes are labeled using the following symbols: ϕ-torsion; ν_s-symmetric stretching; ν_{as}-asymmetric stretching; δ-bending. Spectra are shown vertically stacked for clarity. SERS spectra were baseline-subtracted, subjected to smoothing by the Savitzky–Golay method with a window of 5 points and a polynomial of order 3, and normalized to a [0, 1] scale prior to plotting. The baseline was determined by polynomial fitting. DFT-computed Raman spectra were normalized to a [0, 1] scale, and the y-axis quantity was magnified (by a scale factor of 3 in panel a and a factor of 10 in panels b, c and d) prior to plotting.

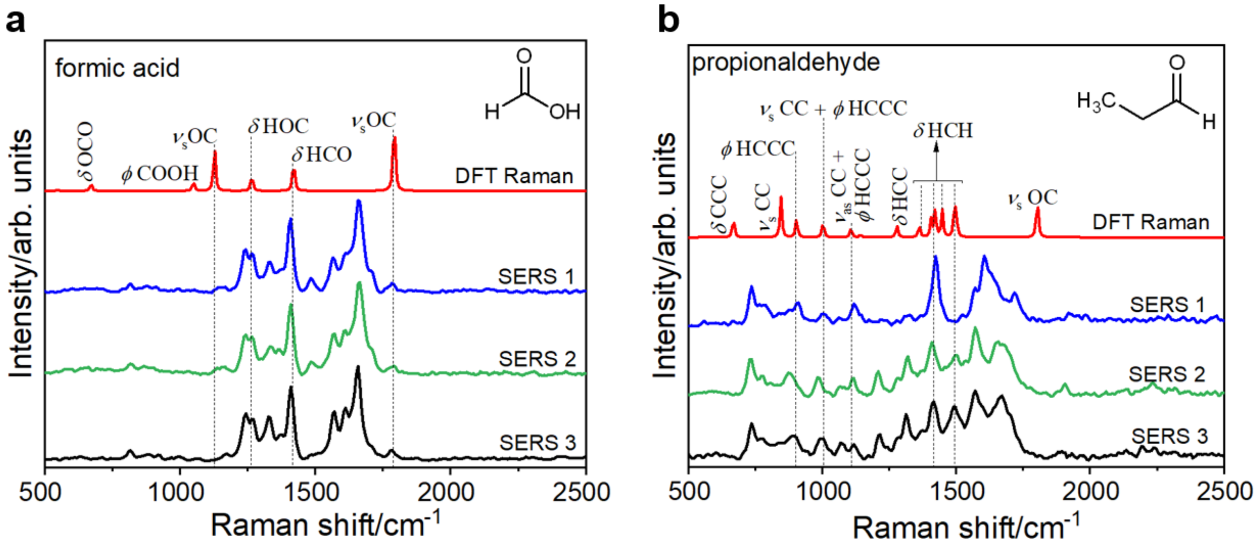

Figure 2.18. Three representative examples of measured SERS spectra (blue, green, and black traces) that correspond to the detection of a) formic acid and b) propionaldehyde. In each case, the DFT-computed Raman vibrational spectrum, which served as the basis of the assignment of the measured SERS spectra, is also shown by the red trace. The major vibrational modes are labeled using the following symbols: ϕ-torsion; ν_s-symmetric stretching; ν_{as}-asymmetric stretching; δ-bending. Spectra are shown vertically stacked for clarity. SERS spectra were baseline-subtracted, subjected to smoothing by the Savitzky–Golay method with a window of 5 points and a polynomial of order 3, and normalized to a [0, 1] scale prior to plotting. The baseline was determined by polynomial fitting. DFT-computed Raman spectra were normalized to a [0, 1] scale, and the y-axis quantity was magnified (by a scale factor of 4 in panel a and a factor of 5 in panel b) prior to plotting.

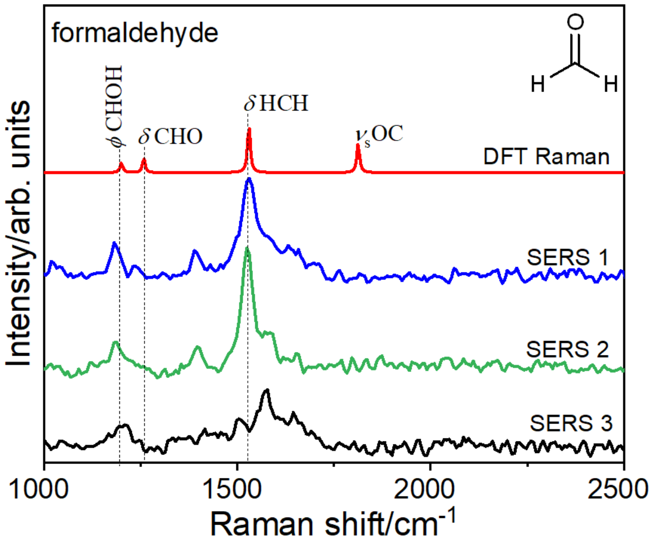

Figure 2.19. Three representative examples of measured SERS spectra (blue, green, and black traces) that correspond to the detection of formaldehyde. The DFT-computed Raman vibrational spectrum, which served as the basis of the assignment of the measured SERS spectra, is also shown by the red trace. The major vibrational modes are labeled using the following symbols: ϕ-torsion; ν_s-symmetric stretching; ν_{as}-asymmetric stretching; δ-bending. Spectra are shown vertically stacked for clarity. SERS spectra were baseline-subtracted, subjected to smoothing by the Savitzky–Golay method with a window of 5 points and a polynomial of order 3, and normalized to a [0, 1] scale prior to plotting. The baseline was determined by polynomial fitting. The DFT-computed Raman spectrum was normalized to a [0, 1] scale, and the y-axis quantity was magnified by a scale factor of 3 prior to plotting.

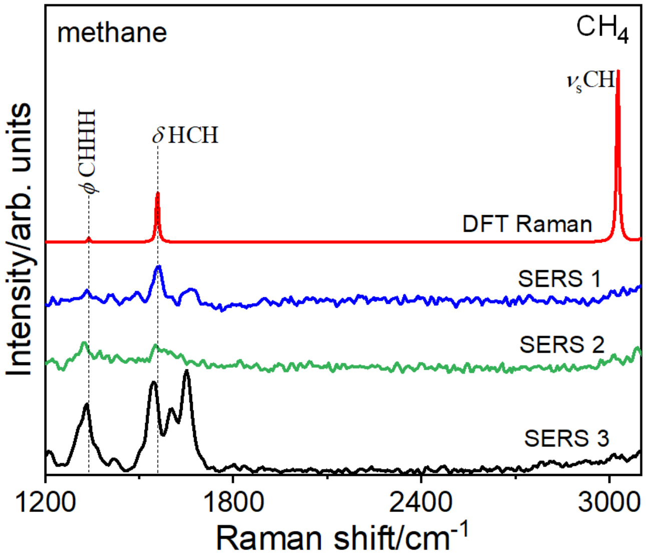

Figure 2.20. Three representative examples of measured SERS spectra (blue, green, and black traces) that correspond to the detection of methane. The DFT-computed Raman vibrational spectrum, which served as the basis of the assignment of the measured SERS spectra, is also shown by the red trace. The major vibrational modes are labeled using the following symbols: ϕ-torsion; ν_s-symmetric stretching; ν_{as}-asymmetric stretching; δ-bending. Spectra are shown vertically stacked for clarity. SERS spectra were baseline-subtracted, subjected to smoothing by the Savitzsky–Golay method with a window of 5 points and a polynomial of order 3, and normalized to a [0, 1] scale prior to plotting. The baseline was determined by polynomial fitting. The DFT-computed Raman spectrum was normalized to a [0, 1] scale, and the y-axis quantity was magnified by a scale factor of 2 prior to plotting.

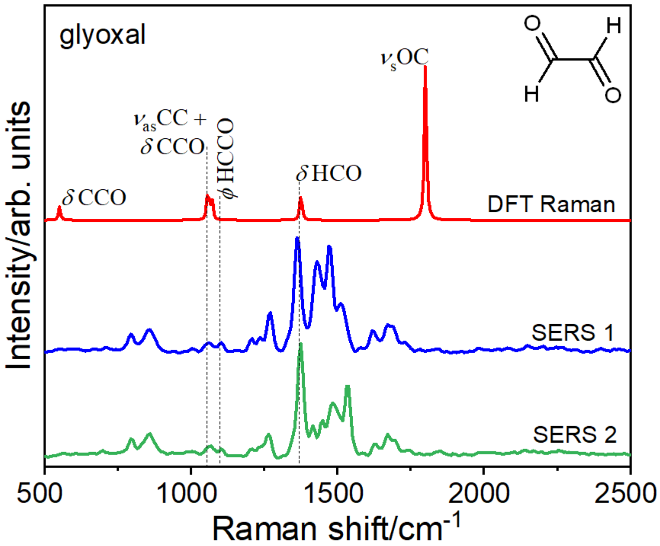

Figure 2.21. Two representative examples of measured SERS spectra (blue and green traces) that correspond to the detection of glyoxal. The DFT-computed Raman vibrational spectrum, which served as the basis of the assignment of the measured SERS spectra, is also shown by the red trace. The major vibrational modes are labeled using the following symbols: ϕ-torsion; ν_s-symmetric stretching; ν_{as}-asymmetric stretching; δ-bending. Spectra are shown vertically stacked for clarity. SERS spectra were baseline-subtracted, subjected to smoothing by the Savitzsky–Golay method with a window of 5 points and a polynomial of order 3, and normalized to a [0, 1] scale prior to plotting. The baseline was determined by polynomial fitting. The DFT-computed Raman spectrum was normalized to a [0, 1] scale, and the y-axis quantity was magnified by a scale factor of 3 prior to plotting.

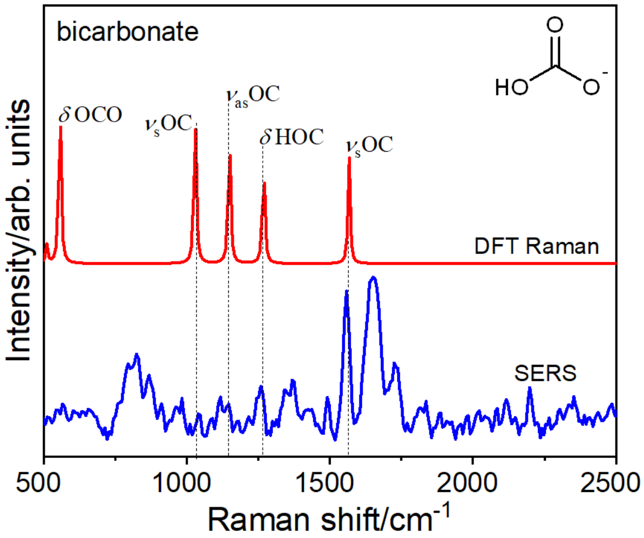

Figure 2.22. One example of a measured SERS spectrum (blue trace) that corresponds to the detection of bicarbonate. The DFT-computed Raman vibrational spectrum, which served as the basis of the assignment of the measured SERS spectrum, is also shown by the red trace. The major vibrational modes are labeled using the following symbols: ϕ-torsion; ν_s-symmetric stretching; ν_{as}-asymmetric stretching; δ-bending. Spectra are shown vertically stacked for clarity. SERS spectrum was baseline-subtracted, subjected to smoothing by the Savitzky–Golay method with a window of 5 points and a polynomial of order 3, and normalized to a [0, 1] scale and the y-axis quantity was magnified by a scale factor of 2 prior to plotting. The baseline was determined by polynomial fitting. The DFT-computed Raman spectrum was normalized to a [0, 1] scale prior to plotting.

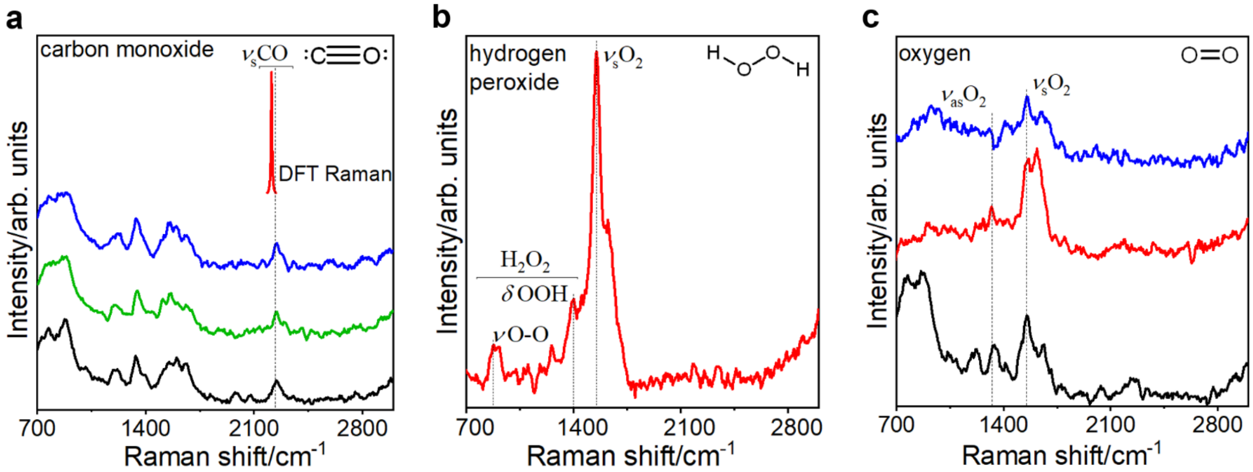

Figure 2.23. a) Three representative examples of measured SERS spectra (blue, green, and black traces) that correspond to the detection of carbon monoxide. The DFT-computed Raman vibrational spectrum for carbon monoxide, which has a single mode, is also shown by the red trace. Although the ν_s mode of carbon monoxide is predicted by DFT to have a frequency of 2200 cm^{-1}, in practice, the mode can appear in the 1800–2200 cm^{-1} range depending on the adsorption motif of carbon monoxide. SERS spectra were subjected to smoothing by the Savitzky–Golay method with a window of 5 points and a polynomial of order 1, and normalized to a [0, 1] scale and the y-axis quantity was magnified by a scale factor of 2 prior to plotting in a vertically stacked manner. The DFT-computed Raman spectrum was normalized to a [0, 1] scale prior to plotting. b) One representative example of a measured SERS spectrum (red trace) that is assigned to hydrogen peroxide.[169] The SERS spectrum was baseline-subtracted, and subjected to smoothing by the Savitzky–Golay method with a window of 5 points and a polynomial of order 1 prior to plotting. The baseline was determined by polynomial fitting. c) Three representative examples of measured SERS spectra (blue, red, and black traces) that are assigned to oxygen.[170, 171] SERS spectra were normalized to a [0, 1] scale and subjected to smoothing by the Savitzky–Golay method with a window of 5 points and a polynomial of order 1 prior to plotting in a vertically-stacked manner. SERS bands from vibrational modes are labeled using the following symbols: ϕ-torsion; ν-stretching; ν_s-symmetric stretching; ν_{as}-asymmetric stretching; δ-bending.

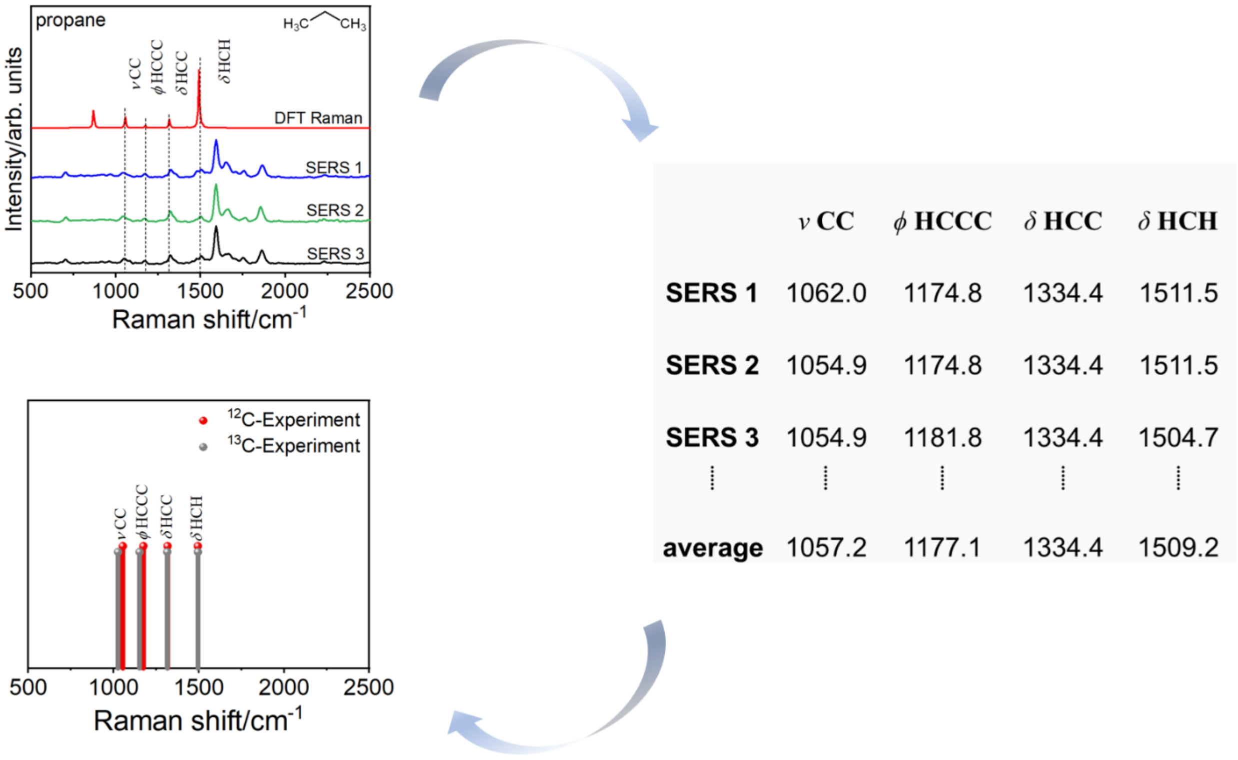

	ν CC	*ϕ* HCCC	*δ* HCC	*δ* HCH
SERS 1	1062.0	1174.8	1334.4	1511.5
SERS 2	1054.9	1174.8	1334.4	1511.5
SERS 3	1054.9	1181.8	1334.4	1504.7
⋮	⋮	⋮	⋮	⋮
average	1057.2	1177.1	1334.4	1509.2

Figure 2.24. Depiction of the method of construction of a spectral barcode from experimental SERS spectra. The example shown here corresponds to the ^{12}C isotopolog of propane. In the top left panel, reproduced from Fig. 2.17c, three representative examples of experimental SERS spectra (blue, green, and black traces) are shown plotted along with the DFT-computed Raman vibrational spectrum (red trace), which served as the basis of the assignment of the measured SERS spectra to propane. The major vibration modes are labeled using the following symbols: *ϕ*-torsion; *v*- stretching; *δ*-bending. Spectra are shown vertically stacked for clarity. SERS spectra were baseline-subtracted, subjected to smoothing by the Savitzsky–Golay method with a window of 5 points and a polynomial of order 3, and normalized to a [0, 1] scale prior to plotting. The baseline was determined by polynomial fitting. The DFT-computed Raman spectrum was normalized to a [0, 1] scale, and the y-axis quantity was magnified by a scale factor of 10 prior to plotting. From each experimental SERS spectrum corresponding to a given species, peak wavenumbers (cm^{-1}) of all key modes were determined, as shown by the table on the right. For each mode, the average of the peak wavenumber across all experimental spectra was obtained. A barcode, shown in the lower left panel, was then constructed by plotting vertical sticks corresponding to the locations of the averaged peak wave-numbers for all modes of the species. While only the process used for construction of the ^{12}C isotopolog barcode (red lines) is shown here, similar steps were employed to construct the barcode for the ^{13}C isotopolog (gray lines).

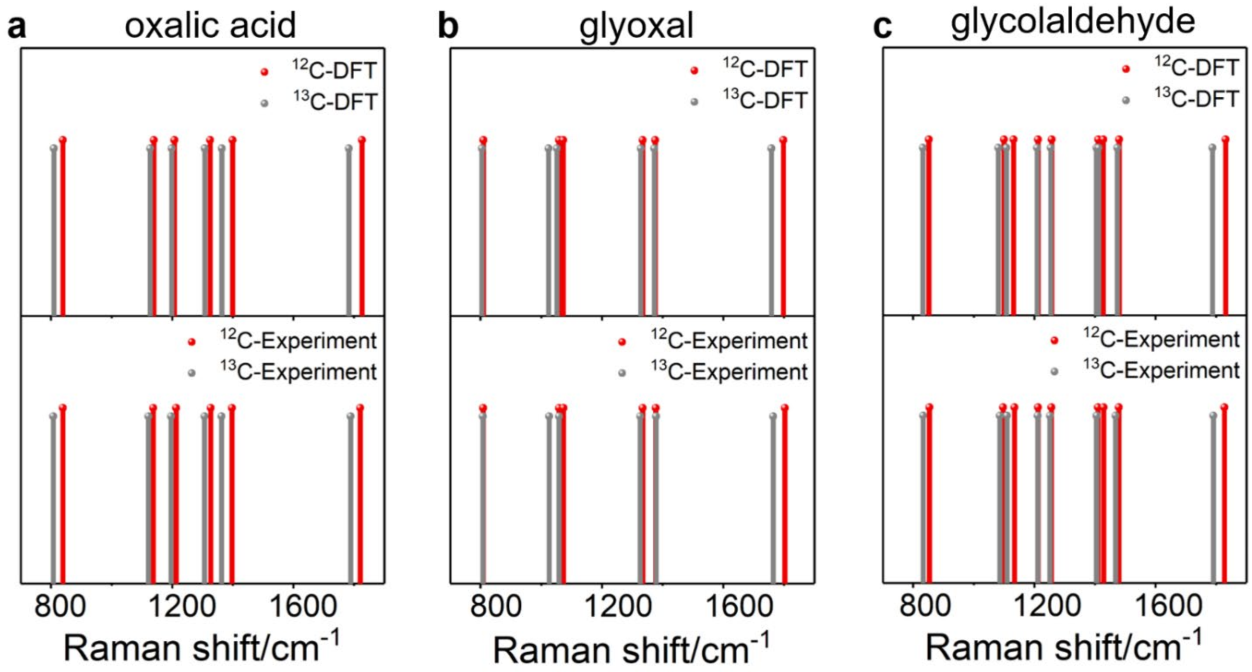

Figure 2.25. Isotopological validation of CO_2RR origin of surface species. Spectral barcodes for the DFT-computed Raman spectra (top row) and experimental SERS spectra (bottom row) for ^{12}C (red lines) and ^{13}C (gray lines) isotopologs of a) oxalic acid, b) glyoxal, and c) glycolaldehyde. Each vertical line in a barcode indicates the peak wavenumber of a vibrational mode. The number of SERS spectra that led to the experimental barcodes are a) 97 and 25, b) 17 and 27, and c) 229 and 231 for the ^{12}C and ^{13}C isotopologs, respectively.

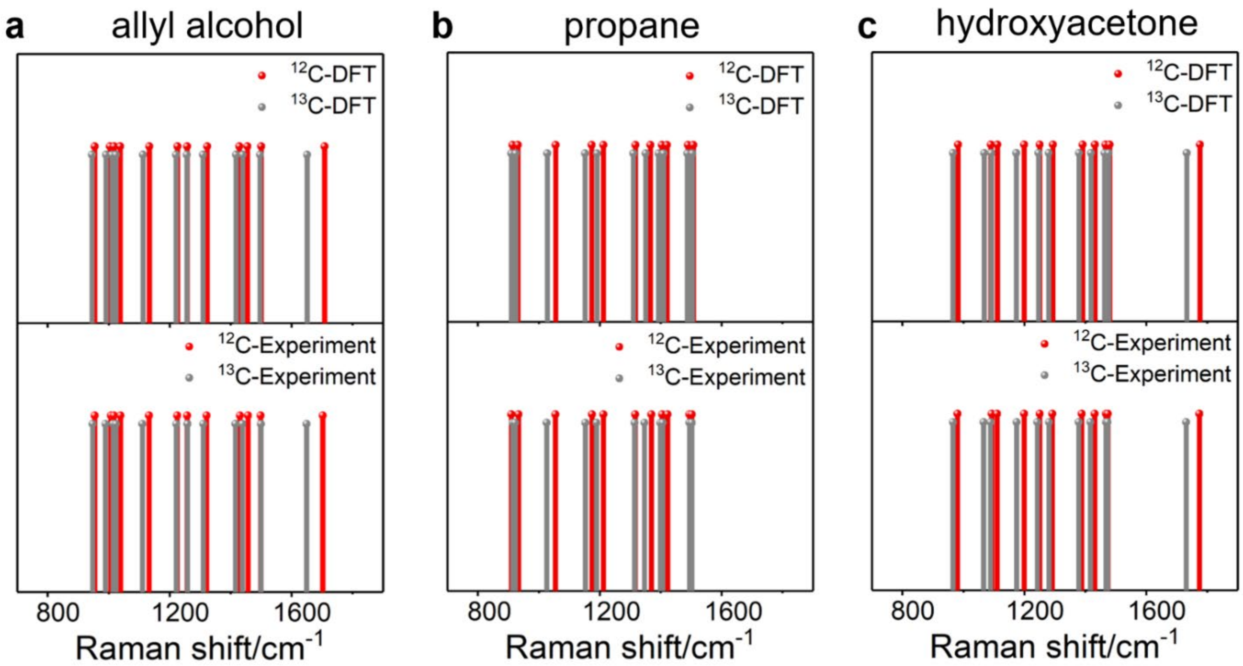

Figure 2.26. Isotopological validation of CO_2RR origin of surface species. Spectral barcodes for the DFT-computed Raman spectra (top row) and experimental SERS spectra (bottom row) for ^{12}C (red lines) and ^{13}C (gray lines) isotopologs of a) allyl alcohol, b) propane, and c) hydroxyacetone. Each vertical line in a barcode indicates the peak wavenumber of a vibrational mode. The number of SERS spectra that led to the experimental barcodes are a) 352 and 516, b) 354 and 569, and c) 372 and 157 for the ^{12}C and ^{13}C isotopologs, respectively.

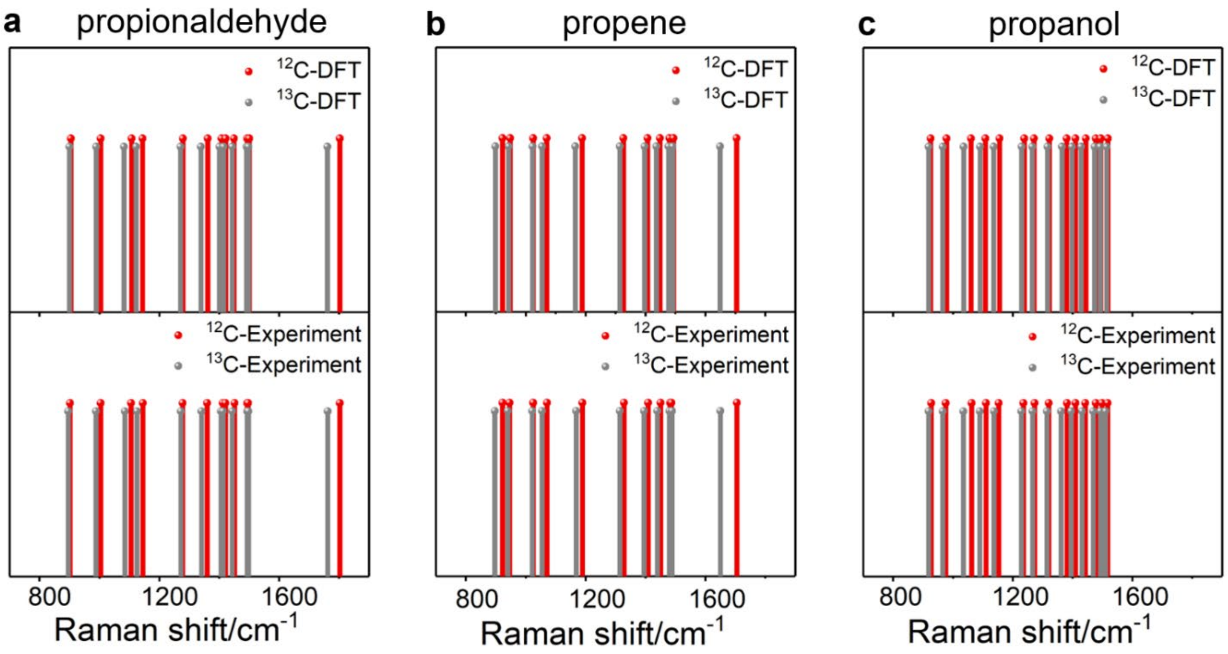

Figure 2.27. Isotopological validation of CO_2RR origin of surface species. Spectral barcodes for the DFT-computed Raman spectra (top row) and experimental SERS spectra (bottom row) for ^{12}C (red lines) and ^{13}C (gray lines) isotopologs of a) propionaldehyde, b) propene, and c) propanol. Each vertical line in a barcode indicates the peak wavenumber of a vibrational mode. The number of SERS spectra that led to the experimental barcodes are a) 598 and 312, b) 316 and 513, and c) 666 and 684 for the ^{12}C and ^{13}C isotopologs, respectively.

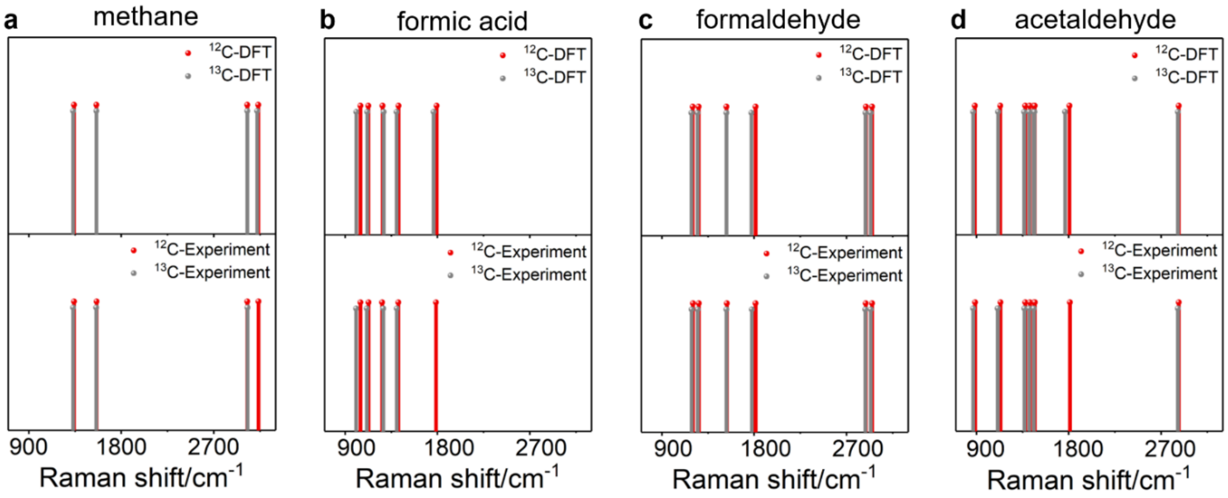

Figure 2.28. Isotopological validation of CO_2RR origin of surface species. Spectral barcodes for the DFT-computed Raman spectra (top row) and experimental SERS spectra (bottom row) for ^{12}C (red lines) and ^{13}C (gray lines) isotopologs of a) methane, b) formic acid, c) formaldehyde and d) acetaldehyde. Each vertical line in a barcode indicates the peak wavenumber of a vibrational mode. The number of SERS spectra that led to the experimental barcodes are a) 6 and 3, b) 10 and 3, c) 28 and 15, and d) 100 and 316 for the ^{12}C and ^{13}C isotopologs, respectively.

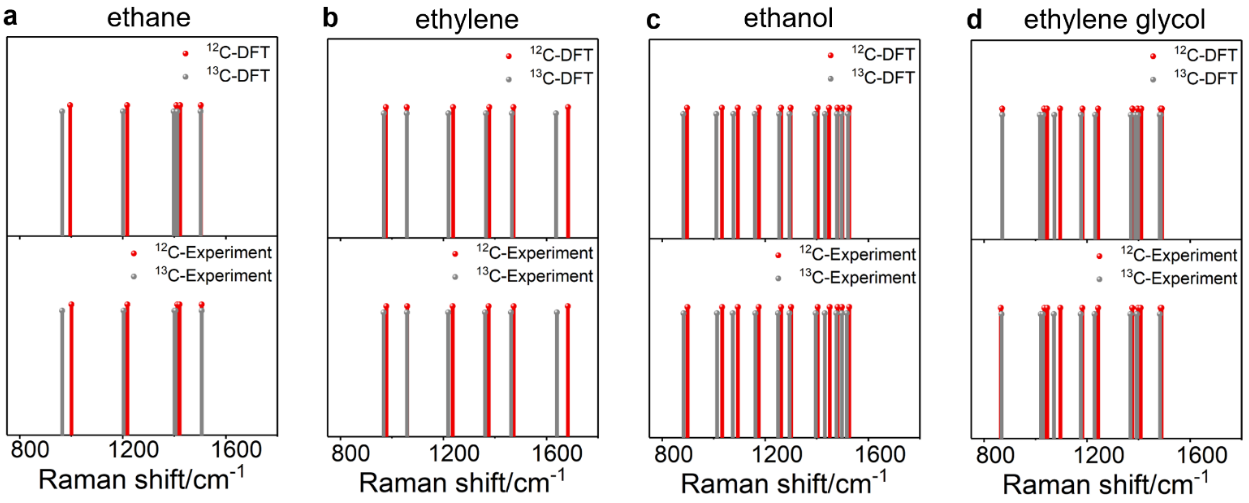

Figure 2.29. Isotopological validation of CO$_2$RR origin of surface species. Spectral barcodes for the DFT-computed Raman spectra (top row) and experimental SERS spectra (bottom row) for ^{12}C (red lines) and ^{13}C (gray lines) isotopologs of a) ethane, b) ethylene, c) ethanol and d) ethylene glycol. Each vertical line in a barcode indicates the peak wavenumber of a vibrational mode. The number of SERS spectra that led to the experimental barcodes are a) 341 and 81, b) 49 and 146, c) 177 and 162, and d) 873 and 344 for the ^{12}C and ^{13}C isotopologs, respectively.

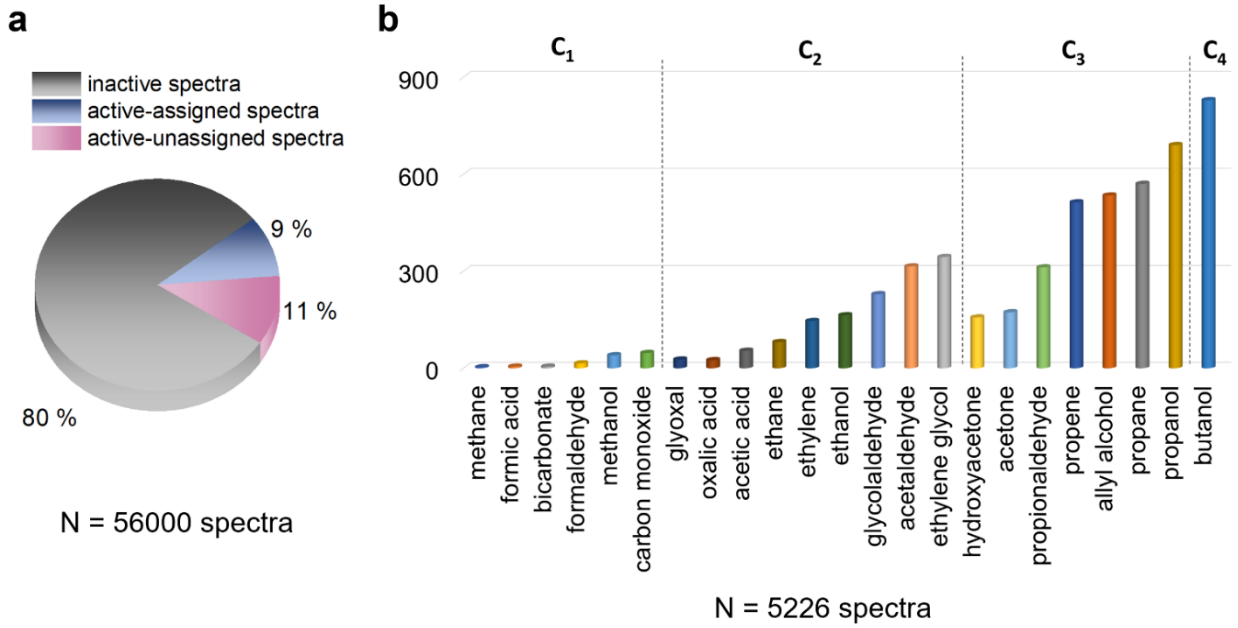

Figure 2.30. a) Pie-chart showing the % distribution of inactive SERS spectra, active spectra that were assigned to a species in the database, and active spectra that were unassignable. This distribution was obtained by an analysis of 56,000 in-situ SERS spectra collected from 56 individual Ag NP scatterers in $^{13}CO_2$-saturated water under plasmonic excitation. d) Bar plot showing for each surface species the number of detection events across the set of active, assigned spectra. The species are grouped into C_1, C_2, C_3, and C_4 categories; within each category, they are listed in the order of their prevalence. N in panels a and b represents the total number of spectra that led to the plot.

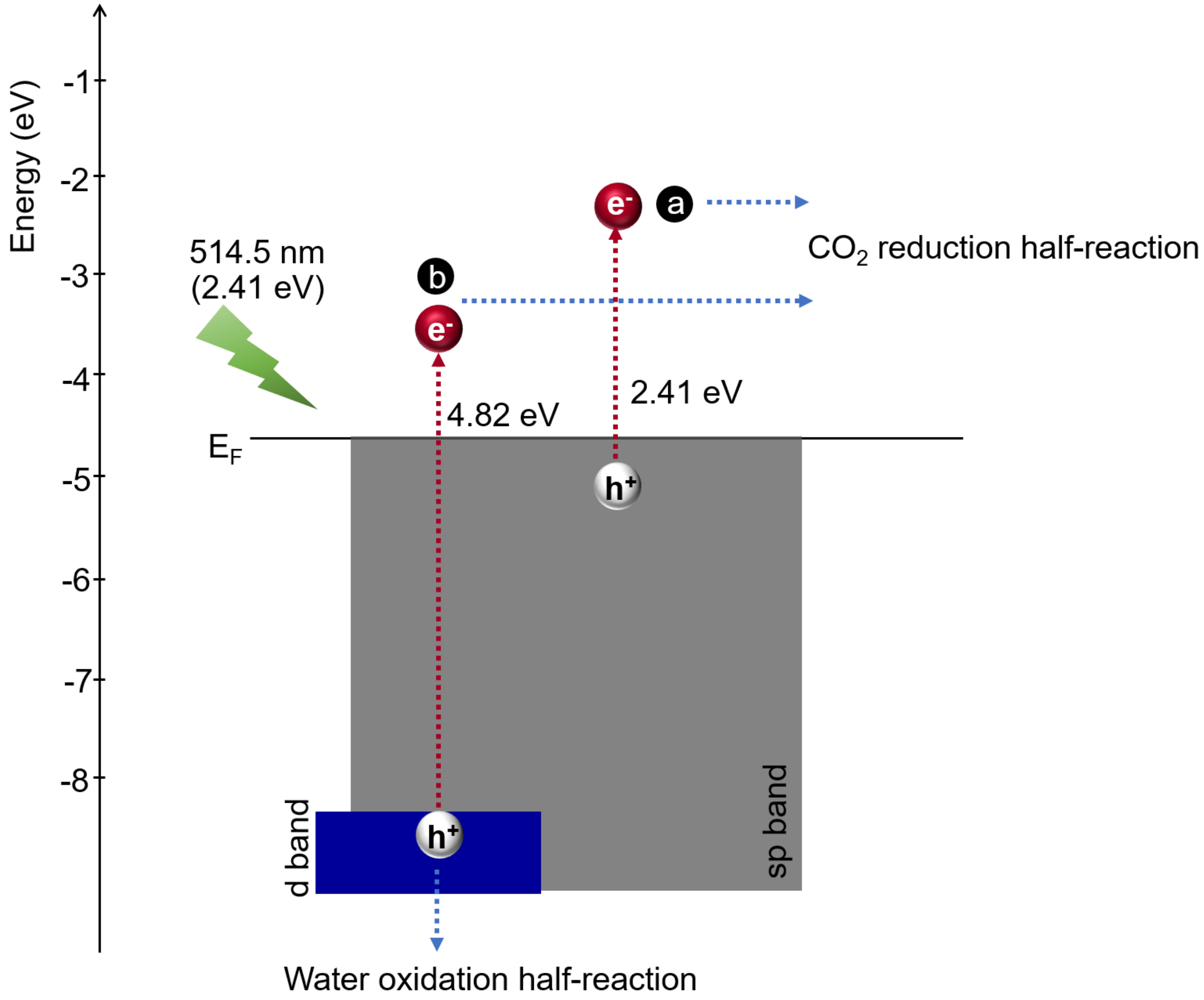

Figure 2.31. Energy diagram depicting possible carrier excitations in an Ag NP dimer, initiated by 514.5 nm laser excitation (2.41 eV). In a typical scenario (depicted as “a”), an LSPR excited in a Ag NP by visible light would undergo decay via an intraband transition to form an electron–hole pair in the sp band of Ag. The resulting electron is considerably energetic relative to the Fermi level (E_F) of Ag, but the hole is not sufficiently energetic for water oxidation, which has a standard reduction potential of 1.23 V vs the standard hydrogen electrode at a pH of 0, i.e., –5.67 V relative to vacuum.[85] Interband transitions cannot be excited in Ag by 514.5 nm laser excitation. Due to the ~4 eV interband edge of Ag,[172] UV light excitation is required. However, the focused laser excitation conditions we employ (Table 2.46) can favor multiphoton excitation and carrier re-excitation processes, which would result in the generation of highly energetic electron–hole pairs akin to those generated by UV light. For instance, two-photon absorption or energetic combination of two sp-band electron–hole pairs of 2.41 eV energy each can induce an interband transition (depicted as “b”) generating a hole in the d band. Such a hole would be energetic enough for the water oxidation half-reaction. Energies are shown relative to the vacuum level.

2.7. TABLES

Table 2.1. Database of chemical species used for assignment of SERS spectra

Category	**Chemical species**
C_1	carbon monoxide
	bicarbonate
	methane
	formic acid
	formaldehyde
	methanol
C_2	glyoxal
	ethylene
	oxalic acid
	acetaldehyde
	acetic acid
	ethanol
	glycolaldehyde
	ethane
	ethylene glycol
C_3	acetone
	propene
	allyl alcohol
	propane
	hydroxyacetone
	propionaldehyde
	propanol
C_4	butanol

Table 2.2. DFT-computed Raman frequencies and normal mode analysis for formaldehyde

formaldehyde		
^{12}C υ in cm^{-1}	Major vibrational component (PED %)	^{13}C υ in cm^{-1}
1201	ϕ_{out} CHOH (100)	1189
1259	δ HCO (100)	1249
1530	δ HCH (90)	1530
1813	v OC (90)	1773
2889	v CH (100)	2885
2948	v CH (100)	2935

Table 2.3. DFT-computed Raman frequencies and normal mode analysis for formic acid

formic acid		
^{12}C υ in cm^{-1}	Major vibrational component (PED %)	^{13}C υ in cm^{-1}
1050	ϕ_{out} COOH (-100)	1009
1128	v OC (78)	1116
1266	δ HOC (76)	1276
1421	δ HCO (92)	1402
1792	v OC (87)	1763

Table 2.4. DFT-computed Raman frequencies and normal mode analysis for bicarbonate

bicarbonate		
^{12}C υ in cm^{-1}	Major vibrational component (PED %)	^{13}C υ in cm^{-1}
557	δ OCO (87)	555
1030	v OC (88)	1027
1149	v OC (-59)	1136
1269	δ HOC (64)	1252
1567	v OC (93)	1527

Table 2.5. DFT-computed Raman frequencies and normal mode analysis for methane

methane		
^{12}C υ in cm^{-1}	Major vibrational component (PED %)	^{13}C υ in cm^{-1}
1340	δ HCH (70); ϕ_{out} CHHH (-93); ϕ_{out} CHHH (-69)	1331
1558	δ HCH (98); δ HCH (98)	1558
3026	v CH (100)	3026
3132	v CH (91); v CH (91); v CH (85)	3121

Table 2.6. DFT-computed Raman frequencies and normal mode analysis for methanol

methanol		
^{12}C υ in cm^{-1}	Major vibrational component (PED %)	^{13}C υ in cm^{-1}
1040	ν OC (71)	1024
1070	ϕ_{out} CHOH (37); δ HOC (-30)	1064
1168	ϕ_{out} CHOH (-85)	1160
1357	δ HOC (58)	1349
1479	δ HCH (92)	1473
1494	δ HCH (85)	1492
1505	δ HCH (-82)	1503

Table 2.7. DFT-computed Raman frequencies and normal mode analysis for carbon monoxide

carbon monoxide		
^{12}C υ in cm^{-1}	Major vibrational component (PED %)	^{13}C υ in cm^{-1}
2213	ν OC	2163

Table 2.8. DFT-computed Raman frequencies and normal mode analysis for ethane

ethane		
^{12}C υ in cm^{-1}	Major vibrational component (PED %)	^{13}C υ in cm^{-1}
996	ν CC (98)	965
1217	ϕ HCCH (-71); ϕ_{out} CHCH (-43)	1201
1408	δ HCH (-81)	1398
1423	δ HCH (86)	1412
1503	δ HCH (76); δ HCH (69)	1502
1506	δ HCH (-54); δ HCH (77)	1503

Table 2.9. DFT-computed Raman frequencies and normal mode analysis for ethanol

ethanol		
^{12}C υ in cm^{-1}	Major vibrational component (PED %)	^{13}C υ in cm^{-1}
897	v OC (56)	882
1032	v CC (65)	1010
1094	v OC (30); ϕ HCCO (27)	1077
1176	ϕ HCCO (-76)	1160
1262	δ HOC (58)	1254
1299	δ HCO (81)	1295
1404	δ HCH (77)	1394
1448	ϕ HCCH (-46)	1432
1481	δ HCH (72)	1479
1500	δ HCH (67)	1497
1526	δ HCH (-57)	1521

Table 2.10. DFT-computed Raman frequencies and normal mode analysis for ethylene

ethylene		
^{12}C υ in cm^{-1}	Major vibrational component (PED %)	^{13}C υ in cm^{-1}
977	ϕ HCCH (77)	969
1058	ϕ HCCH (100)	1058
1238	δ HCC (-100)	1220
1378	δ HCH (65)	1365
1472	δ HCH (100)	1466
1684	v CC (65)	1637

Table 2.11. DFT-computed Raman frequencies and normal mode analysis for ethylene glycol

ethylene glycol		
^{12}C υ in cm^{-1}	Major vibrational component (PED %)	^{13}C υ in cm^{-1}
871	ϕ HCCO (63)	871
1034	v OC (63)	1017
1045	δ HOC (27); ϕ HCCO (19)	1030
1096	v CC (-70)	1073
1183	δ HOC (37); δ HCO (37)	1177
1243	δ HOC (-28); δ HCCO (-20)	1232
1376	δ HOC (44)	1370
1378	δ HOC (-42)	1374
1396	ϕ HCCO (54)	1387
1411	δ HCH (74)	1398
1486	δ HCH (71)	1482
1491	δ HCH (-77)	1487

Table 2.12. DFT-computed Raman frequencies and normal mode analysis for acetic acid

acetic acid		
^{12}C υ in cm^{-1}	Major vibrational component (PED %)	^{13}C υ in cm^{-1}
999	ϕ HCCO (49)	989
1067	ϕ HCCO (-58)	1048
1205	v CC (-27); δ HOC (28)	1190
1332	δ HOC (-52)	1313
1408	δ HCH (42)	1392
1472	δ HCH (41)	1470
1476	δ HCH (75)	1474
1818	v OC (83)	1773

Table 2.13. DFT-computed Raman frequencies and normal mode analysis for acetaldehyde

acetaldehyde		
^{12}C υ in cm^{-1}	Major vibrational component (PED %)	^{13}C υ in cm^{-1}
886	ν_{s} CC (63)	868
1128	ϕ HCCO (-40); ν_{as} CC (-23)	1104
1133	ϕ HCCO (76)	1113
1377	δ HCH (88)	1366
1420	δ HCO (85)	1415
1460	δ HCH (-71)	1458
1469	δ HCH (-76)	1467
1808	ν_{s} OC (90)	1765
2871	ν_{s} CH (99)	2863

Table 2.14. DFT-computed Raman frequencies and normal mode analysis for oxalic acid

oxalic acid		
^{12}C υ in cm^{-1}	Major vibrational component (PED %)	^{13}C υ in cm^{-1}
839	ϕ_{out} OCOC (98)	810
1139	ν OC (69)	1127
1207	δ HOC (58)	1198
1325	δ HOC (63)	1308
1399	ν CC (47); δ HOC (27)	1364
1826	ν OC (93)	1783
1836	ν OC (85)	1789

Table 2.15. DFT-computed Raman frequencies and normal mode analysis for glycolaldehyde

glycolaldehyde		
^{12}C υ in cm^{-1}	Major vibrational component (PED %)	^{13}C υ in cm^{-1}
852	ν CC (74)	832
1100	ϕ OCCO (-69)	1081
1131	ν OC (73)	1108
1212	δ HOC (73)	1209
1257	δ HCO (75)	1254
1411	δ HCH (-80)	1405
1428	δ HCH (69)	1412
1480	ϕ HCCO (73)	1474
1831	ν OC (91)	1788

Table 2.16. DFT-computed Raman frequencies and normal mode analysis for glyoxal

glyoxal		
^{12}C υ in cm^{-1}	Major vibrational component (PED %)	^{13}C υ in cm^{-1}
810	ϕ HCCO (77)	805
1059	ν CC (-49); δ CCO (46)	1024
1072	ϕ HCCO (100)	1052
1334	δ HCO (98)	1328
1376	δ HCO (88)	1373
1798	ν OC (99)	1758
1801	ν OC (88)	1760

Table 2.17. DFT-computed Raman frequencies and normal mode analysis for propane

propane		
^{12}C υ in cm^{-1}	Major vibrational component (PED %)	^{13}C υ in cm^{-1}
870	ν CC (85)	846
914	ϕ HCCC (57)	910
932	ϕ HCCC (67)	925
1056	ν CC (-87)	1028
1174	ϕ HCCC (55)	1152
1212	ϕ HCCC (-75)	1191
1317	δ HCC (55)	1311
1367	ϕ HCCH (-76)	1351
1404	δ HCH (79)	1393
1421	δ HCH (81)	1410
1490	δ HCH (-57)	1488
1492	δ HCH (-79)	1490
1497	δ HCH (57)	1495
1507	δ HCH (75)	1505
1513	δ HCH (80)	1509

Table 2.18. DFT-computed Raman frequencies and normal mode analysis for propanol

propanol		
^{12}C υ in cm^{-1}	Major vibrational component (PED %)	^{13}C υ in cm^{-1}
860	v CC (76)	838
926	ϕ HCCC (57)	919
979	v OC (47)	966
1061	v CC (-64)	1036
1109	v OC (-31); ϕ HCCC (17)	1091
1156	ϕ HCCC (-37); ϕ OCCC (16)	1136
1239	δ HOC (47)	1230
1271	δ HCO (56)	1265
1322	δ HCC (42)	1316
1380	ϕ HCCO (-54)	1365
1410	δ HCH (79)	1398
1444	ϕ HCCC (50)	1429
1478	δ HCH (84)	1474
1495	δ HCH (-65)	1493
1509	δ HCH (-64)	1506
1518	δ HCH (67)	1514

Table 2.19. DFT-computed Raman frequencies and normal mode analysis for propene

propene		
^{12}C υ in cm^{-1}	Major vibrational component (PED %)	^{13}C υ in cm^{-1}
948	ϕ HCCC (41); δ HCC (39)	943
1025	ϕ HCCH (85)	1023
1070	ϕ HCCC (61)	1055
1189	ϕ HCCC (-27); δ HCC (25)	1166
1326	δ HCC (70)	1315
1407	δ HCH (90)	1397
1448	δ HCH (69)	1437
1480	δ HCH (-77)	1477
1494	δ HCH (-64)	1491
1704	v CC (68)	1649

Table 2.20. DFT-computed Raman frequencies and normal mode analysis for propionaldehyde

propionaldehyde		
^{12}C υ in cm^{-1}	Major vibrational component (PED %)	^{13}C υ in cm^{-1}
905	ϕ HCCC (59)	900
1004	ν CC (42); ϕ HCCC (38)	990
1108	ϕ HCCC (27); ν CC (-25)	1082
1144	ϕ HCCC (43)	1123
1279	δ HCC (51)	1271
1362	ϕ HCCC (-35); δ HCH (-22)	1339
1408	δ HCH (-82)	1401
1422	δ HCH (74)	1415
1449	δ HCH (70)	1443
1494	δ HCH (75)	1492
1501	δ HCH (-64)	1498
1803	ν OC (89)	1761

Table 2.21. DFT-computed Raman frequencies and normal mode analysis for acetone

acetone		
^{12}C υ in cm^{-1}	Major vibrational component (PED %)	^{13}C υ in cm^{-1}
889	ϕ HCCC (-48)	877
1083	ϕ HCCC (-64)	1071
1116	ϕ HCCC (33); ϕ_{out} OCCC (-32)	1093
1232	ν CC (38)	1198
1386	δ HCH (-82)	1372
1387	δ HCH (93)	1375
1461	δ HCH (-73)	1459
1465	δ HCH (-74)	1462
1472	δ HCH (-73)	1469
1488	δ HCH (70)	1485
1786	ν OC (90)	1743

Table 2.22. DFT-computed Raman frequencies and normal mode analysis for hydroxyacetone

hydroxyacetone		
^{12}C υ in cm^{-1}	Major vibrational component (PED %)	^{13}C υ in cm^{-1}
856	ϕ HCCC (64)	847
983	ϕ HCCC (-34); ν CC (31)	966
1090	ϕ HCCC (47)	1068
1112	ν OC (71)	1092
1199	ν CC (16); ν CC (-12); ϕ HCCC (15); ϕ HCCC (-15)	1174
1251	δ HCO (71)	1247
1294	δ HOC (45)	1280
1391	δ HCH (89)	1379
1432	δ HCH (45)	1419
1466	δ HCH (-63)	1463
1477	ϕ HCCC (35); δ HCH (-33)	1473
1480	δ HCH (-39)	1477
1776	ν OC (89)	1733

Table 2.23. DFT-computed Raman frequencies and normal mode analysis for allyl alcohol

allyl alcohol		
^{12}C υ in cm^{-1}	Major vibrational component (PED %)	^{13}C υ in cm^{-1}
886	ν_s CC (71)	863
954	ϕ HCCC (98)	945
1004	δ HCC (46)	992
1018	ϕ HCCC (89)	1011
1038	ϕ HCCO (-55)	1024
1133	ν_s OC (48)	1113
1226	δ HOC (72)	1221
1257	δ HCO (89)	1256
1323	δ HCC (71)	1310
1429	ϕ HOCH (-41)	1418
1455	δ HCC (-34)	1440
1501	δ HCH (80)	1497
1708	ν_s CC (72)	1651

Table 2.24. DFT-computed Raman frequencies and normal mode analysis for butanol

butanol		
^{12}C υ in cm^{-1}	Major vibrational component (PED %)	^{13}C υ in cm^{-1}
978	ϕ HCCC (11); ϕ HCOH (-10); ϕ HCCC (16); ϕ HCCC (-22)	971
1033	ν_{as} OC (-65)	1006
1072	ν_{s} CC (75)	1048
1118	ν_{as} OC (-15); δ HOC (-11); ϕ HCCC (-20)	1101
1156	ϕ HCCC (-12); ϕ HCCC (11); ϕ HCCC (-16); ϕ OCCC (-12)	1134
1231	δ HOC (33); δ HCC (14); ϕ HCCC (-13)	1220
1257	ϕ HCCC (37); δ HCO (-14)	1250
1301	δ HOC (-20); δ HCC (32)	1292
1332	δ HCC (38); ϕ HCCC (-12);	1323
1340	δ HCC (34)	1334
1403	ϕ HCCC (-50)	1384
1414	δ HCH (92)	1404
1443	δ HCO (39)	1428
1476	δ HCH (76)	1472
1496	δ HCH (-68)	1494
1501	δ HCH (73)	1499
1510	δ HCH (75)	1506
1516	δ HCH (81)	1512

Table 2.25. Experimentally measured isotopological shifts, $v(^{13}C) - v(^{12}C)$, for vibrational modes of methanol compared with corresponding DFT-computed isotopological shifts. Modes are identified by their DFT-computed frequency. The SD in the measured isotopological shift is also provided in parentheses. All values tabulated here are wavenumbers in cm^{-1} units.

mode frequency	measured shift (SD)	DFT-computed shift
1040	-16.3 (8)	-16
1072	-11.5 (7)	-8
1168	-5.4 (8)	-8
1360	-6.5 (8)	-8
1480	-12.6 (3)	-8
1496	4.2 (8)	0
1504	1.1 (7)	0

Table 2.26. Experimentally measured isotopological shifts, $v(^{13}C) - v(^{12}C)$, for vibrational modes of acetic acid compared with corresponding DFT-computed isotopological shifts. Modes are identified by their DFT-computed frequency. The SD in the measured isotopological shift is also provided in parentheses. All values tabulated here are wavenumbers in cm^{-1} units.

mode frequency	measured shift (SD)	DFT-computed shift
999	-6.5 (9)	-10
1067	-24.7 (8)	-19
1205	-13.8 (7)	-15
1332	-20.9 (8)	-19
1408	-20.4 (7)	-16
1472	-3.4 (7)	-2
1818	-37.7 (4)	-45

Table 2.27. Experimentally measured isotopological shifts, $\nu(^{13}C) - \nu(^{12}C)$, for vibrational modes of acetone compared with corresponding DFT-computed isotopological shifts. Modes are identified by their DFT-computed frequency. The SD in the measured isotopological shift is also provided in parentheses. All values tabulated here are wavenumbers in cm $^{-1}$ units.

mode frequency	measured shift (SD)	DFT-computed shift
889	-16.7 (8)	-12
1083	-15.0 (8)	-12
1116	-29.4 (8)	-23
1232	-32.9 (8)	-34
1386	-13.5 (5)	-14
1461	-5.7 (5)	-2
1472	-1.4 (7)	-3
1488	-11.4 (7)	-3
1786	-40.8 (6)	-43

Table 2.28. Experimentally measured isotopological shifts, $\nu(^{13}C) - \nu(^{12}C)$, for vibrational modes of butanol compared with corresponding DFT-computed isotopological shifts. Modes are identified by their DFT-computed frequency. The SD in the measured isotopological shift is also provided in parentheses. All values tabulated here are wavenumbers in cm $^{-1}$ units.

mode frequency	measured shift (SD)	DFT-computed shift
978	-8.6 (8)	-7
1033	-27.6 (8)	-27
1072	-24.9 (7)	-24
1118	-18.7 (7)	-17
1156	-19.3 (8)	-22
1231	-11.3 (6)	-11
1257	-7.8 (8)	-7
1301	-6.2 (8)	-9
1332	-11.5 (7)	-9
1340	-8.8 (7)	-6
1403	-22.7 (8)	-19
1414	-10.7 (8)	-10
1443	-9.4 (8)	-15
1476	-9.0 (8)	-4
1496	-6.9 (8)	-2

Table 2.29. Experimentally measured isotopological shifts, $\nu(^{13}C) - \nu(^{12}C)$, for vibrational modes of oxalic acid compared with corresponding DFT-computed isotopological shifts. Modes are identified by their DFT-computed frequency. The SD in the measured isotopological shift is also provided in parentheses. All values tabulated here are wavenumbers in cm $^{-1}$ units.

mode frequency	measured shift (SD)	DFT-computed shift
839	-31.7 (9)	-29
1139	-15.5 (8)	-12
1207	-16.6 (7)	-9
1325	-20.3 (8)	-17
1399	-34.9 (8)	-35
1826	-30.7 (7)	-43

Table 2.30. Experimentally measured isotopological shifts, $\nu(^{13}C) - \nu(^{12}C)$, for vibrational modes of glycolaldehyde compared with corresponding DFT-computed isotopological shifts. Modes are identified by their DFT-computed frequency. The SD in the measured isotopological shift is also provided in parentheses. All values tabulated here are wavenumbers in cm $^{-1}$ units.

mode frequency	measured shift (SD)	DFT-computed shift
852	-20.6 (8)	-20
1100	-10.5 (8)	-19
1131	-24.6 (6)	-23
1212	-1.3 (8)	-3
1257	-5.1 (8)	-3
1411	-5.5 (7)	-6
1428	-22.1 (7)	-16
1480	-10.5 (7)	-6
1831	-35.7 (7)	-43

Table 2.31. Experimentally measured isotopological shifts, $\nu(^{13}C) - \nu(^{12}C)$, for vibrational modes of glyoxal compared with corresponding DFT-computed isotopological shifts. Modes are identified by their DFT-computed frequency. The SD in the measured isotopological shift is also provided in parentheses. All values tabulated here are wavenumbers in cm $^{-1}$ units.

mode frequency	measured shift (SD)	DFT-computed shift
810.0	-1.3 (7)	-5
1059	-32.0 (6)	-35
1072	-15.1 (6)	-20
1334	-8.4 (6)	-6
1376	0.5(8)	-3
1798	-39.2 (0)	-40

Table 2.32. Experimentally measured isotopological shifts, $\nu(^{13}C) - \nu(^{12}C)$, for vibrational modes of allyl alcohol compared with corresponding DFT-computed isotopological shifts. Modes are identified by their DFT-computed frequency. The SD in the measured isotopological shift is also provided in parentheses. All values tabulated here are wavenumbers in cm $^{-1}$ units.

mode frequency	measured shift (SD)	DFT-computed shift
954	-6.2 (8)	-9
1004	-18.2 (8)	-12
1018	-2.6 (8)	-7
1038	-15.3 (8)	-14
1133	-21.6 (8)	-20
1226	-2.9 (8)	-5
1257	1.6 (9)	-1
1323	-11.2 (6)	-13
1429	-13.9 (8)	-11
1455	-18.4 (8)	-15
1501	1.6 (8)	-4
1708	-52.8 (7)	-57

Table 2.33. Experimentally measured isotopological shifts, $\nu(^{13}C) - \nu(^{12}C)$, for vibrational modes of propane compared with corresponding DFT-computed isotopological shifts. Modes are identified by their DFT-computed frequency. The SD in the measured isotopological shift is also provided in parentheses. All values tabulated here are wavenumbers in cm $^{-1}$ units.

mode frequency	measured shift (SD)	DFT-computed shift
914	4.8 (8)	-4
932	-11.3 (8)	-7
1056	-28.1 (8)	-28
1174	-22.2 (8)	-22
1212	-21.8 (8)	-21
1317	-2.0 (6)	-6
1367	-22.8 (8)	-16
1404	-5.8 (7)	-11
1421	-15.8 (8)	-11
1490	0.6 (7)	-2
1507	0.6 (8)	-2

Table 2.34. Experimentally measured isotopological shifts, $\nu(^{13}C) - \nu(^{12}C)$, for vibrational modes of hydroxyacetone compared with corresponding DFT-computed isotopological shifts. Modes are identified by their DFT-computed frequency. The SD in the measured isotopological shift is also provided in parentheses. All values tabulated here are wavenumbers in cm $^{-1}$ units.

mode frequency	measured shift (SD)	DFT-computed shift
983	-15.7 (7)	-17
1090	-25.9 (8)	-22
1112	-21.6 (8)	-20
1199	-24.3 (6)	-25
1251	-8.3 (8)	-4
1294	-10.7 (8)	-14
1391	-10.1 (7)	-12
1432	-13.3 (9)	-13
1466	-0.7 (7)	-3
1480	-0.9 (7)	-3
1776	-42.9 (8)	-43

Table 2.35. Experimentally measured isotopological shifts, $\nu(^{13}C) - \nu(^{12}C)$, for vibrational modes of propionaldehyde compared with corresponding DFT-computed isotopological shifts. Modes are identified by their DFT-computed frequency. The SD in the measured isotopological shift is also provided in parentheses. All values tabulated here are wavenumbers in cm^{-1} units.

mode frequency	measured shift (SD)	DFT-computed shift
905	-5.1 (8)	-5
1004	-15.4 (8)	-14
1108	-20.7 (6)	-26
1144	-19.2 (8)	-21
1279	-5.6 (8)	-8
1362	-18.4 (8)	-23
1408	-6.3 (8)	-7
1422	-7.6 (8)	-7
1449	-6.9 (8)	-6
1494	0.6 (7)	-2
1501	1.1 (7)	-3
1803	-39.6 (6)	-42

Table 2.36. Experimentally measured isotopological shifts, $\nu(^{13}C) - \nu(^{12}C)$, for vibrational modes of propene compared with corresponding DFT-computed isotopological shifts. Modes are identified by their DFT-computed frequency. The SD in the measured isotopological shift is also provided in parentheses. All values tabulated here are wavenumbers in cm^{-1} units.

mode frequency	measured shift (SD)	DFT-computed shift
923	-26.0 (7)	-24
948	-5.6 (8)	-5
1025	-2.6 (7)	-2
1070	-16.9 (8)	-15
1189	-19.9 (8)	-23
1326	-14.0 (8)	-11
1407	-13.8 (8)	-10
1448	-10.8 (8)	-11
1480	-1.7 (8)	-3
1494	1.9 (8)	-3
1704	-55.5 (8)	-55

Table 2.37. Experimentally measured isotopological shifts, $\nu(^{13}C) - \nu(^{12}C)$, for vibrational modes of propanol compared with corresponding DFT-computed isotopological shifts. Modes are identified by their DFT-computed frequency. The SD in the measured isotopological shift is also provided in parentheses. All values tabulated here are wavenumbers in cm $^{-1}$ units.

mode frequency	measured shift (SD)	DFT-computed shift
926	-8.3 (8)	-7
979	-10.5 (6)	-13
1061	-27.5 (9)	-25
1109	-20.3 (8)	-18
1156	-16.4 (7)	-20
1239	-6.8 (8)	-9
1271	-7.5 (7)	-6
1322	-6.6 (8)	-6
1380	-19.7 (8)	-15
1410	-14.6 (8)	-12
1444	-10.1 (8)	-15
1478	-9.3 (8)	-4
1495	-4.0 (8)	-2
1518	-7.1 (8)	-4

Table 2.38. Experimentally measured isotopological shifts, $\nu(^{13}C) - \nu(^{12}C)$, for vibrational modes of methane compared with corresponding DFT-computed isotopological shifts. Modes are identified by their DFT-computed frequency. The SD in the measured isotopological shift is also provided in parentheses. All values tabulated here are wavenumbers in cm $^{-1}$ units.

mode frequency	measured shift (SD)	DFT-computed shift
1340	-8.0 (7)	-9
1558	-3.2 (9)	0
3026	0.8 (6)	0
3132	-	-11

Table 2.39. Experimentally measured isotopological shifts, $\nu(^{13}C) - \nu(^{12}C)$, for vibrational modes of formic acid compared with corresponding DFT-computed isotopological shifts. Modes are identified by their DFT-computed frequency. The SD in the measured isotopological shift is also provided in parentheses. All values tabulated here are wavenumbers in cm $^{-1}$ units.

mode frequency	measured shift (SD)	DFT-computed shift
1050	-43.9 (5)	-41
1128	-18.3 (3)	-12
1266	9.9 (6)	10
1421	-14.1 (8)	-19
1792	-	-29

Table 2.40. Experimentally measured isotopological shifts, $\nu(^{13}C) - \nu(^{12}C)$, for vibrational modes of formaldehyde compared with corresponding DFT-computed isotopological shifts. Modes are identified by their DFT-computed frequency. The SD in the measured isotopological shift is also provided in parentheses. All values tabulated here are wavenumbers in cm $^{-1}$ units.

mode frequency	measured shift (SD)	DFT-computed shift
1201	-12.7 (8)	-12
1259	-9.2 (6)	-10
1530	-2.4 (7)	0
1813	-37.8 (8)	-40
2889	-3.6 (5)	-4
2948	-12.5 (7)	-13

Table 2.41. Experimentally measured isotopological shifts, $\nu(^{13}C) - \nu(^{12}C)$, for vibrational modes of acetaldehyde compared with corresponding DFT-computed isotopological shifts. Modes are identified by their DFT-computed frequency. The SD in the measured isotopological shift is also provided in parentheses. All values tabulated here are wavenumbers in cm $^{-1}$ units.

mode frequency	measured shift (SD)	DFT-computed shift
886	-21.0 (6)	-18
1133	-27.5 (7)	-20
1377	-8.4 (8)	-11
1420	-5.6 (6)	-5
1460	-2.9 (5)	-2
1469	-9.0 (7)	-2
1808	0.0 (0)	-43
2871	-9.4 (7)	-8

Table 2.42. Experimentally measured isotopological shifts, $\nu(^{13}C) - \nu(^{12}C)$, for vibrational modes of ethane compared with corresponding DFT-computed isotopological shifts. Modes are identified by their DFT-computed frequency. The SD in the measured isotopological shift is also provided in parentheses. All values tabulated here are wavenumbers in cm $^{-1}$ units.

mode frequency	measured shift (SD)	DFT-computed shift
996	-36.0 (6)	-31
1217	-14.3 (7)	-16
1408	-11.3 (7)	-10
1423	-15.8 (7)	-11
1503	0.1 (7)	-1

Table 2.43. Experimentally measured isotopological shifts, $\nu(^{13}C) - \nu(^{12}C)$, for vibrational modes of ethylene glycol compared with corresponding DFT-computed isotopological shifts. Modes are identified by their DFT-computed frequency. The SD in the measured isotopological shift is also provided in parentheses. All values tabulated here are wavenumbers in cm $^{-1}$ units.

mode frequency	measured shift (SD)	DFT-computed shift
871	3.1 (7)	0
1034	-13.4 (8)	-17
1045	-17.2 (7)	-15
1096	-25.3 (7)	-23
1183	-5.8 (8)	-6
1243	-14.2 (8)	-11
1376	-7.2 (8)	-6
1396	-6.1 (7)	-9
1411	-13.9 (7)	-13
1486	-2.6 (7)	-4
1491	-5.9 (7)	-4

Table 2.44. Experimentally measured isotopological shifts, $v(^{13}C) - v(^{12}C)$, for vibrational modes of ethylene compared with corresponding DFT-computed isotopological shifts. Modes are identified by their DFT-computed frequency. The SD in the measured isotopological shift is also provided in parentheses. All values tabulated here are wavenumbers in cm^{-1} units.

mode frequency	measured shift (SD)	DFT-computed shift
977	-10.3 (8)	-8
1058	-1.2 (5)	0
1238	-16.6 (6)	-18
1378	-13.5 (8)	-13
1472	-10.5 (7)	-6
1684	-41.9 (7)	-47

Table 2.45. Experimentally measured isotopological shifts, $v(^{13}C) - v(^{12}C)$, for vibrational modes of ethanol compared with corresponding DFT-computed isotopological shifts. Modes are identified by their DFT-computed frequency. The SD in the measured isotopological shift is also provided in parentheses. All values tabulated here are wavenumbers in cm^{-1} units.

mode frequency	measured shift (SD)	DFT-computed shift
897	-15.8 (9)	-15
1032	-19.0 (8)	-22
1094	-19.1 (7)	-17
1176	-12.4 (8)	-16
1262	-11.7 (6)	-8
1299	-6.1 (8)	-4
1404	-7.6 (7)	-10
1448	-18.8 (8)	-16
1481	-5.4 (7)	-2
1500	-0.1 (8)	-3
1526	-8.8 (8)	-5

Table 2.46. Parameters and expressions used for the determination of the average time between photon absorption events.

Parameters	**Equations**	**Magnitude**	**Units**
excitation wavelength (λ)		514.5	nm
photon energy	$E = \frac{hc}{\lambda}$	2.41	eV
photon energy (E)	1 eV = 1.6 x 10^{-19} J	3.86 x 10^{-19}	J
laser power (P)		10	mW
beam diameter (φ)		10.8	µm
beam area (A)	$A = \pi \left(\frac{\varphi}{2}\right)^2$	9.15 x 10^{-11}	m^2
intensity (I)	$I = P/A$	1.09 x 10^{8}	$W.m^{-2}$
absorption cross-section (σ)		5.12 x 10^{-15}	m^2
absorbed power (P_{abs})	$P_{abs} = I.\sigma$	5.58 x 10^{-7}	W
rate of photon absorption (R_{abs})	$R_{abs} = P_{abs}/E$	1.45 x 10^{12}	s^{-1}
average time between photon absorption events (τ)	$\tau = 1/R_{abs}$	6.90 x 10^{-13}	s
		690	fs

CHAPTER 3

STOCHASTIC NOISE AND CORRELATIONS IN NANOPARTICLE CATALYSIS

This chapter is based on an article that is expected to be submitted for publication. I designed experiments, performed sample preparation, SERS experiments, analysis, and co-wrote the manuscript. Prof. Prashant K. Jain conceived project, designed experiments, provided analyses and interpretation of results, and co-wrote the manuscript.

3.1. INTRODUCTION

The design of an effective solid-state catalyst for a chemical conversion requires detailed knowledge of the chemical dynamics occurring when the catalyst is in action. Over the past decade, tremendous progress has been made in this direction. In-situ microscropic, nanoscopic, and single-molecule-level spectroscopic tools[28,29,64–68,173–188] have elucidated the elementary catalytic events occurring on the surface of the catalyst in real time.[25,45,53,68,103,189–229] Owing to their improved spatial and temporal resolution, as compared to conventional bulk-level interrogations, these studies have revealed that catalysts are heterogeneous. Catalytic activity can vary spatially—on nanometer and micron scales—and also sometimes in time.[28,29,64–68] Such spatial variation of catalytic behavior is often attributed to static differences in morphologies, structural features (facets, edges, or steps), or chemical environments of individual grains of the catalyst.[230–239] Temporal changes in activity are assigned to dynamics in the surface structure or composition of the catalyst resulting from processes such as adsorbate-induced surface restructuring, poisoning of the surface, or sintering of grains.[240–246]

In plasmon-driven CO_2 reduction reaction (CO_2RR)[84–86,247–251] on Ag nanoparticles (NPs), for which we recently developed in-situ single-NP level monitoring,[45,252] we observe similar NP-to-NP heterogeneity in the profile of species produced. However, the heterogeneity observed here, we argue, is a reflection of the inherent stochasticity (noise) in catalytic events taking place on the NPs.

Consider a hypothetical population of catalytic grains identical in every chemical aspect, including their environment. Even in such a case, where all extrinsic factors of variation have been eliminated, there remains the noise resulting from thermal fluctuations and inherent randomness of individual chemical events. Such noise is not conventionally manifested in measured catalytic activity; it gets smeared out in a measurement that averages over a large sample set of either spatial locations or timepoints. However, the single-NP-level, single-molecule-level detection of events implemented here results in the noise being captured in the form of variation in catalytic activity across NPs and analogously also in time. We also exploit this variation to deduce correlations between different surface species, which in turn shed mechanistic light on the formation of multicarbon compounds[135,137,141,253–258] in CO_2RR.

3.2. RESULTS AND DISCUSSION

As reported in our recent work[252], we used in-situ surface enhanced Raman scattering (SERS) nanoscopy to probe with single-molecule-level resolution the CO_2RR driven by plasmonic excitation on a Ag NP photocatalyst. Under 10 mW of 514.5 nm laser excitation (10.8 µm diameter spot), continuous SERS spectra were collected every 200 ms from individual diffraction-limited Ag NP scatterers in CO_2-saturated water. These scatterers are typically dimers or trimers of Ag NPs with localized surface plasmon resonance (LSPR) modes, the broad spectra of which overlap with the 514.5 nm laser excitation. As found in our previous study[252], LSPR-excitation-induced electronic transitions[79–82,259–263] drive CO_2RR on the Ag surface forming C_1–C_4 species, which are detected by SERS, as also found here (Fig. 3.6).

Fluctuations in CO_2RR activity. From SERS spectra acquired continuously over a period of 200 s, we constructed time-trajectories of CO_2RR activity on individual NP scatterers (Fig. 3.1). In these trajectories, the activity/inactivity toward C_1–C_4 formation is gauged by the appearance/lack of associated SERS vibrational peaks. The single-NP-level trajectories show fluctuations in the catalytic activity. First, a NP scatterer is not necessarily active throughout the observation time. Different C_1–C_4 species appear and disappear randomly on a scatterer. The catalytic activities of different scatterers are not in synchrony. The same species may appear up on two scatterers at two different times. The time-cumulative activity was also variable from one Ag NP scatterer to another. For instance, out of 61 scatterers investigated, the most prevalent species was butanol on 24 scatterers and ethylene glycol on 11 scatterers.

Variations across the population. For a more quantitative analysis of the observed variability in the catalytic activity, we determined the selectivities of C_1–C_4 formation on individual NP scatterers (see Methods). The selectivites vary from one NP scatterer to another (Fig. 3.2 and Fig. 3.7) and span a wide distribution over the full ensemble of NP scatterers studied (Fig. 3.4, top row). Prima facie, this variation can be thought to arise from differences[264–267] in the morphologies—such differences are known to be prevalent from our prior work,[252]—surface structures, and/or environments of the individual NP scatterers. However, static heterogeneities cannot be the sole source of the observed variations; because even on a single scatterer the C_1–C_4 formation activity fluctuates in time (Fig. 3.1).

Variations across time. To further examine the temporal fluctuations, we determined C_1–C_4 formation selectivities for each of 30 time segments over the full 200 s observation window (Figs. 3.3 and 3.8). The selectivities vary considerably from one time segment to another and span a distribution (Fig. 3.4, bottom row).

Variations originate from stochastic noise. The time-distribution of CO_2RR selectivities overlaps with the population-distribution (Fig. 3.4). The mean values of the selectivities are statistically similar for the two distributions (Table 3.1). Variations that yields similar time- and population-averages—a property known as ergodicity[268–271]—can be traced to stochastic thermal fluctuations. Typically, such stochastic behavior gets masked in a bulk-scale measurement that averages over a sample size that is in the thermodynamic limit. However, the single-NP-, one-event-per-frame-limit of the probing employed here preserves the stochastic noise in the catalytic activity occurring on a NP scatterer, which in turn is manifested in the observed variations (Figs. 3.2–3.4). It must however be noted that the population-distributions are significantly wider than the time-distributions (Fig. 3.4). This difference suggests that a portion of the measured NP-to-NP variations, especially the larger deviations from the mean (Fig. 3.4, top row), emanate from a source other than intrinsic noise, e.g., static heterogeneities.

In the in-situ probing employed here, chemical events occurring on the surface are sampled randomly rather than in a temporal/kinetic sequence. Nevertheless, we were able to exploit the NP-by-NP variation to draw insight into the elementary steps occurring in the catalysis. Using the C_1–C_4 formation selectivities measured on individual NP scatterers, we examined correlations between the formations of species of different C_n ($n = 1, 2, 3, 4$) categories (Fig. 3.5). The prevalence of C_3 formation was anti-correlated ($r = -0.62$) with the prevalence of $C_1 + C_2$ formation (Fig. 3.5a). This correlation may be explained by C_3 species being produced by the coupling of C_1

and C_2 species. Similarly, the prevalence of C_4 formation is anti-correlated ($r = -0.50$) with the prevalence of C_2 formation (Fig. 3.5b), which points to the coupling of C_2 species as a pathway for the production of C_4 species.

This study shows that at the single-NP-level, observed variations in catalytic activity may not all be due to static heterogeneities; in this small-sampling-limit, intrinsic noise in activity resulting from the stochasticity of catalytic events can be captured. This intrinsic noise can be identified by examining the overlap of the population-distribution and the time-distribution of the catalytic activity. Activity variations unique to the population-distribution may be attributable to static heterogeneities; on the other hand, variations unique to the time-distribution may be attributable to dynamic changes in the catalyst. We were able to exploit NP-to-NP variations in CO_2RR activity to elucidate mechanisms of formation of multicarbon compounds.

3.3. METHODS

Ag NPs were synthesized by the Lee–Meisel method.[105] The preparation of microfluidic reaction cells, in situ SERS spectroscopy of individual Ag NP scatterers under CO_2RR conditions in water, spectral analyses, and species assignment were performed as per the methods described in our past work.[252] The analysis presented in this work is based on 68 movies (each consisting of 1000 frames or SERS spectra) captured from 61 diffraction-limited Ag NP scatterers. It must be noted that of this total of 68,000 spectra, 42,000 spectra were from 40 Ag NP scatterers from our previous study[252] and 26,000 spectra correspond to newly acquired data. Spectra were assigned to species from a database. The prior database of compounds used for spectral assignments[252] was updated to include additional species: formate, acetate, oxalate, carbonate, butene, methyl glyoxal, 2,3-furandiol, pyruvate, and glyceraldehyde. Raman spectra of these species, in their gas-phase form, were calculated by density functional theory (DFT). The interpretation of DFT-computed Raman spectra and the assignment of vibrational frequencies to various local bond vibrations (modes) were performed by a potential energy distribution (PED) analysis in vibrational energy distribution analysis (VEDA) program, similar to our prior study.[252] DFT-computed Raman modes for these species are provided in Tables 3.2–3.10.

Tables 3.2–3.10 provide for each species the calculated vibrational frequencies, the corresponding dominant local mode/s, and their % contribution to the frequency estimated by the potential energy distribution (PED) distribution. Positive % contribution values indicate symmetric modes and negative values indicate antisymmetric modes of vibration. The following symbols are used to indicate various vibrational modes: ν_s–symmetric stretching; ν_{as}–antisymmetric stretching; δ–bending; ρ–rocking; τ–twisting; ω–wagging; ϕ–torsion.

Each frame of a spectral movie acquired from an individual NP scatterer was assigned to a species from the database. From this analysis, we determined for this scatterer the number of detection events (x_n) of species in the C_n category where $n = 1, 2, 3$, and 4. The % selectivity of C_n species was determined as: $\frac{x_n}{\sum_{n=1}^{4} x_n} \times 100$. The % selectivity of C_1–C_4 species for a scatterer was presented in the form of a pie chart. Such pie charts, compared across different NP scatterers, provide a gauge of the variation in CO_2RR activity from one NP scatterer to another.

To analyze the temporal variation in activity, each spectral movie consisting of 1000 frames was divided up into 30 time segments each containing 33 frames. The last 10 frames or spectra were omitted from this analysis. SERS spectra that were assigned to a particular species across all individual NP scatterers were then grouped together and categorized on the basis of the time segment they fall within. From this full-NP-ensemble-data, the % selectivity of C_1–C_4 species was determined for each time segment and represented as a pie chart. Such pie charts, compared across the 30 different time segments, provide a gauge of the temporal variation in CO_2RR activity of the full NP ensemble.

3.4. FIGURES

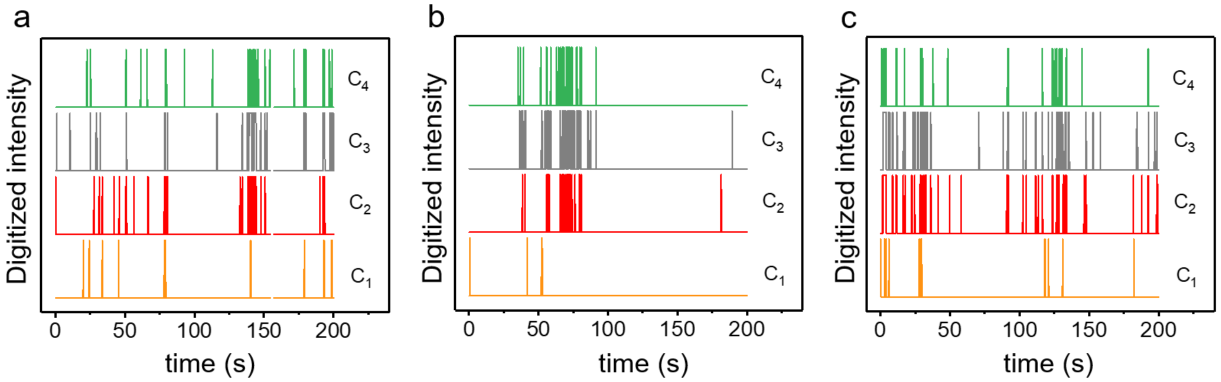

Figure 3.1. Digital time-trajectories of C_1–C_4 species. Trajectories showing the stochastic appearance and disappearance of C_1, C_2, C_3, and C_4 species on the surface of three different (a–c) diffraction-limited Ag NP scatterers in CO_2RR under plasmonic excitation. For the generation of digital trajectory, a spectral movie was analyzed to determine which species from the database are detected in each spectral frame. If any species from a specific C_n (n = 1, 2, 3, or 4) category is detected in a spectral frame, the intensity for that timepoint was assigned a value of "1" for that C_n category. Note that species from more than one category can be found in the same spectral frame. Conversely, if no species from a specific C_n (n = 1, 2, 3, or 4) category is detected in a spectral frame, the intensity for that timepoint was assigned a value of "0" for that C_n category. The resulting digitized intensity was plotted as a function of time. These plots are based on source data acquired in a prior study.[252]

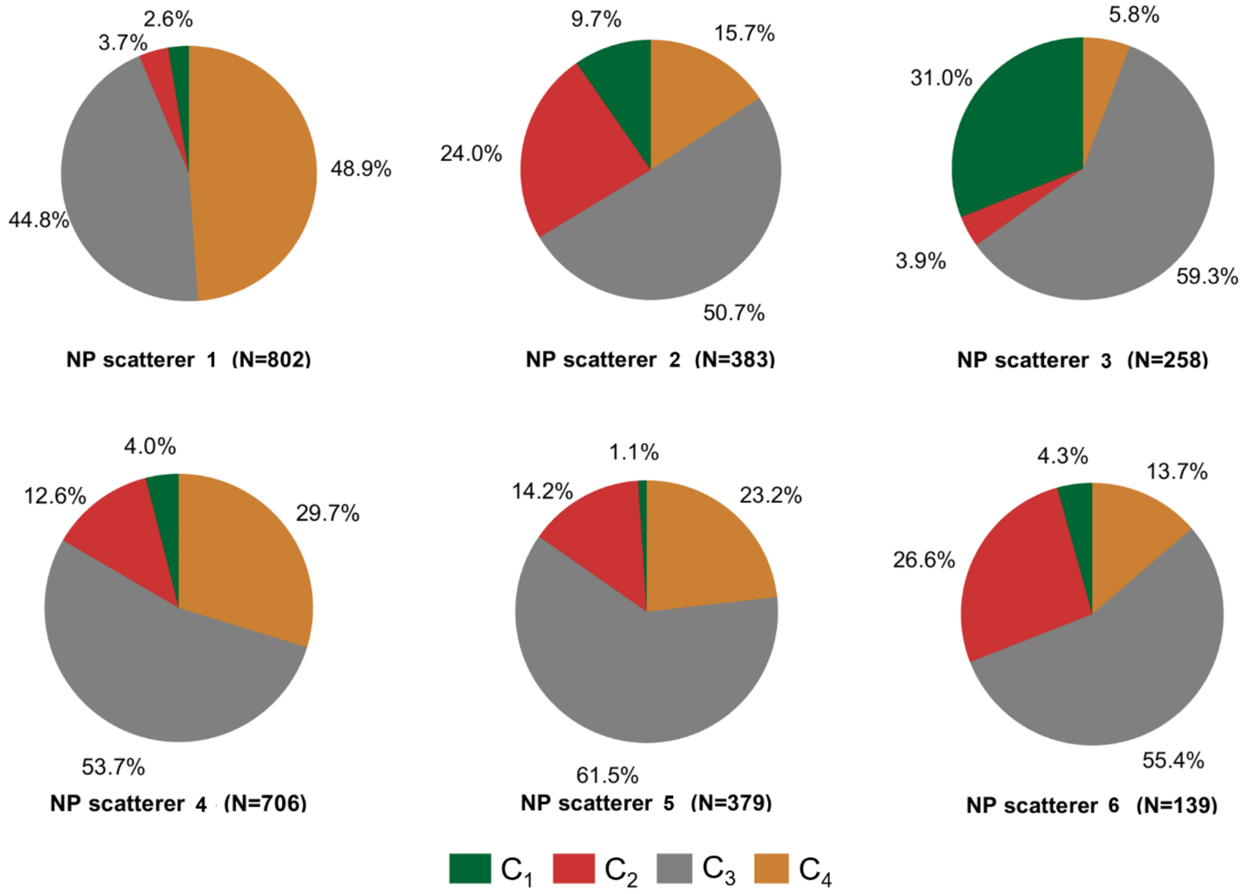

Figure 3.2. Variation in CO_2RR activity across the population of NP scatterers. Pie charts showing for different Ag NP scatterers the selectivities (%) of C_1–C_4 formation in CO_2RR under plasmonic excitation over the full time-course of observation. The number of spectra resulting in each pie chart is listed as N. Pie charts from six selected individual Ag NP scatterers are shown here; additional examples are provided in Fig. 3.7.

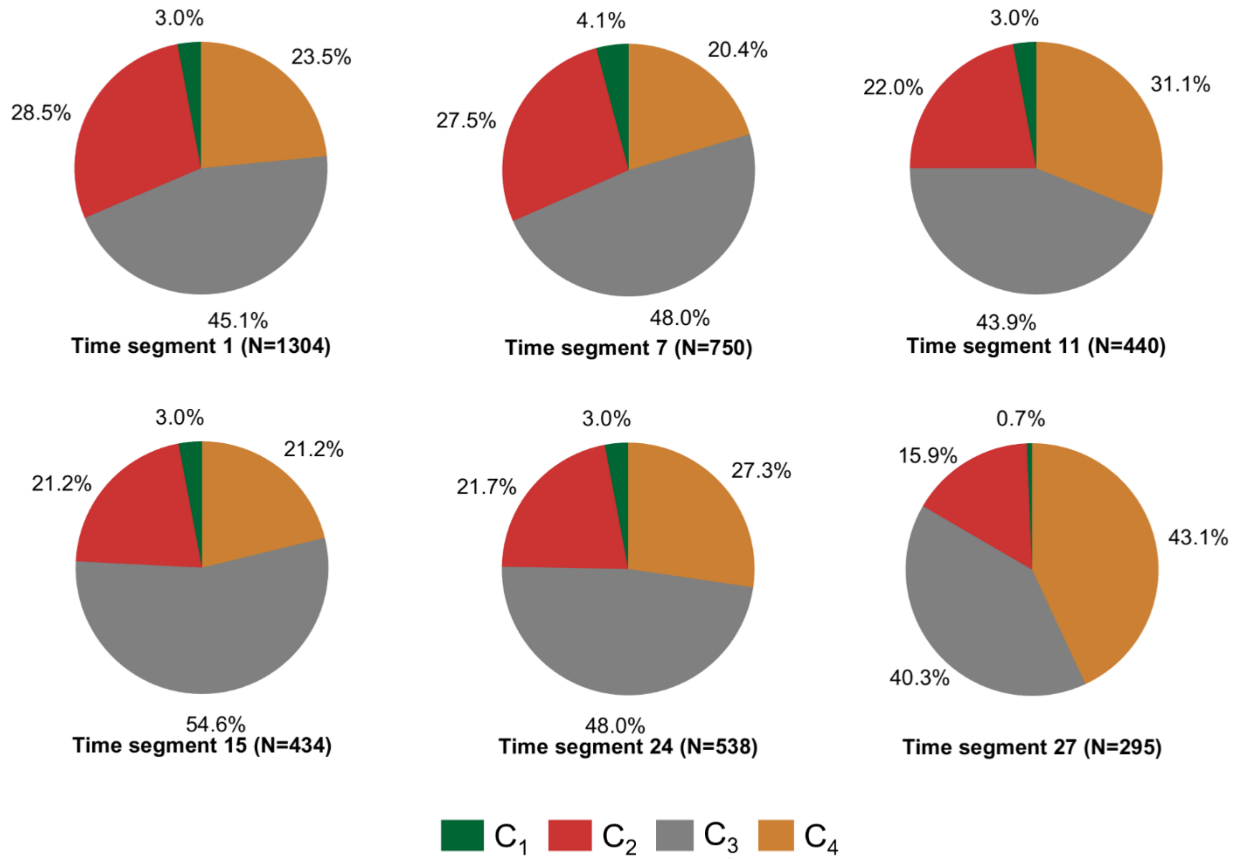

Figure 3.3. Temporal variation in CO_2RR activity. Pie charts showing for different time segments the selectivities (%) of C_1–C_4 formation determined for the full ensemble of Ag NPs in CO_2RR under plasmonic excitation. The number of spectra resulting in each pie chart is listed as N. Only selected time segments out of a total of 30 are shown here for brevity; the full set is provided in Fig. 3.8. 68, 000 spectra acquired from 61 Ag NP scatterers were analyzed. Of this, 42, 000 spectra obtained from 40 Ag NP scatterers are same as the source data analyzed in the previous manuscript.[252]

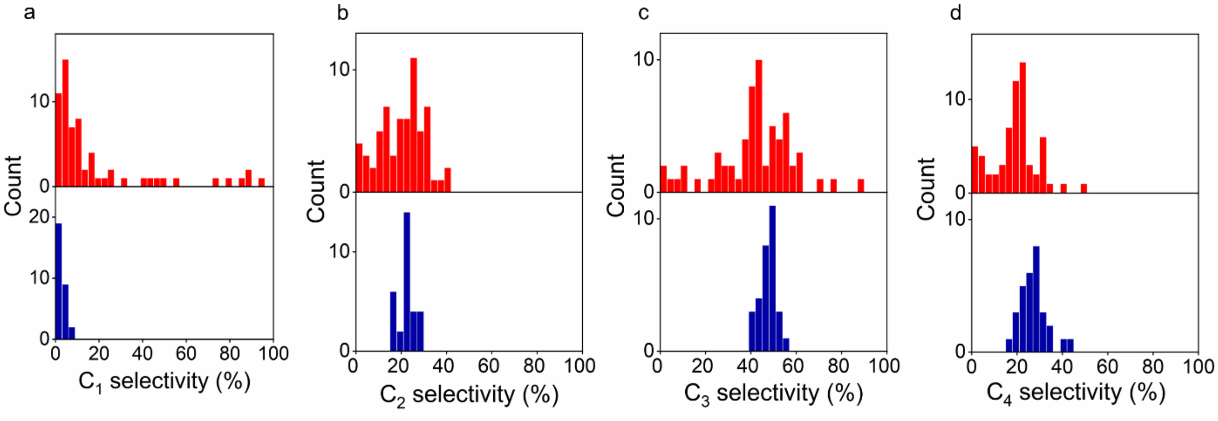

Figure 3.4. NP-to-NP variation in CO_2RR activity compared with temporal variation of CO_2RR activity. Histogram showing the distribution of % selectivity of C_1 (a), C_2 (b), C_3 (c) and C_4 (d) formation across different Ag NP scatterers in the ensemble (top, red) and across different time segments for the entire NP ensemble (bottom, blue). These histograms and associated statistical measures tabulated in Table 3.1 show close correspondence between the ensemble averages and the temporal averages of the CO_2RR selectivities. 68, 000 spectra acquired from 61 Ag NP scatterers were analyzed. Of this, 42, 000 spectra obtained from 40 Ag NP scatterers are same as the source data analyzed in the previous manuscript.[252]

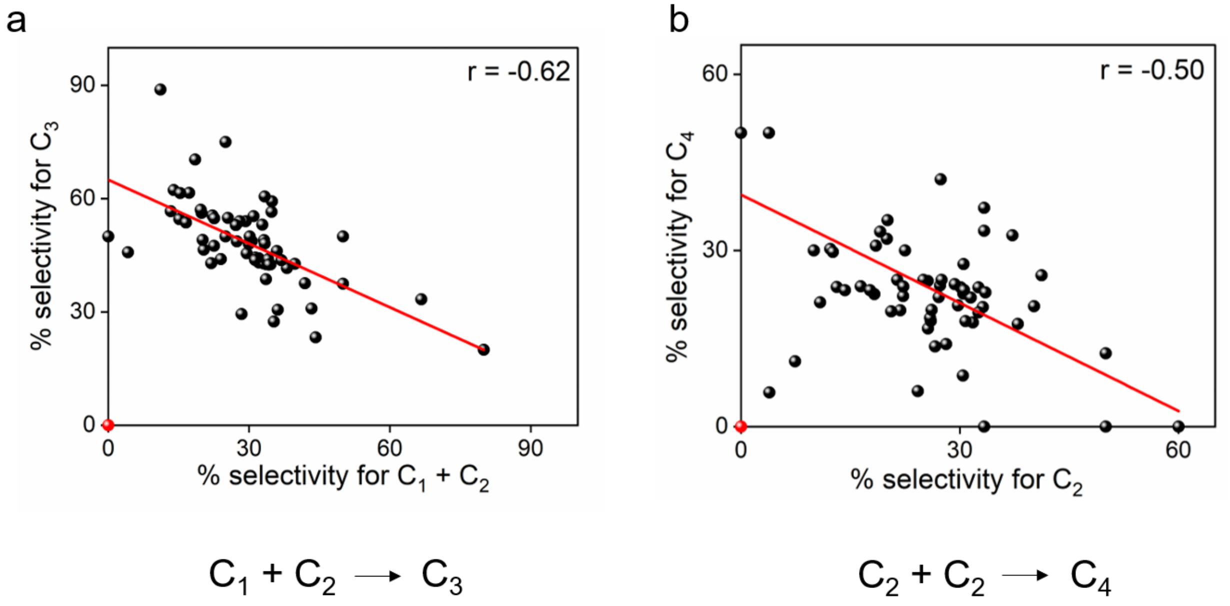

Figure 3.5. Correlations between formation of species of different C_n (n = 1, 2, 3, and 4) categories a) % selectivity of C_3 formation plotted vs. % selectivity of C_1 + C_2 formation and b) % selectivity of C_4 formation plotted vs. % selectivity of C_2 formation. Each individual data point (black dots) corresponds to % selectivities determined on an individual Ag NP scatterer in CO_2RR under plasmonic excitation. The linear correlation between the plotted quantities is shown by a straight line fit (solid line) and the corresponding Pearson's correlation coefficient, r, is listed. The trivial point (0, 0), which is marked red, was omitted from the correlation analysis in a and b. The analysis presented in this figure is based on 68, 000 spectra acquired from 61 Ag NP scatterers. Of this, 42, 000 spectra obtained from 40 Ag NP scatterers are same as the source data analyzed in the previous manuscript.[252]

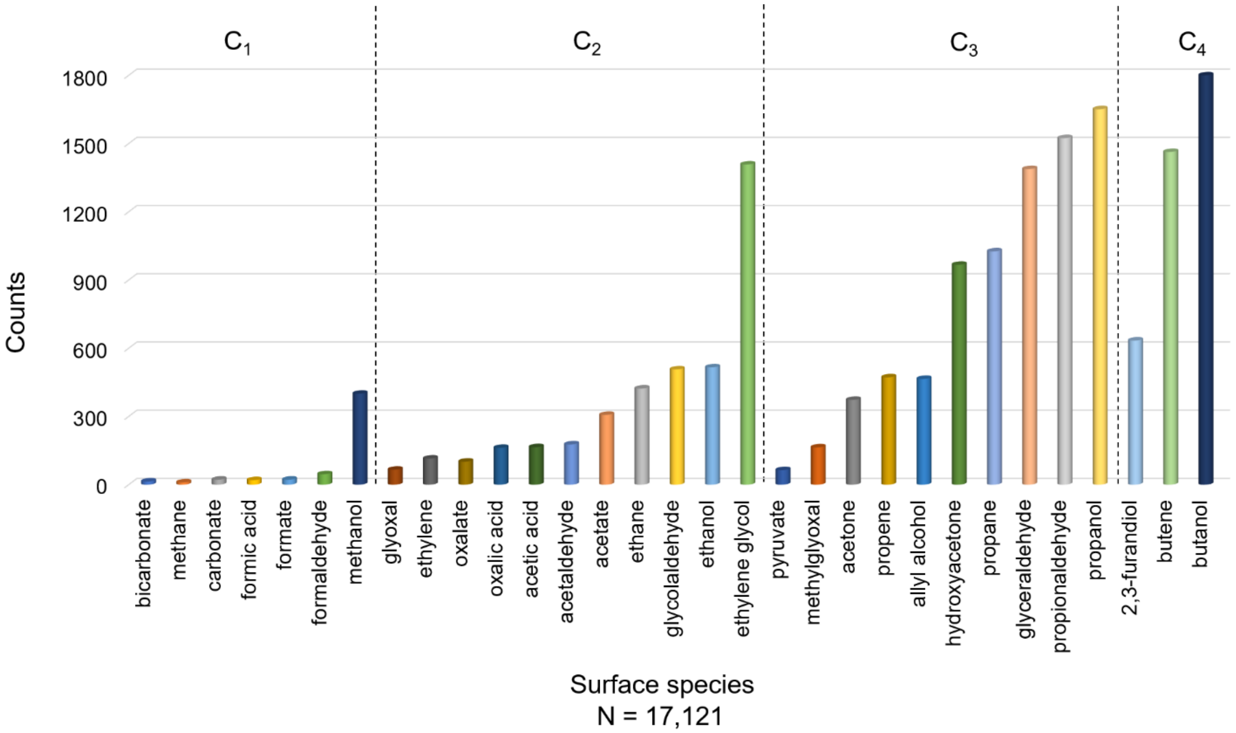

Figure 3.6. Bar plot showing the profile of surface species observed by in-situ nanoscale SERS spectroscopy in CO_2RR on Ag nanoparticles (NPs). Each species is shown by a bar of a different color. The species are grouped into C_1, C_2, C_3, and C_4 categories; within each category, they are presented in order of their prevalence. This distribution was determined from 68,000 SERS spectra acquired from 61 Ag NP scatterers in CO_2-saturated water under plasmonic excitation. Of this, 42,000 spectra obtained from 40 Ag NP scatterers are from source data acquired in a previous study.[S252]

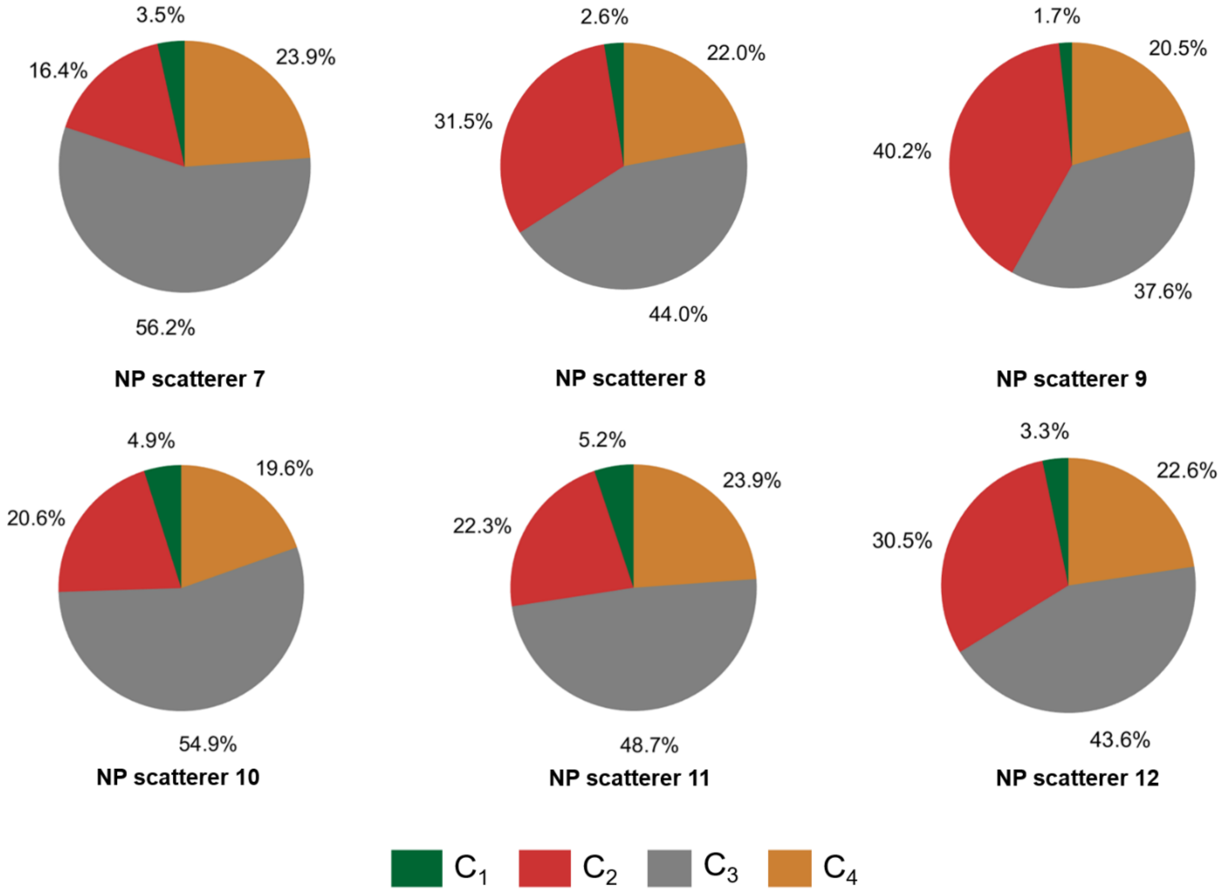

Figure 3.7. Variation in CO$_2$RR selectivity from one nanoscale location to another. Additional examples of pie charts showing for individual Ag NP scatterers the selectivities (%) of C_1–C_4 formation in CO$_2$RR under plasmonic excitation over the full time-course of observation. The pie chart is based on 201, 273, 117, 102, 310, and 548 active assigned spectra respectively for NP scatterer 7, NP scatterer 8, NP scatterer 9, NP scatterer 10, NP scatterer 11, and NP scatterer 12.

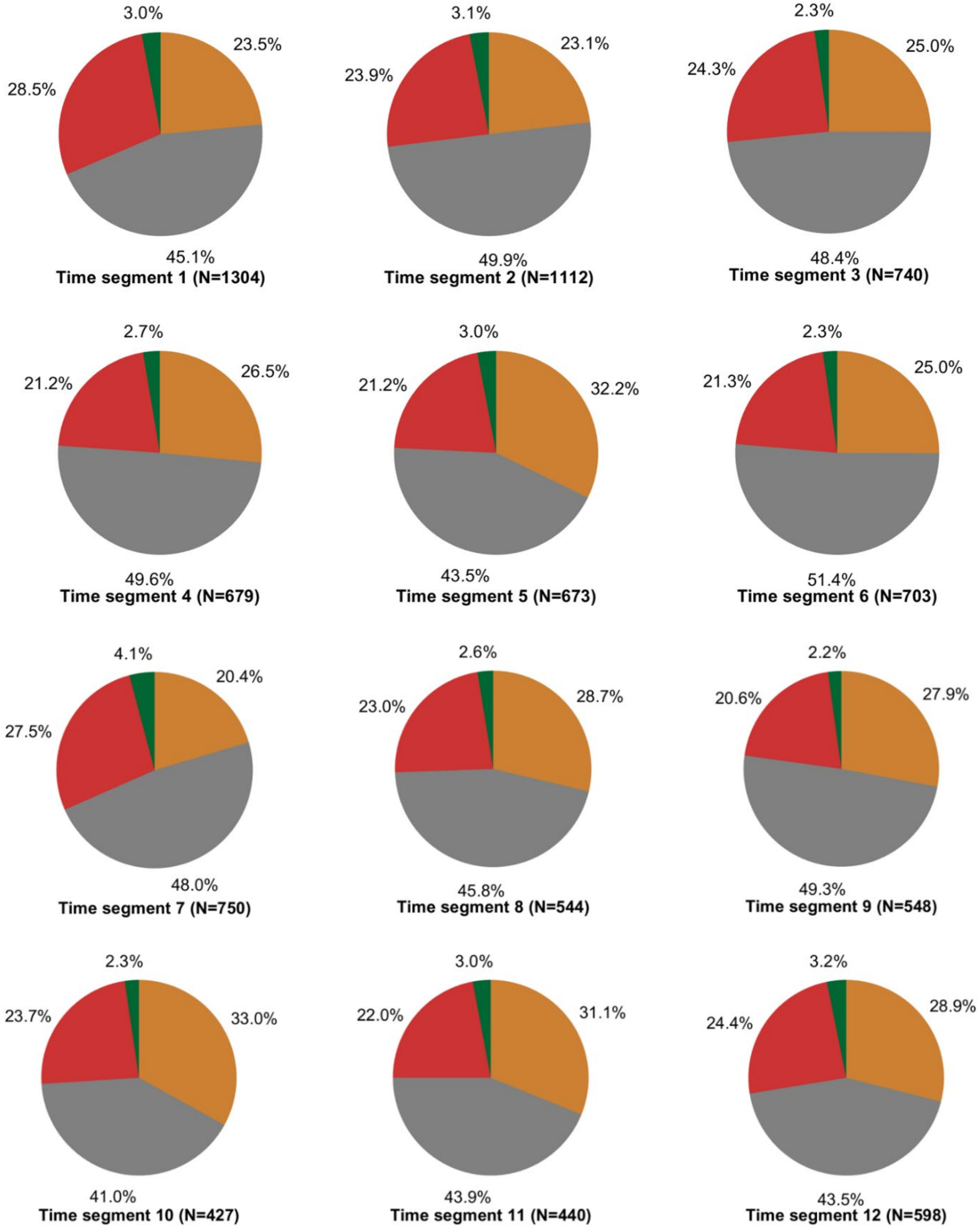

Figure 3.8. (cont.)

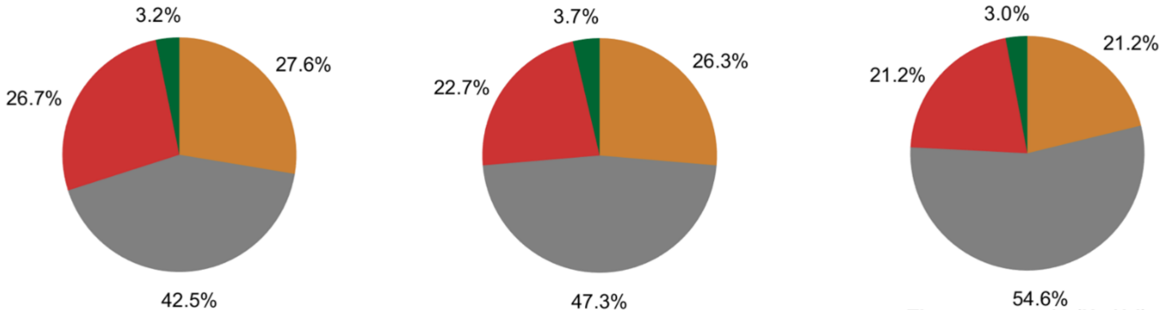

Time segment 13 (N=431) **Time segment 14 (N=353)** **Time segment 15 (N=434)**

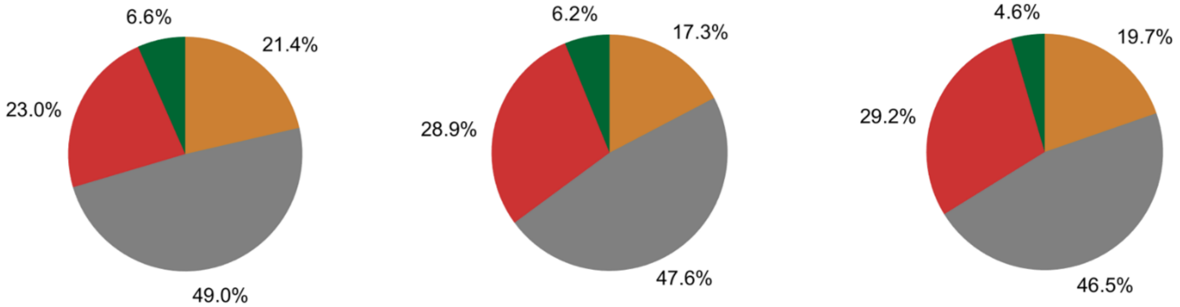

Time segment 16 (N=514) **Time segment 17 (N=681)** **Time segment 18 (N=742)**

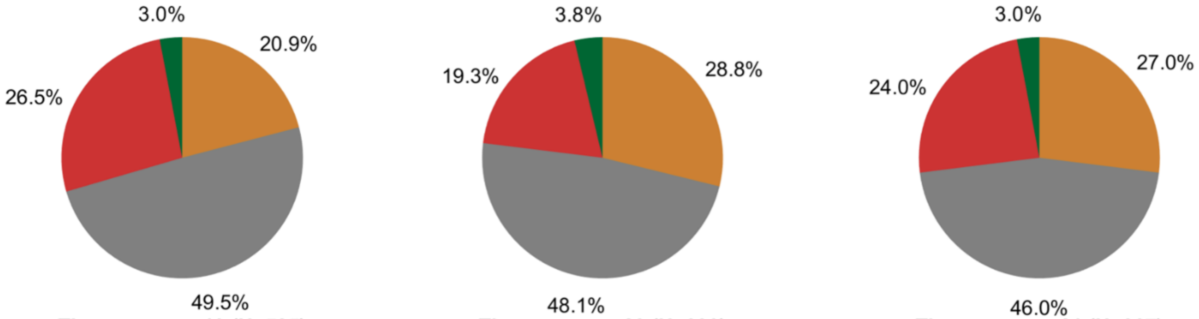

Time segment 19 (N=535) **Time segment 20 (N=399)** **Time segment 21 (N=367)**

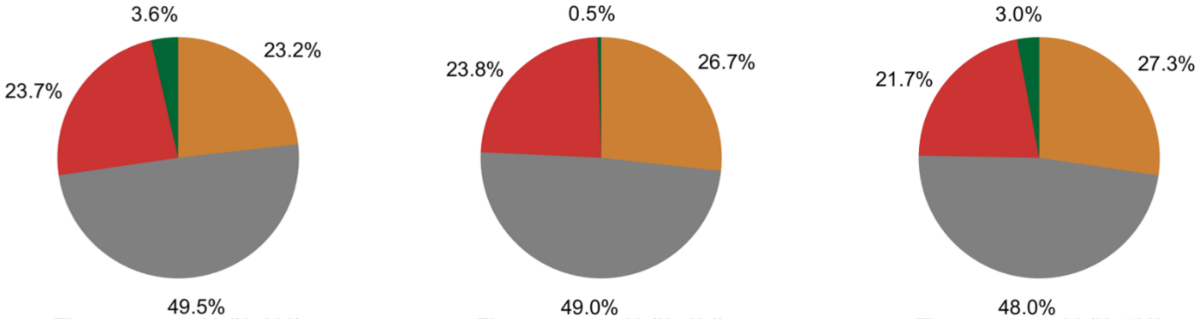

Time segment 22 (N=388) **Time segment 23 (N=404)** **Time segment 24 (N=538)**

Figure 3.8. (cont.)

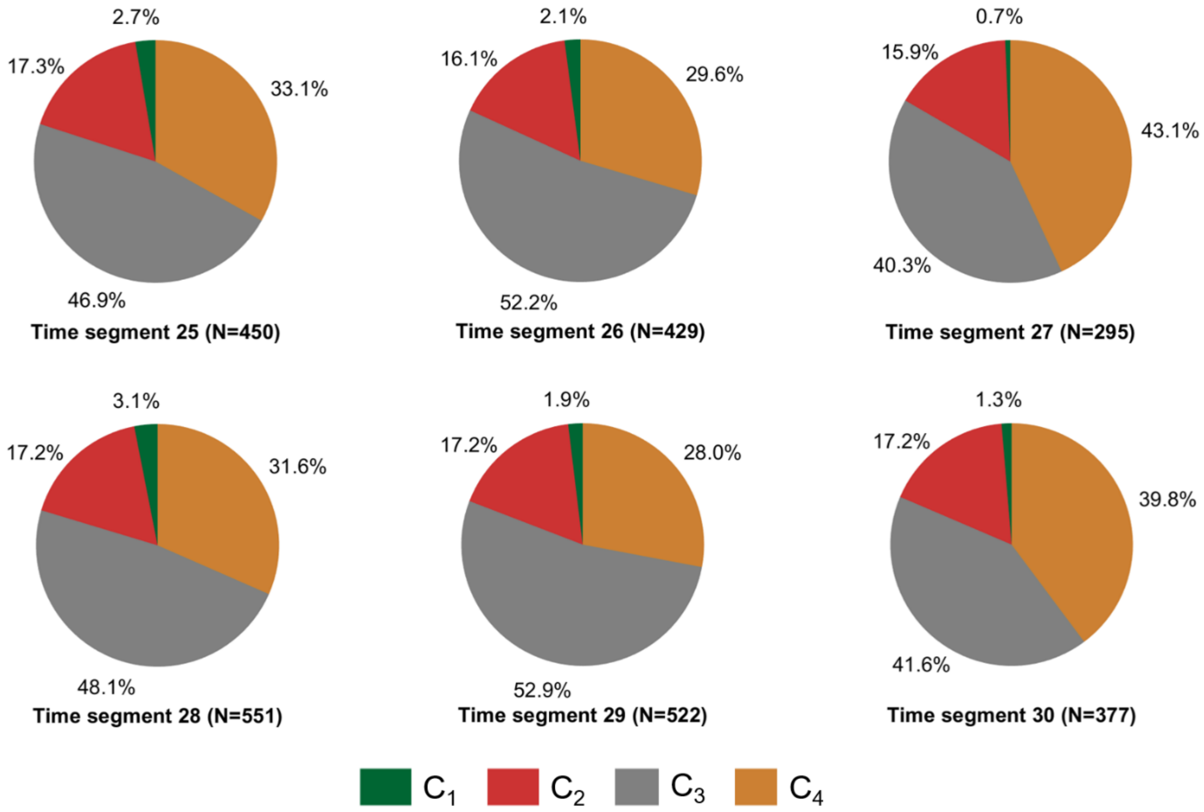

Figure 3.8. Temporal variation in CO_2RR selectivity. Pie charts showing for all 30 time segments the selectivities (%) of C_1–C_4 formation determined for the full ensemble of Ag NPs in CO_2RR under plasmonic excitation. The number of spectra resulting in each pie chart is listed as N. For this analysis, 68,000 SERS spectra acquired from 61 Ag NP scatterers were analyzed. Of this, 42,000 spectra obtained from 40 Ag NP scatterers are from source data acquired in a previous study.[S252]

3.5. TABLES

Table 3.1. Mean and standard deviation of the distributions in selectivities (%) of C_1–C_4 species measured across different Ag NP scatterers in the ensemble and across different time segments for the entire NP ensemble. 68, 000 spectra acquired from 61 Ag NP scatterers were analyzed. Of this, 42, 000 spectra obtained from 40 Ag NP scatterers are same as the source data analyzed in the previous manuscript.[252]

Category	**Mean (Standard deviation)**	
	Distribution across ensemble	Distribution across time
C_1	19% (25%)	3% (1%)
C_2	20% (10%)	22% (4%)
C_3	42% (17%)	48% (3%)
C_4	19% (10%)	27% (6%)

Table 3.2. DFT-computed Raman frequencies and normal mode analysis for 2,3-furandiol

Frequency, cm^{-1}	Major vibrational component (PED, %)
827	ϕ HCCC (76)
905	δ CCO (68)
1048	ν_{as}OC (-40)
1075	δ HOC (-17); δ COC (22)
1153	ν_{as}OC (-34)
1187	ν_{s}CC (27)
1264	δ HCO (34)
1302	δ HOC (-29)
1360	ν_{as}CC (-29)
1482	δ CCO (26)
1548	ν_{s}CC (68)
1705	ν_{s}CC (63)

Table 3.3. DFT-computed Raman frequencies and normal mode analysis for acetate

Frequency, cm^{-1}	Major vibrational component (PED, %)
862	ν_sCC (63)
994	ϕ HCCO (-66)
1029	ϕ HCCO (-53)
1319	δ HCH (85)
1345	ν_sOC (78)
1461	δ HCH (-76)
1475	δ HCH (79)
1648	ν_sOC (-93)

Table 3.4. DFT-computed Raman frequencies and normal mode analysis for pyruvate

Frequency, cm^{-1}	Major vibrational component (PED, %)
1006	ϕ HCCC (55)
1153	ϕ HCCC (28)
1322	ν_s OC (85)
1358	δ HCH (77)
1450	δ HCH (52)
1697	ν_s OC (94)
1755	ν_s OC (92)

Table 3.5. DFT-computed Raman frequencies and normal mode analysis for carbonate

Frequency, cm^{-1}	Major vibrational component (PED, %)
856	ϕ OCCC (100)
1010	ν_sOC (100)
1318	ν_sOC (-58)

Table 3.6. DFT-computed Raman frequencies and normal mode analysis for butene

Frequency, cm^{-1}	Major vibrational component (PED, %)
989	δ HCC (-56)
1019	ν_sCC (-53)
1030	ϕ HCCC (-62)
1093	ϕ HCCC (-22)
1198	δ HCC (-24)
1290	δ HCC (-41)
1319	δ HCC (63)
1344	ϕ HCCC (-60)
1408	δ HCH (95)
1453	δ HCH (73)
1483	δ HCH (-80)
1498	δ HCH (-72)
1506	δ HCH (-73)
1699	ν_sCC (70)

Table 3.7. DFT-computed Raman frequencies and normal mode analysis for glyceraldehyde

Frequency, cm^{-1}	Major vibrational component (PED, %)
907	ϕ HCCC (-40)
1035	ν_sCC (32)
1072	ν_sOC (70)
1086	ν_sOC (49)
1109	ν_sOC (15)
1199	ϕ HCCC (-39)
1219	δ HOC (-28)
1310	δ HCO (41)
1365	δ HCO (67)
1382	δ HCO (39)
1407	δ HOC (29)
1439	δ HCO (-29)
1506	δ HCH (91)
1793	ν_sOC (92)

Table 3.8. DFT-computed Raman frequencies and normal mode analysis for methyl glyoxal

Frequency, cm^{-1}	Major vibrational component (PED, %)
901	ϕ HCCO (-64)
1009	ϕ HCCC (-46)
1072	ϕ HCCC (22)
1238	ν_{as}CC (-47)
1355	δ HCO (92)
1392	δ HCH (45)
1460	δ HCH (-41)
1784	ν_{s} OC (90)
1801	ν_{s}OC (95)

Table 3.9. DFT-computed Raman frequencies and normal mode analysis for oxalate

Frequency, cm^{-1}	Major vibrational component (PED, %)
861	ϕ_{out} OCOC (100)
1289	ν_{s} OC (93)
1336	ν_{s} OC (87)
1577	ν_{s} OC (88)
1605	ν_{s} OC (98)

Table 3.10. DFT-computed Raman frequencies and normal mode analysis for formate

Frequency, cm^{-1}	Major vibrational component (PED, %)
1042	ϕ_{out} COOH (100)
1336	ν_{s} OC (89)
1375	δ HCO (94)
1660	ν_{s} OC (94)
2563	ν_{s} CH (99)

CHAPTER 4

OUTLOOK

As shown in the previous chapters, SERS is a powerful analytical tool for tracking the chemical activity of a catalyst in real time. As showed in my work, real-time responses from molecular species captured as vibrational signatures from the working environment of a catalyst can shed light into potential reaction intermediates formed on the surface. In-situ SERS monitoring of a Ag NP surface, under plasmonic excitation and CO_2RR conditions led to the discovery of a rich profile of multicarbon hydrocarbons, alcohols, and oxygenates. Here, a Ag NP plays a dual role: a photocatalyst that absorbs light and catalyzes the conversion of CO_2 to hydrocarbons and a plasmonic substrate that enhances the Raman signals of molecules in its close proximity, thereby enabling the probing of real-time chemical events by their vibrational signatures.

The capability of our nanoscale-SERS probing method is not limited to the tracking of chemical processes induced and/or enhanced by a plasmonic photocatalyst alone. I have performed an initial demonstration that a plasmonic Ag NP substrate can be used to study chemical transformations that are not plasmon-mediated. An example is the study of room-temperature, catalyst free chlorination of methane using trichloroisocyanuric acid (TCCA).[272] Here, TCCA acts as the chlorinating agent. The dissolution of TCCA in water releases hypochlorous acid (HOCl), the active chlorine species that triggers the chlorination of methane.

SERS probing of TCCA dissolved in water shows a vibrational peak corresponding to HOCl[273] around 731 cm^{-1} (Fig. 4.1). In a solution saturated with methane, this peak does not appear in the

SERS spectrum. This may be explained by the HOCl being consumed by the chlorination of methane and being unavailable to be detected at the Ag surface by SERS.

This powerful method can be utilized to study other non-plasmon-based catalysts and reactions by means of strategic design: for instance, a core-shell NP where the metal core is plasmonically active and serves as a spectroscopic enhancer and the shell catalyzes or hosts the reaction of interest. In this manner, the use of SERS for drawing molecular-level insights can be extended to a wider range of chemical reactions.

4.1. FIGURE

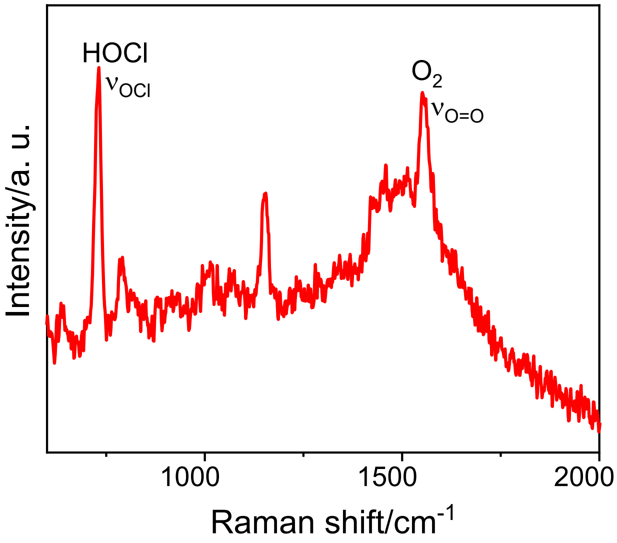

Figure 4.1. SERS spectrum of an aqueous solution of TCCA showing the vibrational signature of HOCl. A vibrational peak corresponding to HOCl[273] is observed around 731 cm^{-1}.

REFERENCES

1. Védrine, J. C. Heterogeneous catalysis on metal oxides. *Catalysts* **7**, 341 (2017).
2. Dumesic, J. A., Huber, G. W. & Boudart, M. Principles of heterogeneous catalysis. in *Handbook of heterogeneous catalysis* (Wiley-VCH, 2008).
3. Council, N. R., Sciences, D. E. P., Commission on Physical Sciences, M. A. & Technology, P. N. D. C. S. *Catalysis looks to the future*. (National Academies Press, 1992).
4. Moulijn, J. A., Leeuwen, P. W. N. M. van & Santen, R. A. van. *Catalysis: an integrated approach to homogeneous, heterogeneous and industrial catalysis*. (Elsevier, 1993).
5. Santen, R. A. van, Averill, B. A., Moulijn, J. A. & Leeuwen, P. W. N. M. van. *Catalysis: an integrated approach*. (Elsevier, 2000).
6. Bartholomew, C. H. & Farrauto, R. J. *Fundamentals of industrial catalytic processes*. (John Wiley & Sons, 2011).
7. Armor, J. N. New catalytic technology commercialized in the USA during the 1990s. *Appl. Catal. Gen.* **222**, 407–426 (2001).
8. Sorgenti, H. A. & Sachsel, G. F. Nitric acid manufacture—theory and practice. *Ind. Eng. Chem.* **52**, 101–104 (1960).
9. Salciccioli, M., Stamatakis, M., Caratzoulas, S. & Vlachos, D. G. A review of multiscale modeling of metal-catalyzed reactions: Mechanism development for complexity and emergent behavior. *Chem. Eng. Sci.* **66**, 4319–4355 (2011).
10. Buurmans, I. L. C. & Weckhuysen, B. M. Heterogeneities of individual catalyst particles in space and time as monitored by spectroscopy. *Nat. Chem.* **4**, 873–886 (2012).
11. Sambur, J. B. & Chen, P. Approaches to single-nanoparticle catalysis. *Annu. Rev. Phys. Chem.* **65**, 395–422 (2014).

12. Chen, P. *et al.* Single-molecule fluorescence imaging of nanocatalytic processes. *Chem. Soc. Rev.* **39**, 4560–4570 (2010).
13. Tachikawa, T. & Majima, T. Single-molecule, single-particle fluorescence imaging of TiO_2-based photocatalytic reactions. *Chem. Soc. Rev.* **39**, 4802–4819 (2010).
14. Cremer, G. D., F. Sels, B., Vos, D. E. D., Hofkens, J. & J. Roeffaers, M. B. Fluorescence micro(spectro)scopy as a tool to study catalytic materials in action. *Chem. Soc. Rev.* **39**, 4703–4717 (2010).
15. Hirschfeld, T. Optical microscopic observation of single small molecules. *Appl. Opt.* **15**, 2965 (1976).
16. Brooks Shera, E., Seitzinger, N. K., Davis, L. M., Keller, R. A. & Soper, S. A. Detection of single fluorescent molecules. *Chem. Phys. Lett.* **174**, 553–557 (1990).
17. Moerner, W. E. & Kador, L. Optical detection and spectroscopy of single molecules in a solid. *Phys. Rev. Lett.* **62**, 2535–2538 (1989).
18. Orrit, M. & Bernard, J. Single pentacene molecules detected by fluorescence excitation in a p-terphenyl crystal. *Phys. Rev. Lett.* **65**, 2716–2719 (1990).
19. Betzig, E. & Chichester, R. J. Single molecules observed by near-field scanning optical microscopy. *Science* **262**, 1422–1425 (1993).
20. Lu, H. P., Xun, L. & Xie, X. S. Single-molecule enzymatic dynamics. *Science* **282**, 1877–1882 (1998).
21. Edman, L., Földes-Papp, Z., Wennmalm, S. & Rigler, R. The fluctuating enzyme: a single molecule approach. *Chem. Phys.* **247**, 11–22 (1999).
22. Velonia, K. *et al.* Single-enzyme kinetics of CALB-catalyzed hydrolysis. *Angew. Chem. Int. Ed Engl.* **44**, 560–564 (2005).

23. English, B. P. *et al.* Ever-fluctuating single enzyme molecules: Michaelis-Menten equation revisited. *Nat. Chem. Biol.* **2**, 87–94 (2006).

24. Smiley, R. D. & Hammes, G. G. Single molecule studies of enzyme mechanisms. *Chem. Rev.* **106**, 3080–3094 (2006).

25. Xu, W., Kong, J. S., Yeh, Y.-T. E. & Chen, P. Single-molecule nanocatalysis reveals heterogeneous reaction pathways and catalytic dynamics. *Nat. Mater.* **7**, 992 (2008).

26. Roeffaers, M. B. J. *et al.* Spatially resolved observation of crystal-face-dependent catalysis by single turnover counting. *Nature* **439**, 572–575 (2006).

27. Naito, K., Tachikawa, T., Fujitsuka, M. & Majima, T. Real-time single-molecule imaging of the spatial and temporal distribution of reactive oxygen species with fluorescent probes: applications to TiO_2 photocatalysts. *J. Phys. Chem. C* **112**, 1048–1059 (2008).

28. Routzahn, A. L. & Jain, P. K. Luminescence blinking of a reacting quantum dot. *Nano Lett.* **15**, 2504–2509 (2015).

29. Routzahn, A. L. & Jain, P. K. Single-nanocrystal reaction trajectories reveal sharp cooperative transitions. *Nano Lett.* **14**, 987–992 (2014).

30. Sharma, B., Frontiera, R. R., Henry, A.-I., Ringe, E. & Van Duyne, R. P. SERS: materials, applications, and the future. *Mater. Today* **15**, 16–25 (2012).

31. Fleischmann, M., Hendra, P. J. & McQuillan, A. J. Raman spectra of pyridine adsorbed at a silver electrode. *Chem. Phys. Lett.* **26**, 163–166 (1974).

32. Jeanmaire, D. L. & Van Duyne, R. P. Surface raman spectroelectrochemistry: Part I. Heterocyclic, aromatic, and aliphatic amines adsorbed on the anodized silver electrode. *J. Electroanal. Chem. Interfacial Electrochem.* **84**, 1–20 (1977).

33. Schatz, G. C., Young, M. A. & Van Duyne, R. P. Electromagnetic mechanism of SERS. in *Surface-enhanced Raman scattering: physics and applications* (eds. Kneipp, K., Moskovits, M. & Kneipp, H.) 19–45 (Springer Berlin Heidelberg, 2006).

34. Otto, A. The 'chemical' (electronic) contribution to surface-enhanced Raman scattering. *J. Raman Spectrosc.* **36**, 497–509 (2005).

35. Jensen, L., M. Aikens, C. & C. Schatz, G. Electronic structure methods for studying surface-enhanced Raman scattering. *Chem. Soc. Rev.* **37**, 1061–1073 (2008).

36. Lombardi, J. R. & Birke, R. L. A unified approach to surface-enhanced Raman spectroscopy. *J. Phys. Chem. C* **112**, 5605–5617 (2008).

37. Nie, S. & Emory, S. R. Probing single molecules and single nanoparticles by surface-enhanced raman scattering. *Science* **275**, 1102–1106 (1997).

38. Xu, P. *et al.* Mechanistic understanding of surface plasmon assisted catalysis on a single particle: cyclic redox of 4-aminothiophenol. *Sci. Rep.* **3**, 2997 (2013).

39. Kang, L. *et al.* In situ surface-enhanced Raman spectroscopy study of plasmon-driven catalytic reactions of 4-nitrothiophenol under a controlled atmosphere. *ChemCatChem* **7**, 1004–1010 (2015).

40. Tang, X., Cai, W., Yang, L. & Liu, J. Monitoring plasmon-driven surface catalyzed reactions in situ using time-dependent surface-enhanced Raman spectroscopy on single particles of hierarchical peony-like silver microflowers. *Nanoscale* **6**, 8612–8616 (2014).

41. Wang, H. *et al.* Plasmon-driven surface catalysis in hybridized plasmonic gap modes. *Sci. Rep.* **4**, 7087 (2014).

42. Sun, M., Hou, Y., Li, Z., Liu, L. & Xu, H. Remote excitation polarization-dependent surface photochemical reaction by plasmonic waveguide. *Plasmonics* **6**, 681 (2011).

43. Shen, Y. *et al.* SERS-based plasmon-driven reaction and molecule detection on a single Ag@MoS_2 microsphere: effect of thickness and crystallinity of MoS_2. *ChemCatChem* **10**, 3520–3525 (2018).

44. Kang, L. *et al.* Laser wavelength- and power-dependent plasmon-driven chemical reactions monitored using single particle surface enhanced Raman spectroscopy. *Chem. Commun.* **49**, 3389–3391 (2013).

45. Kumari, G., Zhang, X., Devasia, D., Heo, J. & Jain, P. K. Watching visible light-driven CO_2 reduction on a plasmonic nanoparticle catalyst. *ACS Nano* **12**, 8330–8340 (2018).

46. Kneipp, K. *et al.* Single molecule detection using surface-enhanced Raman scattering (SERS). *Phys. Rev. Lett.* **78**, 1667–1670 (1997).

47. Michaels, A. M., Nirmal, M. & Brus, L. E. Surface enhanced raman spectroscopy of individual rhodamine 6G molecules on large Ag nanocrystals. *J. Am. Chem. Soc.* **121**, 9932–9939 (1999).

48. Dieringer, J. A., Lettan, R. B., Scheidt, K. A. & Van Duyne, R. P. A Frequency Domain Existence Proof of Single-Molecule Surface-Enhanced Raman Spectroscopy. *J. Am. Chem. Soc.* **129**, 16249–16256 (2007).

49. Kleinman, S. L. *et al.* Single-molecule surface-enhanced Raman spectroscopy of crystal violet isotopologues: theory and experiment. *J. Am. Chem. Soc.* **133**, 4115–4122 (2011).

50. Zong, C. *et al.* Single-molecule level rare events revealed by dynamic surface-enhanced raman spectroscopy. *Anal. Chem.* **92**, 15806–15810 (2020).

51. Michaels, A. M., Jiang & Brus, L. Ag nanocrystal junctions as the site for surface-enhanced Raman scattering of single rhodamine 6G molecules. *J. Phys. Chem. B* **104**, 11965–11971 (2000).

52. Kang, L. *et al.* Amino acid-assisted synthesis of hierarchical silver microspheres for single particle surface-enhanced raman spectroscopy. *J. Phys. Chem. C* **117**, 10007–10012 (2013).
53. van Schrojenstein Lantman, E. M., Deckert-Gaudig, T., Mank, A. J. G., Deckert, V. & Weckhuysen, B. M. Catalytic processes monitored at the nanoscale with tip-enhanced Raman spectroscopy. *Nat. Nanotechnol.* **7**, 583–586 (2012).
54. Williams, C. T., Takoudis, C. G. & Weaver, M. J. Methanol oxidation on rhodium as probed by surface-enhanced Raman and mass spectroscopies: adsorbate stability, reactivity, and catalytic relevance. *J. Phys. Chem. B* **102**, 406–416 (1998).
55. Chan, H. Y. H., Williams, C. T., Weaver, M. J. & Takoudis, C. G. Methanol oxidation on palladium compared to rhodium at ambient pressures as probed by surface-enhanced Raman and mass spectroscopies. *J. Catal.* **174**, 191–200 (1998).
56. Zou, S., Chan, H. Y. H., Williams, C. T. & Weaver, M. J. Formation and stability of oxide films on platinum-group metals in electrochemical and related environments as probed by surface-enhanced Raman spectroscopy: dependence on the chemical oxidant. *Langmuir* **16**, 754–763 (2000).
57. Bhasin, M. M. Importance of surface science and fundamental studies in heterogeneous catalysis. *Catal. Lett.* **59**, 1–7 (1999).
58. Shan, X. *et al.* Imaging the electrocatalytic activity of single nanoparticles. *Nat. Nanotechnol.* **7**, 668–672 (2012).
59. Wang, W. Imaging the chemical activity of single nanoparticles with optical microscopy. *Chem. Soc. Rev.* **47**, 2485–2508 (2018).
60. Fang, Y. *et al.* Plasmonic imaging of electrochemical oxidation of single nanoparticles. *J. Am. Chem. Soc.* **136**, 12584–12587 (2014).

61. Fang, Y. *et al.* Plasmonic imaging of electrochemical reactions of single nanoparticles. *Acc. Chem. Res.* **49**, 2614–2624 (2016).

62. Zhou, X., Xu, W., Liu, G., Panda, D. & Chen, P. Size-dependent catalytic activity and dynamics of gold nanoparticles at the single-molecule level. *J. Am. Chem. Soc.* **132**, 138–146 (2010).

63. Zhou, X. *et al.* Quantitative super-resolution imaging uncovers reactivity patterns on single nanocatalysts. *Nat. Nanotechnol.* **7**, 237–241 (2012).

64. Smith, J. G., Yang, Q. & Jain, P. K. Identification of a critical intermediate in galvanic exchange reactions by single-nanoparticle-resolved kinetics. *Angew. Chem.* **126**, 2911–2916 (2014).

65. Smith, J. G. & Jain, P. K. The ligand shell as an energy barrier in surface reactions on transition metal nanoparticles. *J. Am. Chem. Soc.* **138**, 6765–6773 (2016).

66. Smith, J. G., Chakraborty, I. & Jain, P. K. In situ single-nanoparticle spectroscopy study of bimetallic nanostructure formation. *Angew. Chem. Int. Ed.* **55**, 9979–9983 (2016).

67. Smith, J. G. & Jain, P. K. Kinetics of self-assembled monolayer formation on individual nanoparticles. *Phys. Chem. Chem. Phys.* **18**, 23990–23997 (2016).

68. Smith, J. G., Zhang, X. & Jain, P. K. Galvanic reactions at the single-nanoparticle level: tuning between mechanistic extremes. *J. Mater. Chem. A* **5**, 11940–11948 (2017).

69. Lewis, N. S. & Nocera, D. G. Powering the planet: chemical challenges in solar energy utilization. *Proc. Natl. Acad. Sci.* **103**, 15729–15735 (2006).

70. Corbin, N., Zeng, J., Williams, K. & Manthiram, K. Heterogeneous molecular catalysts for electrocatalytic CO_2 reduction. *Nano Res.* **12**, 2093–2125 (2019).

71. Yang, D.-T. *et al.* Direct electrochemical carboxylation of benzylic C–N bonds with carbon dioxide. *ACS Catal.* **9**, 4699–4705 (2019).

72. Martell, S. A. *et al.* High surface area mesoporous silicon nanoparticles prepared via two-step magnesiothermic reduction for stoichiometric CO_2 to CH_3OH conversion. *ACS Appl. Nano Mater.* **2**, 5713–5719 (2019).

73. Dasog, M., Kraus, S., Sinelnikov, R., C. Veinot, J. G. & Rieger, B. CO_2 to methanol conversion using hydride terminated porous silicon nanoparticles. *Chem. Commun.* **53**, 3114–3117 (2017).

74. Olivo, A. *et al.* CO_2 photoreduction with water: catalyst and process investigation. *J. CO2 Util.* **12**, 86–94 (2015).

75. Appel, A. M. *et al.* Frontiers, opportunities, and challenges in biochemical and chemical catalysis of CO_2 fixation. *Chem. Rev.* **113**, 6621–6658 (2013).

76. Qiao, J., Liu, Y., Hong, F. & Zhang, J. A review of catalysts for the electroreduction of carbon dioxide to produce low-carbon fuels. *Chem. Soc. Rev.* **43**, 631–675 (2013).

77. Lu, Q. *et al.* A selective and efficient electrocatalyst for carbon dioxide reduction. *Nat. Commun.* **5**, 3242 (2014).

78. Govorov, A. O., Zhang, H. & Gun'ko, Y. K. Theory of photoinjection of hot plasmonic carriers from metal nanostructures into semiconductors and surface molecules. *J. Phys. Chem. C* **117**, 16616–16631 (2013).

79. Aizpurua, J. *et al.* Theory of hot electrons: general discussion. *Faraday Discuss.* **214**, 245–281 (2019).

80. Govorov, A. O., Zhang, H., Demir, H. V. & Gun'ko, Y. K. Photogeneration of hot plasmonic electrons with metal nanocrystals: quantum description and potential applications. *Nano Today* **9**, 85–101 (2014).

81. Harutyunyan, H. *et al.* Anomalous ultrafast dynamics of hot plasmonic electrons in nanostructures with hot spots. *Nat. Nanotechnol.* **10**, 770–774 (2015).

82. Kim, Y., Smith, J. G. & Jain, P. K. Harvesting multiple electron–hole pairs generated through plasmonic excitation of au nanoparticles. *Nat. Chem.* **10**, 763–769 (2018).

83. Yu, S., Wilson, A. J., Kumari, G., Zhang, X. & Jain, P. K. Opportunities and challenges of solar-energy-driven carbon dioxide to fuel conversion with plasmonic catalysts. *ACS Energy Lett.* **2**, 2058–2070 (2017).

84. Yu, S., Wilson, A. J., Heo, J. & Jain, P. K. Plasmonic control of multi-electron transfer and C-C coupling in visible-light-driven CO_2 reduction on au nanoparticles. *Nano Lett.* **18**, 2189–2194 (2018).

85. Yu, S. & Jain, P. K. Plasmonic photosynthesis of C_1–C_3 hydrocarbons from carbon dioxide assisted by an ionic liquid. *Nat. Commun.* **10**, 1–7 (2019).

86. Yu, S. & Jain, P. K. Selective branching of plasmonic photosynthesis into hydrocarbon production and hydrogen generation. *ACS Energy Lett.* **4**, 2295–2300 (2019).

87. Naldoni, A., Shalaev, V. M. & Brongersma, M. L. Applying plasmonics to a sustainable future. *Science* **356**, 908–909 (2017).

88. Naldoni, A. *et al.* Solar-powered plasmon-enhanced heterogeneous catalysis. *Nanophotonics* **5**, 112–133 (2016).

89. Wu, S. & Sheldon, M. T. Optical power conversion via tunneling of plasmonic hot carriers. *ACS Photonics* **5**, 2516–2523 (2018).

90. Hogan, N., Wu, S. & Sheldon, M. Photothermalization and hot electron dynamics in the steady state. *J. Phys. Chem. C* **124**, 4931–4945 (2020).

91. Sheldon, M. T., Groep, J. van de, Brown, A. M., Polman, A. & Atwater, H. A. Plasmoelectric potentials in metal nanostructures. *Science* **346**, 828–831 (2014).

92. Drachev, V. P. *et al.* Adaptive silver films for surface-enhanced raman spectroscopy of biomolecules. *J. Raman Spectrosc.* **36**, 648–656 (2005).

93. Zhang, Z., Deckert-Gaudig, T. & Deckert, V. Label-free monitoring of plasmonic catalysis on the nanoscale. *Analyst* **140**, 4325–4335 (2015).

94. Jeanmaire, D. & Vanduyne, R. Surface Raman spectroelectrochemistry .1. heterocyclic, aromatic, and aliphatic-amines adsorbed on anodized silver electrode. *J. Electroanal. Chem.* **84**, 1–20 (1977).

95. Fokas, C. & Deckert, V. Towards in situ Raman microscopy of single catalytic sites. *Appl. Spectrosc.* **56**, 192–199 (2002).

96. Tabatabaei, M. *et al.* Tunable 3D plasmonic cavity nanosensors for surface-enhanced Raman spectroscopy with sub-femtomolar limit of detection. *ACS Photonics* **2**, 752–759 (2015).

97. Galarreta, B. C., Tabatabaei, M., Guieu, V., Peyrin, E. & Lagugné-Labarthet, F. Microfluidic channel with embedded SERS 2D platform for the aptamer detection of ochratoxin a. *Anal. Bioanal. Chem.* **405**, 1613–1621 (2013).

98. McRae, D. M. & Lagugné-Labarthet, F. In search of the hot spot. *Nat. Nanotechnol.* **14**, 922–923 (2019).

99. Merlen, A., Lagugné-Labarthet, F. & Harté, E. Surface-enhanced Raman and fluorescence spectroscopy of dye molecules deposited on nanostructured gold surfaces. *J. Phys. Chem. C* **114**, 12878–12884 (2010).

100. McNay, G., Eustace, D., Smith, W. E., Faulds, K. & Graham, D. Surface-enhanced Raman scattering (SERS) and surface-enhanced resonance Raman scattering (SERRS): a review of applications. *Appl. Spectrosc.* **65**, 825–837 (2011).

101. Haran, G. Single-molecule Raman spectroscopy: a probe of surface dynamics and plasmonic fields. *Acc. Chem. Res.* **43**, 1135–1143 (2010).

102. Wilson, A. J. & Jain, P. K. Structural dynamics of the oxygen-evolving complex of photosystem ii in water-splitting action. *J. Am. Chem. Soc.* **140**, 5853–5859 (2018).

103. Zhang, X., Kumari, G., Heo, J. & Jain, P. K. In situ formation of catalytically active graphene in ethylene photo-epoxidation. *Nat. Commun.* **9**, 1–10 (2018).

104. Qian, X.-M. & Nie, S. M. Single-molecule and single-nanoparticle SERS: from fundamental mechanisms to biomedical applications. *Chem. Soc. Rev.* **37**, 912–920 (2008).

105. Lee, P. C. & Meisel, D. Adsorption and surface-enhanced Raman of dyes on silver and gold sols. *J. Phys. Chem.* **86**, 3391–3395 (1982).

106. Joshi, G. K., White, S. L., Johnson, M. A., Sardar, R. & Jain, P. K. Ultrashort, angstrom-scale decay of surface-enhanced raman scattering at hot spots. *J. Phys. Chem. C* **120**, 24973–24981 (2016).

107. Masango, S. S. *et al.* High-resolution distance dependence study of surface-enhanced Raman scattering enabled by atomic layer deposition. *Nano Lett.* **16**, 4251–4259 (2016).

108. Spurgeon, J. M. & Kumar, B. A comparative technoeconomic analysis of pathways for commercial electrochemical CO_2 reduction to liquid products. *Energy Env. Sci* **11**, 1536–1551 (2018).

109. Zhao, K., Liu, Y., Quan, X., Chen, S. & Yu, H. CO_2 electroreduction at low overpotentia electroreduction at low overpotential on oxide-derived Cu/carbons fabricated from metal organic framework. *ACS Appl. Mater. Interfaces* **9**, 5302–5311 (2017).

110. Kwon, Y., Lum, Y., Clark, E. L., Ager, J. W. & Bell, A. T. CO_2 electroreduction with enhanced ethylene and ethanol selectivity by nanostructuring polycrystalline copper. *ChemElectroChem* **3**, 1012–1019 (2016).

111. Hori, Y., Wakebe, H., Tsukamoto, T. & Koga, O. Electrocatalytic process of co selectivity in electrochemical reduction of co_2 at metal electrodes in aqueous media. *Electrochimica Acta* **39**, 1833–1839 (1994).

112. Kas, R., Kortlever, R., Yılmaz, H., Koper, M. T. M. & Mul, G. Manipulating the hydrocarbon selectivity of copper nanoparticles in CO_2 electroreduction by process conditions. *ChemElectroChem* **2**, 354–358 (2015).

113. Ren, D., Wong, N. T., Handoko, A. D., Huang, Y. & Yeo, B. S. Mechanistic insights into the enhanced activity and stability of agglomerated Cu nanocrystals for the electrochemical reduction of carbon dioxide to n-propanol. *J. Phys. Chem. Lett.* **7**, 20–24 (2016).

114. Dutta, A., Rahaman, M., Luedi, N. C., Mohos, M. & Broekmann, P. Morphology matters: tuning the product distribution of CO_2 electroreduction on oxide-derived Cu foam catalysts. *ACS Catal.* **6**, 3804–3814 (2016).

115. Hori, Y., Kikuchi, K., Murata, A. & Suzuki, S. Production of methane and ethylene in electrochemical reduction of carbon dioxide at copper electrode in aqueous hydrogen carbonate solution. *Chem. Lett.* **15**, 897–898 (1986).

116. Calvinho, K. U. D. *et al.* Selective CO_2 reduction to C_3 and C_4 oxyhydrocarbons on nickel phosphides at overpotentials as low as 10 mv. *Energy Env. Sci* **11**, 2550–2559 (2018).

117. Ren, D. *et al.* Selective electrochemical reduction of carbon dioxide to ethylene and ethanol on copper(i) oxide catalysts. *ACS Catal.* **5**, 2814–2821 (2015).

118. Chen, C. S. *et al.* Stable and selective electrochemical reduction of carbon dioxide to ethylene on copper mesocrystals. *Catal. Sci. Technol.* **5**, 161–168 (2015).

119. Li, Y. *et al.* Structure-sensitive CO_2 electroreduction to hydrocarbons on ultrathin 5-fold twinned copper nanowires. *Nano Lett.* **17**, 1312–1317 (2017).

120. Hori, Y., Murata, A. & Takahashi, R. Formation of hydrocarbons in the electrochemical reduction of carbon dioxide at a copper electrode in aqueous solution. *J Chem Soc Faraday Trans 1* **85**, 2309–2326 (1989).

121. Chen, C. S., Wan, J. H. & Yeo, B. S. Electrochemical reduction of carbon dioxide to ethane using nanostructured Cu_2o-derived copper catalyst and palladium(ii) chloride. *J. Phys. Chem. C* **119**, 26875–26882 (2015).

122. Schmitt, K. G. & Gewirth, A. A. In situ surface-enhanced Raman spectroscopy of the electrochemical reduction of carbon dioxide on silver with 3,5-diamino-1,2,4-triazole. *J. Phys. Chem. C* **118**, 17567–17576 (2014).

123. Ichinohe, Y., Wadayama, T. & Hatta, A. Electrochemical reduction of CO_2 on silver as probed by surface-enhanced raman scattering. *J. Raman Spectrosc.* **26**, 335–340 (1995).

124. Hatsukade, T., Kuhl, K. P., Cave, E. R., Abram, D. N. & Jaramillo, T. F. Insights into the electrocatalytic reduction of CO_2 on metallic silver surfaces. *Phys. Chem. Chem. Phys.* **16**, 13814–13819 (2014).

125. Ye, Y. *et al.* Dramatic differences in carbon dioxide adsorption and initial steps of reduction between silver and copper. *Nat. Commun.* **10**, 1875 (2019).

126. Zhang, D., Xie, Y., Deb, S. K., Davison, V. J. & Ben-Amotz, D. Isotope edited internal standard method for quantitative surface-enhanced Raman spectroscopy. *Anal. Chem.* **77**, 3563–3569 (2005).

127. Deb, S. K. *et al.* Detection and relative quantification of proteins by surface enhanced Raman using isotopic labels. *J. Am. Chem. Soc.* **130**, 9624–9625 (2008).

128. Kim, C. *et al.* Achieving selective and efficient electrocatalytic activity for CO_2 reduction using immobilized silver nanoparticles. *J. Am. Chem. Soc.* **137**, 13844–13850 (2015).

129. Kostecki, R. & Augustynski, J. Electrochemical reduction of CO_2 at an activated silver electrode. *Berichte Bunsenges. Für Phys. Chem.* **98**, 1510–1515 (1994).

130. Zhao, S., Jin, R. & Jin, R. Opportunities and challenges in CO_2 reduction by gold- and silver-based electrocatalysts: from bulk metals to nanoparticles and atomically precise nanoclusters. *ACS Energy Lett.* **3**, 452–462 (2018).

131. Hoshi, N., Kato, M. & Hori, Y. Electrochemical reduction of CO_2 on single crystal electrodes of silver Ag(111), Ag(100) and Ag(110). *J. Electroanal. Chem.* **440**, 283–286 (1997).

132. Noda, H. *et al.* Electrochemical reduction of carbon dioxide at various metal electrodes in aqueous potassium hydrogen carbonate solution. *Bull. Chem. Soc. Jpn.* **63**, 2459–2462 (1990).

133. Dutta, A., Morstein, C. E., Rahaman, M., Cedeño López, A. & Broekmann, P. Beyond copper in CO_2 electrolysis: effective hydrocarbon production on silver-nanofoam catalysts. *ACS Catal.* **8**, 8357–8368 (2018).

134. Azuma, M., Hashimoto, K., Hiramoto, M., Watanabe, M. & Sakata, T. Electrochemical reduction of carbon dioxide on various metal electrodes in low-temperature aqueous $khco_3$ media. *J. Electrochem. Soc.* **137**, 1772–1778 (1990).

135. Lee, S., Kim, D. & Lee, J. Electrocatalytic production of C_3-C_4 compounds by conversion of CO_2 on a chloride-induced bi-phasic Cu_2o-Cu catalyst. *Angew. Chem. Int. Ed.* **54**, 14701–14705 (2015).

136. Kim, D., Kley, C. S., Li, Y. & Yang, P. Copper nanoparticle ensembles for selective electroreduction of CO_2 to C_2– C_3 products. *Proc. Natl. Acad. Sci.* **114**, 10560–10565 (2017).

137. Zhuang, T.-T. *et al.* Copper nanocavities confine intermediates for efficient electrosynthesis of C_3 alcohol fuels from carbon monoxide. *Nat. Catal.* **1**, 946–951 (2018).

138. Ebaid, M. *et al.* Production of C_2/C_3 oxygenates from planar copper nitride-derived mesoporous copper via electrochemical reduction of CO_2. *Chem. Mater.* **32**, 3304–3311 (2020).

139. Kim, T. *et al.* Enhancing C_2–C_3 production from CO_2 on copper electrocatalysts via a potential-dependent mesostructure. *ACS Appl. Energy Mater.* **1**, 1965–1972 (2018).

140. Wang, X. *et al.* Efficient upgrading of CO to C_3 fuel using asymmetric C-C coupling active sites. *Nat. Commun.* **10**, 5186 (2019).

141. Zhuang, T.-T. *et al.* Steering post-C–C coupling selectivity enables high efficiency electroreduction of carbon dioxide to multi-carbon alcohols. *Nat. Catal.* **1**, 421–428 (2018).

142. Kuhl, K. P., Cave, E. R., Abram, D. N. & Jaramillo, T. F. New insights into the electrochemical reduction of carbon dioxide on metallic copper surfaces. *Energy Environ. Sci.* **5**, 7050–7059 (2012).

143. Wang, X. *et al.* Mechanistic reaction pathways of enhanced ethylene yields during electroreduction of CO_2–co CO-feeds on Cu and Cu-tandem electrocatalysts. *Nat. Nanotechnol.* **14**, 1063–1070 (2019).

144. Han, Z., Kortlever, R., Chen, H.-Y., Peters, J. C. & Agapie, T. CO_2 reduction selective for $C\geq2$ products on polycrystalline copper with n-substituted pyridinium additives. *ACS Cent. Sci.* **3**, 853–859 (2017).

145. Baturina, O. A. *et al.* CO_2 electroreduction to hydrocarbons on carbon-supported Cu nanoparticles. *ACS Catal.* **4**, 3682–3695 (2014).

146. Manthiram, K., Beberwyck, B. J. & Alivisatos, A. P. Enhanced electrochemical methanation of carbon dioxide with a dispersible nanoscale copper catalyst. *J. Am. Chem. Soc.* **136**, 13319–13325 (2014).

147. Gao, J., Ren, D., Guo, X., Zakeeruddin, S. M. & Grätzel, M. Sequential catalysis enables enhanced C–C coupling towards multi-carbon alkenes and alcohols in carbon dioxide reduction: a study on bifunctional Cu/Au electrocatalysts. *Faraday Discuss.* **215**, 282–296 (2019).

148. Paris, A. R. & Bocarsly, A. B. Ni–Al films on glassy carbon electrodes generate an array of oxygenated organics from CO_2. *ACS Catal.* **7**, 6815–6820 (2017).

149. Paris, A. R. & Bocarsly, A. B. Mechanistic insights into C_2 and C_3 product generation using Ni_3Al and Ni_3Ga electrocatalysts for CO_2 reduction. *Faraday Discuss.* **215**, 192–204 (2019).

150. Kortlever, R. *et al.* Palladium–gold catalyst for the electrochemical reduction of CO_2 to C_1–C_5 hydrocarbons. *Chem. Commun.* **52**, 10229–10232 (2016).

151. Sorcar, S. *et al.* High-rate solar-light photoconversion of CO_2 to fuel: controllable transformation from C_1 to C_2 products. *Energy Environ. Sci.* **11**, 3183–3193 (2018).

152. Wu, J. *et al.* A metal-free electrocatalyst for carbon dioxide reduction to multi-carbon hydrocarbons and oxygenates. *Nat. Commun.* **7**, 13869 (2016).

153. Pérez-Cadenas, A. F. *et al.* Metal-doped carbon xerogels for the electro-catalytic conversion of CO_2 to hydrocarbons. *Carbon* **56**, 324–331 (2013).

154. Hara, K., Kudo, A. & Sakata, T. Electrochemical CO_2 reduction on a glassy carbon electrode under high pressure. *J. Electroanal. Chem.* **421**, 1–4 (1997).

155. Hara, K., Kudo, A. & Sakata, T. Electrochemical reduction of high pressure carbon dioxide on fe electrodes at large current density. *J. Electroanal. Chem.* **386**, 257–260 (1995).

156. Castelo-Quibén, J. *et al.* Carbon-iron electro-catalysts for CO_2 reduction. the role of the iron particle size. *J. CO2 Util.* **24**, 240–249 (2018).

157. Gao, D., Arán-Ais, R. M., Jeon, H. S. & Roldan Cuenya, B. Rational catalyst and electrolyte design for CO_2 electroreduction towards multicarbon products. *Nat. Catal.* **2**, 198–210 (2019).

158. Greenblatt, J. B., Miller, D. J., Ager, J. W., Houle, F. A. & Sharp, I. D. The technical and energetic challenges of separating (photo)electrochemical carbon dioxide reduction products. *Joule* **2**, 381–420 (2018).

159. Li, H. *et al.* Integrated electromicrobial conversion of CO_2 to higher alcohols. *Science* **335**, 1596–1596 (2012).

160. Link, S. & El-Sayed, M. A. Spectral properties and relaxation dynamics of surface plasmon electronic oscillations in gold and silver nanodots and nanorods. *J. Phys. Chem. B* **103**, 8410–8426 (1999).

161. Zhang, H. *et al.* In situ dynamic tracking of heterogeneous nanocatalytic processes by shell-isolated nanoparticle-enhanced raman spectroscopy. *Nat. Commun.* **8**, 15447 (2017).

162. M. J. Frisch, G. W. Trucks, H. B. Schlegel, G. E. Scuseria, M. A. Robb, J. R. Cheeseman, G. Scalmani, V. Barone, G. A. Petersson, H. Nakatsuji, X. Li, M. Caricato, A. Marenich, J.

Bloino, B. G. Janesko, R. Gomperts, B. Mennucci, H. P. Hratchian, J. V. Ortiz, A. F. Izmaylov, J. L. Sonnenberg, D. Williams-Young, F. Ding, F. Lipparini, F. Egidi, J. Goings, B. Peng, A. Petrone, T. Henderson, D. Ranasinghe, V. G. Zakrzewski, J. Gao, N. Rega, G. Zheng, W. Liang, M. Hada, M. Ehara, K. Toyota, R. Fukuda, J. Hasegawa, M. Ishida, T. Nakajima, Y. Honda, O. Kitao, H. Nakai, T. Vreven, K. Throssell, J. A. Montgomery, Jr., J. E. Peralta, F. Ogliaro, M. Bearpark, J. J. Heyd, E. Brothers, K. N. Kudin, V. N. Staroverov, T. Keith, R. Kobayashi, J. Normand, K. Raghavachari, A. Rendell, J. C. Burant, S. S. Iyengar, J. Tomasi, M. Cossi, J. M. Millam, M. Klene, C. Adamo, R. Cammi, J. W. Ochterski, R. L. Martin, K. Morokuma, O. Farkas, J. B. Foresman, and D. J. Fox. *Gaussian 09*. (Gaussian, Inc., Wallingford CT, 2016).

163. Jamróz, M. H. Vibrational Energy Distribution Analysis (VEDA): scopes and limitations. *Spectrochim. Acta. A. Mol. Biomol. Spectrosc.* **114**, 220–230 (2013).
164. Michal. H. Jamroz. *Vibrational Energy Distribution Analysis VEDA 4*. (Warsaw, 2004-2010).
165. Dijk, M. A. van & Natuurwetenschappen, F. der W. en. Nonlinear optical studies of single gold nanoparticles. (Leiden University, 2007).
166. Simakov, D. S. A. Thermocatalytic conversion of CO_2. in *Renewable synthetic fuels and chemicals from carbon dioxide: fundamentals, catalysis, design considerations and technological challenges* (ed. Simakov, D. S. A.) 1–25 (Springer International Publishing, 2017).
167. N. Waterhouse, G. I., A. Bowmaker, G. & B. Metson, J. The thermal decomposition of silver (i, iii) oxide: a combined XRD, FT-IR and Raman spectroscopic study. *Phys. Chem. Chem. Phys.* **3**, 3838–3845 (2001).

168. Martina, I. Micro-Raman characterisation of silver corrosion products: instrumental set up and reference database. 8 (2012).

169. Giguére, P. A. & Srinivasan, T. K. K. A Raman study of H_2O_2 and D_2O_2 vapor. *J. Raman Spectrosc.* **2**, 125–132 (1974).

170. Ricks, A. M., Douberly, G. E. & Duncan, M. A. IR photodissociation spectroscopy of O_{4+}, O_{6+} and O_{8+} cluster ions. *Int. J. Mass Spectrom.* **283**, 69–76 (2009).

171. Green, I. X. & Yates, J. T. Vibrational spectroscopic observation of weakly bound adsorbed molecular oxygen on powdered titanium dioxide. *J. Phys. Chem. C* **114**, 11924–11930 (2010).

172. Christensen, N. E. The band structure of silver and optical interband transitions. *Phys. Status Solidi B* **54**, 551–563 (1972).

173. Xu, W., Kong, J. S. & Chen, P. Probing the catalytic activity and heterogeneity of Au-nanoparticles at the single-molecule level. *Phys. Chem. Chem. Phys.* **11**, 2767 (2009).

174. Mao, X., Liu, C., Hesari, M., Zou, N. & Chen, P. Super-resolution imaging of non-fluorescent reactions via competition. *Nat. Chem.* **11**, 687–694 (2019).

175. Zou, N. *et al.* Imaging catalytic hotspots on single plasmonic nanostructures via correlated super-resolution and electron microscopy. *ACS Nano* **12**, 5570–5579 (2018).

176. Zou, N. *et al.* Cooperative communication within and between single nanocatalysts. *Nat. Chem.* **10**, 607–614 (2018).

177. Chen, G. *et al.* Bimetallic effect of single nanocatalysts visualized by super-resolution catalysis imaging. *ACS Cent. Sci.* **3**, 1189–1197 (2017).

178. Shen, H., Zhou, X., Zou, N. & Chen, P. Single-molecule kinetics reveals a hidden surface reaction intermediate in single-nanoparticle catalysis. *J. Phys. Chem. C* **118**, 26902–26911 (2014).

179. Zhou, X., Choudhary, E., Andoy, N. M., Zou, N. & Chen, P. Scalable parallel screening of catalyst activity at the single-particle level and subdiffraction resolution. *ACS Catal.* **3**, 1448–1453 (2013).

180. Andoy, N. M. *et al.* Single-molecule catalysis mapping quantifies site-specific activity and uncovers radial activity gradient on single 2D nanocrystals. *J. Am. Chem. Soc.* **135**, 1845–1852 (2013).

181. Han, K. S., Liu, G., Zhou, X., Medina, R. E. & Chen, P. How does a single Pt nanocatalyst behave in two different reactions? A single-molecule study. *Nano Lett.* **12**, 1253–1259 (2012).

182. Zhou, X. *et al.* Quantitative super-resolution imaging uncovers reactivity patterns on single nanocatalysts. *Nat. Nanotechnol.* **7**, 237–241 (2012).

183. Zhou, X., Xu, W., Liu, G., Panda, D. & Chen, P. Size-dependent catalytic activity and dynamics of gold nanoparticles at the single-molecule level. *J. Am. Chem. Soc.* **132**, 138–146 (2010).

184. Chen, P. *et al.* Single-molecule fluorescence imaging of nanocatalytic processes. *Chem. Soc. Rev.* **39**, 4560–4570 (2010).

185. Wang, D., Zhang, D. & Sadtler, B. Irreversibility in anion exchange between cesium lead bromide and iodide nanocrystals imaged by single-particle fluorescence. *J. Phys. Chem. C* **124**, 27158–27168 (2020).

186. Shen, M. *et al.* Competing activation and deactivation mechanisms in photodoped bismuth oxybromide nanoplates probed by single-molecule fluorescence imaging. *J. Phys. Chem. Lett.* **11**, 5219–5227 (2020).

187. Wang, D. *et al.* Role of solid-state miscibility during anion exchange in cesium lead halide nanocrystals probed by single-particle fluorescence. *J. Phys. Chem. Lett.* **11**, 952–959 (2020).

188. Yin, B. *et al.* Fluorescence microscopy of single lead bromide nanocrystals reveals sharp transitions during their transformation to methylammonium lead bromide. *J. Mater. Chem. C* **7**, 3486–3495 (2019).

189. Kumari, G., Kamarudheen, R., Zoethout, E. & Baldi, A. Photocatalytic surface restructuring in individual silver nanoparticles. *ACS Catal.* **11**, 3478–3486 (2021).

190. Canham, S. M. *et al.* Toward the single-molecule investigation of organometallic reaction mechanisms: single-molecule imaging of fluorophore-tagged palladium(ii) complexes. *Organometallics* **27**, 2172–2175 (2008).

191. Esfandiari, N. M. *et al.* Single-molecule imaging of platinum ligand exchange reaction reveals reactivity distribution. *J. Am. Chem. Soc.* **132**, 15167–15169 (2010).

192. Esfandiari, N. M., Wang, Y., McIntire, T. M. & Blum, S. A. Real-time imaging of platinum−sulfur ligand exchange reactions at the single-molecule level via a general chemical technique. *Organometallics* **30**, 2901–2907 (2011).

193. Esfandiari, N. M., Wang, Y., Bass, J. Y. & Blum, S. A. Deconvoluting subensemble chemical reaction kinetics of platinum–sulfur ligand exchange detected with single-molecule fluorescence microscopy. *Inorg. Chem.* **50**, 9201–9203 (2011).

194. Esfandiari, N. M. & Blum, S. A. Homogeneous vs heterogeneous polymerization catalysis revealed by single-particle fluorescence microscopy. *J. Am. Chem. Soc.* **133**, 18145–18147 (2011).

195. Hensle, E. M. & Blum, S. A. Phase separation polymerization of dicyclopentadiene characterized by in operando fluorescence microscopy. *J. Am. Chem. Soc.* **135**, 12324–12328 (2013).

196. Cordes, T. & Blum, S. A. Opportunities and challenges in single-molecule and single-particle fluorescence microscopy for mechanistic studies of chemical reactions. *Nat. Chem.* **5**, 993–999 (2013).

197. Blum, S. A. Location change method for imaging chemical reactivity and catalysis with single-molecule and -particle fluorescence microscopy. *Phys. Chem. Chem. Phys.* **16**, 16333–16339 (2014).

198. Easter, Q. T., Trauschke, V. & Blum, S. A. Catalyst inefficiencies: supported ring-opening metathesis polymerization catalyst yields its ensemble rate from a small number of molecular active sites. *ACS Catal.* **5**, 2290–2295 (2015).

199. Feng, C., Cunningham, D. W., Easter, Q. T. & Blum, S. A. Role of LiCl in generating soluble organozinc reagents. *J. Am. Chem. Soc.* **138**, 11156–11159 (2016).

200. Easter, Q. T. & Blum, S. A. Single turnover at molecular polymerization catalysts reveals spatiotemporally resolved reactions. *Angew. Chem. Int. Ed.* **56**, 13772–13775 (2017).

201. Kitagawa, K. & Blum, S. A. Structure–reactivity studies of intermediates for mechanistic information by subensemble fluorescence microscopy. *ACS Catal.* **7**, 3786–3791 (2017).

202. Feng, C., Easter, Q. T. & Blum, S. A. Structure–reactivity studies, characterization, and transformation of intermediates by lithium chloride in the direct insertion of alkyl and aryl iodides to metallic zinc powder. *Organometallics* **36**, 2389–2396 (2017).

203. Easter, Q. T. & Blum, S. A. Evidence for dynamic chemical kinetics at individual molecular ruthenium catalysts. *Angew. Chem. Int. Ed.* **57**, 1572–1575 (2018).

204. Easter, Q. T. & Blum, S. A. Kinetics of the same reaction monitored over nine orders of magnitude in concentration: when are unique subensemble and single-turnover reactivity displayed? *Angew. Chem. Int. Ed.* **57**, 12027–12032 (2018).

205. Easter, Q. T., Garcia, A. & Blum, S. A. Single-polymer–particle growth kinetics with molecular catalyst speciation and single-turnover imaging. *ACS Catal.* **9**, 3375–3383 (2019).

206. Easter, Q. T. & Blum, S. A. Organic and organometallic chemistry at the single-molecule, -particle, and -molecular-catalyst-turnover level by fluorescence microscopy. *Acc. Chem. Res.* **52**, 2244–2255 (2019).

207. Garcia, A. *et al.* Does selectivity of molecular catalysts change with time? Polymerization imaged by single-molecule spectroscopy. *Angew. Chem. Int. Ed.* **60**, 1550–1555 (2021).

208. Lupo, K. M., Hinton, D. A., Ng, J. D., Padilla, N. A. & Goldsmith, R. H. Probing heterogeneity and bonding at silica surfaces through single-molecule investigation of base-mediated linkage failure. *Langmuir* **32**, 9171–9179 (2016).

209. Ng, J. D. *et al.* Single-molecule investigation of initiation dynamics of an organometallic catalyst. *J. Am. Chem. Soc.* **138**, 3876–3883 (2016).

210. Upadhyay, S. P. *et al.* Fluorescent dendrimeric molecular catalysts demonstrate unusual scaling behavior at the single-molecule level. *J. Phys. Chem. C* **119**, 19703–19714 (2015).

211. Dong, B. *et al.* Single molecule investigation of nanoconfinement hydrophobicity in heterogeneous catalysis. *J. Am. Chem. Soc.* **142**, 13305–13309 (2020).

212. Dong, B. *et al.* In situ quantitative single-molecule study of dynamic catalytic processes in nanoconfinement. *Nat. Catal.* **1**, 135–140 (2018).

213. Chen, T. *et al.* Optical super-resolution imaging of surface reactions. *Chem. Rev.* **117**, 7510–7537 (2017).

214. Ha, J. W. *et al.* Super-resolution mapping of photogenerated electron and hole separation in single metal–semiconductor nanocatalysts. *J. Am. Chem. Soc.* **136**, 1398–1408 (2014).

215. Han, R. *et al.* Geometry-assisted three-dimensional superlocalization imaging of single-molecule catalysis on modular multilayer nanocatalysts. *Angew. Chem. Int. Ed.* **53**, 12865–12869 (2014).

216. Wang, A. *et al.* In situ identification of intermediates of benzyl chloride reduction at a silver electrode by sers coupled with dft calculations. *J. Am. Chem. Soc.* **132**, 9534–9536 (2010).

217. Zhong, J.-H. *et al.* Probing the electronic and catalytic properties of a bimetallic surface with 3 nm resolution. *Nat. Nanotechnol.* **12**, 132–136 (2017).

218. Su, H.-S. *et al.* Probing the local generation and diffusion of active oxygen species on a Pd/Au bimetallic surface by tip-enhanced Raman spectroscopy. *J. Am. Chem. Soc.* **142**, 1341–1347 (2020).

219. Huang, S.-C. *et al.* Probing nanoscale spatial distribution of plasmonically excited hot carriers. *Nat. Commun.* **11**, 4211 (2020).

220. Zong, C. *et al.* Real-time imaging of surface chemical reactions by electrochemical photothermal reflectance microscopy. *Chem. Sci.* **12**, 1930–1936 (2021).

221. Feng, H.-S., Dong, F., Su, H.-S., Sartin, M. M. & Ren, B. In situ investigation of hot-electron-induced Suzuki−Miyaura reaction by surface-enhanced Raman spectroscopy. *J. Appl. Phys.* **128**, 173105 (2020).

222. Trześniewski, B. J. *et al.* In situ observation of active oxygen species in Fe-containing Ni-based oxygen evolution catalysts: the effect of pH on electrochemical activity. *J. Am. Chem. Soc.* **137**, 15112–15121 (2015).

223. Pérez-Gallent, E., Figueiredo, M. C., Calle-Vallejo, F. & Koper, M. T. M. Spectroscopic observation of a hydrogenated CO dimer intermediate during CO reduction on Cu(100) electrodes. *Angew. Chem.* **129**, 3675–3678 (2017).

224. Meirer, F. & Weckhuysen, B. M. Spatial and temporal exploration of heterogeneous catalysts with synchrotron radiation. *Nat. Rev. Mater.* **3**, 324–340 (2018).

225. Weckhuysen, B. M. Snapshots of a working catalyst: possibilities and limitations of in situ spectroscopy in the field of heterogeneous catalysis. *Chem. Commun.* 97–110 (2002) doi:10.1039/B107686H.

226. Hartman, T., Geitenbeek, R. G., Whiting, G. T. & Weckhuysen, B. M. Operando monitoring of temperature and active species at the single catalyst particle level. *Nat. Catal.* **2**, 986–996 (2019).

227. Korhonen, S. T., Beale, A. M., Newton, M. A. & Weckhuysen, B. M. New insights into the active surface species of silver alumina catalysts in the selective catalytic reduction of NO. *J. Phys. Chem. C* **115**, 885–896 (2011).

228. de Smit, E. *et al.* Nanoscale chemical imaging of a working catalyst by scanning transmission X-ray microscopy. *Nature* **456**, 222–225 (2008).

229. Buurmans, I. L. C. *et al.* Catalytic activity in individual cracking catalyst particles imaged throughout different life stages by selective staining. *Nat. Chem.* **3**, 862–867 (2011).

230. Calle-Vallejo, F. *et al.* Finding optimal surface sites on heterogeneous catalysts by counting nearest neighbors. *Science* **350**, 185–189 (2015).

231. Schmid, G. & Corain, B. Nanoparticulated gold: syntheses, structures, electronics, and reactivities. *Eur. J. Inorg. Chem.* **2003**, 3081–3098 (2003).

232. Lopez, N. *et al.* On the origin of the catalytic activity of gold nanoparticles for low-temperature CO oxidation. *J. Catal.* **223**, 232–235 (2004).

233. den Breejen, J. P. *et al.* On the origin of the cobalt particle size effects in Fischer−Tropsch catalysis. *J. Am. Chem. Soc.* **131**, 7197–7203 (2009).

234. Reske, R., Mistry, H., Behafarid, F., Roldan Cuenya, B. & Strasser, P. Particle size effects in the catalytic electroreduction of CO_2 on Cu nanoparticles. *J. Am. Chem. Soc.* **136**, 6978–6986 (2014).

235. Taketoshi, A. & Haruta, M. Size- and structure-specificity in catalysis by gold clusters. *Chem. Lett.* **43**, 380–387 (2014).

236. Somorjai, G. A. & Carrazza, J. Structure sensitivity of catalytic reactions. *Ind. Eng. Chem. Fundam.* **25**, 63–69 (1986).

237. Englisch, M., Jentys, A. & Lercher, J. A. Structure sensitivity of the hydrogenation of crotonaldehyde over Pt/SiO_2 and Pt/TiO_2. *J. Catal.* **166**, 25–35 (1997).

238. Che, M. & Bennett, C. O. The influence of particle size on the catalytic properties of supported metals. in *Advances in Catalysis* (eds. Eley, D. D., Pines, H. & Weisz, P. B.) vol. 36 55–172 (Academic Press, 1989).

239. Bond, G. C. The origins of particle size effects in heterogeneous catalysis. *Surf. Sci.* **156**, 966–981 (1985).

240. Somorjai, G. A. Surface reconstruction and catalysis. *Annu. Rev. Phys. Chem.* **45**, 721–751 (1994).

241. Harris, P. J. F. Sulphur-induced faceting of platinum catalyst particles. *Nature* **323**, 792–794 (1986).

242. Chen, J. J. & Ruckenstein, E. Sintering of palladium on alumina model catalyst in a hydrogen atmosphere. *J. Catal.* **69**, 254–273 (1981).

243. Ruckenstein, E. & Chu, Y. F. Redispersion of platinum crystallites supported on alumina—Role of wetting. *J. Catal.* **59**, 109–122 (1979).

244. Nagai, Y. *et al.* Real-time observation of platinum redispersion on ceria-based oxide by in-situ turbo-XAS in fluorescence mode. *AIP Conf. Proc.* **882**, 594–596 (2007).

245. Newton, M. A., Belver-Coldeira, C., Martínez-Arias, A. & Fernández-García, M. Dynamic in situ observation of rapid size and shape change of supported Pd nanoparticles during CO/NO cycling. *Nat. Mater.* **6**, 528–532 (2007).

246. Newton, M. A., Belver-Coldeira, C., Martínez-Arias, A. & Fernández-García, M. "Oxidationless" promotion of rapid palladium redispersion by oxygen during redox CO/(NO+O_2) cycling. *Angew. Chem. Int. Ed.* **46**, 8629–8631 (2007).

247. Rawool, S. A., Samanta, A., Ajithkumar, T. G., Kar, Y. & Polshettiwar, V. Photocatalytic hydrogen generation and CO_2 conversion using g-C_3N_4 decorated dendritic fibrous nanosilica: role of interfaces between silica and g-C_3N_4. *ACS Appl. Energy Mater.* **3**, 8150–8158 (2020).

248. DuChene, J. S. *et al.* Optical excitation of a nanoparticle Cu/p-NiO photocathode improves reaction selectivity for CO_2 reduction in aqueous electrolytes. *Nano Lett.* **20**, 2348–2358 (2020).

249. DuChene, J. S., Tagliabue, G., Welch, A. J., Cheng, W.-H. & Atwater, H. A. Hot hole collection and photoelectrochemical CO_2 reduction with plasmonic Au/p-GaN photocathodes. *Nano Lett.* **18**, 2545–2550 (2018).

250. Mishra, A. K., Belgamwar, R., Jana, R., Datta, A. & Polshettiwar, V. Defects in nanosilica catalytically convert CO_2 to methane without any metal and ligand. *Proc. Natl. Acad. Sci.* **117**, 6383–6390 (2020).

251. Dhiman, M. *et al.* Plasmonic colloidosomes of black gold for solar energy harvesting and hotspots directed catalysis for CO_2 to fuel conversion. *Chem. Sci.* **10**, 6594–6603 (2019).

252. Devasia, D., Wilson, A. J., Heo, J., Mohan, V. & Jain, P. K. A rich catalog of C–C bonded species formed in CO_2 reduction on a plasmonic photocatalyst. *Nat. Commun.* **12**, 2612 (2021).

253. P. Kuhl, K., R. Cave, E., N. Abram, D. & F. Jaramillo, T. New insights into the electrochemical reduction of carbon dioxide on metallic copper surfaces. *Energy Environ. Sci.* **5**, 7050–7059 (2012).

254. Calvinho, K. U. D. *et al.* Selective CO_2 reduction to C_3 and C_4 oxyhydrocarbons on nickel phosphides at overpotentials as low as 10 mV. *Energy Environ. Sci.* **11**, 2550–2559 (2018).

255. Kim, D., Kley, C. S., Li, Y. & Yang, P. Copper nanoparticle ensembles for selective electroreduction of CO_2 to $C_2 – C_3$ products. *Proc. Natl. Acad. Sci.* **114**, 10560–10565 (2017).

256. Ma, M., Djanashvili, K. & Smith, W. A. Controllable hydrocarbon formation from the electrochemical reduction of CO_2 over Cu nanowire arrays. *Angew. Chem. Int. Ed.* **55**, 6680–6684 (2016).

257. Du, C. *et al.* CO_2 transformation to multicarbon products by photocatalysis and electrocatalysis. *Mater. Today Adv.* **6**, 100071 (2020).

258. Huang, J. E. *et al.* CO_2 electrolysis to multicarbon products in strong acid. *Science* **372**, 1074–1078 (2021).

259. Chang, L. *et al.* Electronic structure of the plasmons in metal nanocrystals: fundamental limitations for the energy efficiency of hot electron generation. *ACS Energy Lett.* **4**, 2552–2568 (2019).

260. Govorov, A. O., Zhang, H. & Gun'ko, Y. K. Theory of photoinjection of hot plasmonic carriers from metal nanostructures into semiconductors and surface molecules. *J. Phys. Chem. C* **117**, 16616–16631 (2013).

261. Sundararaman, R., Narang, P., Jermyn, A. S., Goddard Iii, W. A. & Atwater, H. A. Theoretical predictions for hot-carrier generation from surface plasmon decay. *Nat. Commun.* **5**, 5788 (2014).

262. Brown, A. M., Sundararaman, R., Narang, P., Goddard, W. A. & Atwater, H. A. Nonradiative plasmon decay and hot carrier dynamics: effects of phonons, surfaces, and geometry. *ACS Nano* **10**, 957–966 (2016).

263. Narang, P., Sundararaman, R. & Atwater, H. A. Plasmonic hot carrier dynamics in solid-state and chemical systems for energy conversion. *Nanophotonics* **5**, 96–111 (2016).

264. Byers, C. P. *et al.* Single-particle spectroscopy reveals heterogeneity in electrochemical tuning of the localized surface plasmon. *J. Phys. Chem. B* **118**, 14047–14055 (2014).

265. Sundaresan, V., Monaghan, J. W. & Willets, K. A. Visualizing the effect of partial oxide formation on single silver nanoparticle electrodissolution. *J. Phys. Chem. C* **122**, 3138–3145 (2018).

266. Kirchner, S. R. *et al.* Snapshot hyperspectral imaging (SHI) for revealing irreversible and heterogeneous plasmonic processes. *J. Phys. Chem. C* **122**, 6865–6875 (2018).

267. Willets, K. A. Supercharging superlocalization microscopy: how electrochemical charging of plasmonic nanostructures uncovers hidden heterogeneity. *ACS Nano* **13**, 6145–6150 (2019).

268. Walters, P. *An introduction to ergodic theory*. (Springer Science & Business Media, 2000).

269. Birkhoff, G. D. Proof of the ergodic theorem. *Proc. Natl. Acad. Sci. U. S. A.* **17**, 656–660 (1931).

270. von Neumann, J. Physical applications of the ergodic hypothesis. *Proc. Natl. Acad. Sci.* **18**, 263–266 (1932).

271. Moore, C. C. Ergodic theorem, ergodic theory, and statistical mechanics. *Proc. Natl. Acad. Sci.* **112**, 1907–1911 (2015).

272. Mohan, Varun, Ripani, Roma, & Jain, Prashant. K. Room-temperature, catalyst-free methane chlorination. (2021).

273. Cherney, D. P., Duirk, S. E., Tarr, J. C. & Collette, T. W. Monitoring the speciation of aqueous free chlorine from ph 1 to 12 with Raman spectroscopy to determine the identity of the potent low-ph oxidant. *Appl. Spectrosc.* **60**, 764–772 (2006).